MECHANICS OF SURFACE INSTABILITIES OF SOFT NANOFIBERS AND NONLINEAR

CONTACTS OF HYDROGELS

A Dissertation
Submitted to the Graduate Faculty
of the
North Dakota State University
of Agriculture and Applied Science

By

Mojtaba Ahmadi

In Partial Fulfillment of the Requirements
for the Degree of
DOCTOR OF PHILOSOPHY

Major Department:
Mechanical Engineering

July 2020

Fargo, North Dakota

North Dakota State University
Graduate School

Title

MECHANICS OF SURFACE INSTABILITIES OF SOFT NANOFIBERS
AND NONLINEAR CONTACTS OF HYDROGELS

By

Mojtaba Ahmadi

The Supervisory Committee certifies that this ***disquisition*** complies with North Dakota

State University's regulations and meets the accepted standards for the degree of

DOCTOR OF PHILOSOPHY

SUPERVISORY COMMITTEE:

Dr. Xiangfa Wu

Chair

Dr. Mariusz Ziejewski

Dr. Chad Ulven

Dr. Long Jiang

Dr. Andrew B. Croll

Approved:

08/12/2020   Dr. Alan R. Kallmeyer

Date   Department Chair

ABSTRACT

The research of this dissertation is formulated in two fields, i.e., the theoretical and computational studies of circumferential wrinkling on soft nanofibers and the swelling mechanics study of a bi-layered spherical hydrogel containing a hard core.

Continuous polymer nanofibers have been massively produced by means of the low-cost, top-down electrospinning technique. As a unique surface instability phenomenon, surface wrinkling in circumferential direction is commonly observed on soft nanofibers in electrospinning. In this study, a theoretical continuum mechanics model is developed to explore the mechanisms of circumferential wrinkling on soft nanofibers under uniaxial stretching. The model is able to examine the effects of elastic properties, surface energy, and fiber radius on the critical axial stretch to trigger circumferential wrinkling and to discover the threshold fiber radius to initiate spontaneous wrinkling. In addition, nonlinear finite element method (FEM) is further adopted to predict the critical mismatch strain to evoke circumferential wrinkling in core-shell polymer nanofibers containing a hard core, as a powerful computational tool to simulate controllable wrinkling on soft nanofibers via co-electrospinning polymer nanofibers incorporated with nanoparticles as the core. The studies provide rational understanding of surface wrinkling in polymer nanofibers and technical approaches to actively tune surface morphologies of polymer nanofibers for particular applications, e.g. high-grade filtration, oil-water separation, polymer nanocomposites, wound dressing, tissue scaffolding, drug delivery, and renewable energy harvesting, conversion, and storage, etc.

Furthermore, hydrogels are made of cross-linked polymer chains that can swell significantly when imbibing water and exhibit inhomogeneous deformation, stress, and, water concentration fields when the swelling is constrained. In this study, a continuum mechanics field

theory is adopted to study the swelling behavior of a bi-layered spherical hydrogel containing a hard core. The problem is reduced into a two-point boundary value problem of a 2nd-order nonlinear ordinary differential equation (ODE) and solved numerically. Effects of material properties on the deformation, stress, and water concentration fields of the hydrogel are examined. The study offers a rational route to design and regulate hydrogels with tailorable swelling behavior for practical applications in drug delivery, leakage blocking, etc.

ACKNOWLEDGMENTS

DEDICATION

This thesis work is dedicated to my parents, who have been a constant source of support and encouragement during the challenges of graduate school and life, who have always loved me unconditionally and whose good examples have taught me to work hard for the things that I aspire to achieve. I am truly grateful for having them in my life. This work is also dedicated to my lovely wife, Maryam, who recently joined me in my life journey as my partner and supported me during this short period of time with her true love and encouragement.

TABLE OF CONTENTS

LIST OF FIGURES

LIST OF APPENDIX FIGURES

CHAPTER 1. INTRODUCTION

1.1. Motivation

Polymeric materials have found their way in a wide range of structural and multifunctional applications such as structural plastics, fiber-reinforced polymer matrix composites (PMCs), biomedical implants and devices, sensors, etc. as they can be produced in various materials and structures with high specific strength and stiffness, sound manufacturability, excellent corrosion resistance, and highly tailorable mechanical and multifunctional properties. Among those, polymer nanofibers and polymeric hydrogels have been under intensive investigations in recent years due to their unique properties and promising applications in broad sectors for better and healthier life, cleaner water, air and environment, and more efficient energy utilization. The study of their unique mechanical performance forms the main research topics of this dissertation work.

1.1.1. Continuous Polymer Nanofibers

Continuous polymer nanofibers have been broadly produced by means of the electrospinning technique in a low-cost and well scalable way (Reneker & Chun, 1996; Dzenis, 2004; Li & Xia, 2004a). Electrospinning is a top-down nanomanufacturing technique based on the principle of electrohydrodynamic jetting of polymer solutions or melts, which has been used extensively to fabricate various types of continuous nanofibers (e.g., monolithic, composite, core-shell, multi-layered, porous, surface-decorated, etc.) of synthetic and natural polymers or polymer-derived carbon, silicon, metals, metal oxides, ceramics, etc. (Reneker et al., 2007; Reneker & Yarin, 2008). Electrospun nanofibers are a unique type of one-dimensional (1D) submicron materials, which are normally collected as nonwoven nanofiber mats in the

electrospinning process. These nanofibrous materials carry superior structural properties such as a high surface area to volume ratio (over 100 m^2/g), improved tensile strength, and tailorable surface morphology and microstructures (Gibson et al., 2001). To date, electrospun nanofibers have been finding a variety of promising applications in nanocomposites (Kim & Reneker, 1999; Huang et al., 2003; Dzenis, 2008; Lai et al., 2008; Wu, 2009; Chen et al., 2011; Sinha-Ray et al., 2012; Wu et al., 2013; Wu & Yarin, 2013; Mohammadzadehmoghadam et al., 2015), fine gas/liquid filtration (Gopal et al., 2006; Maze et al., 2007; Barhate & Ramakrishna, 2007; Zhou & Wu, 2015; Zhou et al., 2016), wound dressing (Gibson et al., 2001; Smith, Kataphinan, et al., 2004; Smith, Reneker, et al., 2004), drug delivery (Kenawy et al., 2002; Chew et al., 2006; Liang et al., 2007; Barnes et al., 2007; Xie et al., 2008), tissue engineering (Li et al., 2002; Matthews et al., 2002; Burger et al., 2006; Pham et al., 2006), and energy harvesting, conversion and storage (Kim et al., 2007; Ji & Zhang, 2009; Schulz et al., 2010; Dong et al., 2011; Zhang et al., 2011; Joshi et al., 2012; Zhou et al., 2012; Zhou & Wu, 2013; Zhou & Wu, 2014; Zhou et al., 2014), among others. This has triggered rapidly expanding research on the electrospinning process and electrospinability of various polymer solutions (Kirichenko et al., 1986; Saville, 1997; Spivak & Dzenis, 1998; Spivak et al., 2000; Feng, 2002, 2003; Reneker et al., 2007; Wu et al., 2020), mechanical characterization of nanofibers and nanofiber membranes (e.g., modulus, tensile strength, plasticity, etc.) (Cuenot et al., 2000; Tan & Lim, 2004, 2006; Tan, Goh, et al., 2005; Tan, Ng, & Lim, 2005; Inai et al., 2005; Ji et al., 2006; Zussman et al., 2006; Yuya et al., 2007; Arinstein et al., 2007; Naraghi et al., 2007a, 2007b), and modeling of the mechanical behaviors of nanofibers and fiber networks (Wu & Dzenis, 2005, 2006, 2007a, 2007b, 2007c; Wu et al., 2008; Wu, 2010; Wu et al., 2010; Wu et al., 2012), etc.

1.1.2. Polymeric Hydrogels

Hydrogels are flexible long-chained polymers that are cross-linked into a three-dimensional network, which can imbibe a large quantity of water from the environment and swell without dissolving (Flory, 1953; Tanaka, 1981; Shibayama & Tanaka, 1993; Kopeček, 2002; Zhao et al., 2008a; Hong et al., 2008b; Hong et al., 2009; Ahmed, 2015). Due to their hydrophilicity, softness, smartness, and ability to store a large amount of water, hydrogels have been extensively used in diverse technologies, including tissue engineering (Lee & Mooney, 2001; Nowak et al., 2002; Drury & Mooney, 2003; Luo & Shoichet, 2004; Wong et al., 2008), drug delivery (Fischel-Ghodsian et al., 1988; Jeong et al., 1997; Langer, 1998; Qiu & Park, 2001; Duncan, 2003; Peppas et al., 2006), medical devices (Wichterle & Lim, 1960; Jagur-Grodzinski, 2006; Peppas et al., 2006; Discher et al., 2009), and stimuli-sensitive actuators (Beebe et al., 2000; Dong et al., 2006; Sidorenko et al., 2007; Li et al., 2007; Cho et al., 2008). These applications have resulted in the intensive investigations on various types of hydrogels with broad tailorable functionalities and modeling of their mechanical behaviors (Raschip et al., 2007; Hong et al., 2008b; Hennink & van Nostrum, 2012; Popadyuk et al., 2014; Zholobko et al., 2014a; Zholobko et al., 2014b; Ahmed, 2015; Walker et al., 2019).

1.2. Problem Statements

1.2.1 Circumferential Wrinkling of Polymer Nanofibers

Circumferential wrinkling has been commonly observed on soft electrospun polymer nanofibers. Two different scenarios could be responsible for such circumferential wrinkling. First, even by excluding the solvent evaporation from a drying polymer solution jet during an electrospinning process, the combined effect of surface energy and nonlinear elasticity of the soft

nanofibers can trigger the circumferential wrinkling. The second scenario is relevant to the core-shell nanostructure as the electrospun jet starts drying inhomogeneously to form a glassy shell surrounding a soft core, which would create a mismatched strain between the core and shell layers, and as a result, cause the circumferential wrinkling.

Regarding the first scenario, no theoretical model is available yet in the literature for exploring the rational mechanisms of circumferential winkling on electrospun nanofibers including the effect of surface energy and the threshold fiber diameter to trigger spontaneous circumferential wrinkling, a special surface instability phenomenon induced purely by surface energy without mechanical loadings. For the second scenario, Wang et al. (2009) conducted the nonlinear finite element analysis (FEA) to extract the surface wrinkle mode chart in terms of the surface morphology (i.e., the wavenumber n) against the stiffness and aspect ratios (E_f/E_s and a/t) of the electrospun fibers. However, the corresponding critical mismatch strain was not predicted explicitly in their study. Further justification still needs to be researched in this dissertation on how to apply these theoretical predictions for the design and optimization of the surface winkle modes of electrospun fibers for practical applications. Specifically, based on nonlinear FEA, the present study proposes an innovative technique to actively alter and optimize the circumferential wrinkling via co-electrospinning polymer solution containing nanoparticles as the core.

1.2.2. Inhomogeneous Swelling of Hydrogels

Since mechanical loads or geometric constraints are ubiquitous in hydrogels in any practical applications, the swelling hydrogel would reach to an inhomogeneous and anisotropic equilibrium state after imbibing sufficient water from environment (Kim et al., 2006; Zhao et al.,

2008a; Hong et al., 2009). Yet, only a few theoretical analyses have been made for determining the deformation, stress, and water concentration fields of monolithic hydrogels in inhomogeneous and anisotropic equilibrium states (Zhao et al., 2008a).

In the view of applications, understanding of the responses (e.g., displacements, stresses, and water concentration) of hydrogels to external stimuli of either mechanical, chemical, electrical, electromagnetic loads or their combinations is crucial to design hydrogel-based functional materials and reliable soft devices/machines and predict relevant multifunctional performances (Peppas et al., 2000). Since the last decade, the promising biomedical applications of soft materials have triggered intensive research of swelling mechanics of hydrogels. It is important to mention that swelling can induce various forms of instability like cavitation, debonding, surface wrinkling and creasing, etc. (Southern & Thomas, 1965; Sidorenko et al., 2007; Hong et al., 2008a; Trujillo et al., 2008; Zhang et al. 2008; Hong et al., 2009). Yet, no research has been made on exploring the swelling mechanics of a bi-hydrogel that is made of two hydrogels with different gel stiffness and water absorption. In practice, bi-hydrogel structures are expected to provide extensive opportunities to design and optimize the swelling performance of hydrogels, which forms the second research topic of this dissertation.

1.3. Research Objectives

This dissertation work is formulated on the basis of continuum mechanics. The outstanding problems addressed above are studied theoretically by formulating novel analytical and finite element models with the assumption that the polymers and hydrogels are treated as hyperelastic solids under proper constraints and external loads.

5

For the first problem to explore the critical conditions to trigger circumferential wrinkling on soft polymer nanofibers under uniaxial stretching, an analytical continuum mechanics model is developed with the assumption that the axisymmetric circumferential wrinkling is triggered by superimposing a periodic linear displacement disturbance onto a deformed configuration of the soft fiber. The unique surface energy is taken into account in this model, which shows the obvious size effect in the critical axial stretch to evoke the surface wrinkling. Effects of nonlinear elasticity, surface energy, and axial stretch of the soft nanofibers on circumferential wrinkling behaviors are examined in detail. The present modeling work results in a novel governing equation that is capable of explaining the effects of fiber material and geometric parameters to trigger the unique spontaneous circumferential wrinkling on soft polymer nanofibers, which is first discovered in this dissertation research.

On the second problem that is treated as an extension of the above one, as a viable experimental approach, hard cores [e.g., carbon nanotubes (CNTs), silica particles, etc.] are proposed to incorporate into the polymer nanofibers via coaxial electrospinning, which can rationally alter the surface wrinkle modes of the resulting core-shell nanofibers. The core-shell structured nanofiber is an approach to the inhomogeneity of the mechanical properties in the fiber cross-section. A finite element model is developed to explore the dependencies of surface wrinkle modes of the electrospun core-shell polymer fibers upon the thickness and stiffness of the glassy shell and inner soft sol-gel layers.

For the third problem, the displacement, stress, and water concentration fields of a bi-layered spherical hydrogel bonded onto a hard core are considered by formulating and solving the relevant swelling mechanics problem, which is an extension of the problem considered by Zhao et al. (2008). Experimentally, it is convenient to coat a 2nd gel layer onto the 1st one to form

a bi-layered hydrogel or a composite hydrogel layer. To do so, the 2nd layer can be used to regulate the swelling behavior of the entire hydrogel system. In practice, it is favorable to apply a relatively stiff surface gel layer to protect the inner hydrogel layer such that generation of compressive radial stress to stabilize the core-shell structure and suppression of the wear and tear of the inner softer hydrogel layer. The present problem is reduced into a two-point boundary value problem of a 2nd-order ordinary differential equation (ODE) with the inner continuity conditions between the two neighboring layers and solved numerically. Effects of the outer layer stiffness on the displacement, stress, and water concentration fields are examined and compared in a numerical manner.

The present dissertation consists of six chapters, and the supplementary detailed formula derivations and data are provided in the Appendix. The six chapters are planned as below.

Chapter 1: Introduction, motivation, and research background of the current dissertation are provided in this chapter. The research objectives with corresponding hypotheses are further explained in this chapter.

Chapter 2: Research background of electrospun polymer nanofibers and polymeric hydrogels are provided along with some of the existing analytical and finite element models on surface wrinkling in electrospun nanofibers and inhomogeneous and anisotropic equilibrium state in swollen hydrogels. These models are explained to show the backgrounds of the objectives of the present dissertation.

Chapter 3: In this chapter, the first objective is fulfilled, which includes the development of an analytical continuum mechanics model to explore the wrinkling phenomena and the effects of varying fiber material and geometrical parameters on the wrinkling behaviors of the soft electrospun polymer nanofibers. This model is further examined numerically to demonstrate the

correlation of critical axial stretch to the corresponding circumferential wrinkle mode. Besides, the threshold fiber radius to trigger the spontaneous circumferential wrinkling is first discovered in the limiting case of zero axial stretch. A research paper based on the results of this theoretical study has been published in the Physical Review E (2020).

Chapter 4: In this chapter, based on the 2nd objective of this dissertation, a finite element model is developed to numerically analyze the surface wrinkle modes of electrospun core-shell polymer nanofibers in response to the thickness and stiffness of the glassy shell and inner soft sol-gel layers. The study provides a rational basis of surface wrinkling in electrospun polymer fibers and the viable technical strategies to regulate the electrospinning process for producing ultrathin polymer fibers with tunable surface morphologies for broad applications (e.g., oil-water separation, tissue scaffolding, etc.). A research paper based on the results of this theoretical study has been published in the Journal of Physics Communications (2019).

Chapter 5: In this chapter, an analytical model is developed to study the swelling behavior of a bi-layered spherical hydrogel containing a hard core after imbibing sufficient water from the environment, which covers the 3rd objective. The problem is reduced into a two-point boundary value problem of a 2nd-order nonlinear ODE and solved numerically. Effects of material properties on the deformation, stress, and water concentration fields of the hydrogel are examined. The study offers a rational route to design and regulate hydrogels with tailorable swelling behaviors for practical applications such as drug delivery, leakage blocking, etc. A research paper based on the results of this theoretical study has been published in the Journal of Applied Physics (2020).

Chapter 6: This is the final chapter to summarize the significant achievements gained in this dissertation research. In addition, suggestions and recommendations for future investigations in the related researched topics are made.

CHAPTER 2. RESEARCH BACKGROUND

2.1. Circumferential Wrinkling in Electrospun Polymer Nanofibers

2.1.1. Electrospun Polymer Nanofibers and Applications

Electrospinning provides a viable technique for producing low-cost, ultrathin continuous fibers of polymers and polymer-derived carbon, silicon, metals, metal oxides, ceramics, etc. with the diameters ranging from a few nanometers to micrometers (Reneker & Chun, 1996; Dzenis, 2004; Li & Xia, 2004a; Reneker et al., 2007; Reneker & Yarin, 2008). The unique continuity, large specific surface area (~1-100 m^2/g) (Wang et al., 2009), improved tensile strength, and tunable surface morphologies and microstructures are the superior structural advantages of electrospun fibers that are resulted mainly from their size effects in mechanical, physical, and chemical properties (Gibson et al., 2001). As a result, these unique one-dimensional (1D) electrospun continuous nanofibers of natural and synthetic polymers and polymer-derived carbon, silicon, metals, metal oxides, ceramics, etc. have been considered as a new class of nanostructured materials for broad structural and multifunctional applications under intensive investigations. So far, electrospun nanofibrous materials have been considered as the key constituents in protective clothing and wound dressing (Gibson et al., 2001; Smith et al., 2004a; Smith et al., 2004b), high-grade gas and liquid filtration (Gopal et al., 2006; Maze et al., 2007; Barhate & Ramakrishna, 2007; Zhou & Wu, 2015; Zhou et al., 2016), nanofiber-reinforced polymer matrix composites (PMCs) (Kim & Reneker, 1999; Huang et al., 2003; Dzenis, 2008; Lai et al., 2008; Wu, 2009; Chen et al., 2011; Sinha-Ray et al., 2012; Wu et al., 2013; Wu & Yarin, 2013; Mohammadzadehmoghadam et al., 2015), biodegradable scaffolds for cell growth (Li et al., 2002; Matthews et al., 2002; Burger et al., 2006; Pham et al., 2006), drug delivery (Kenawy et al., 2002; Chew et al., 2006; Liang et al., 2007; Barnes et al., 2007; Xie et al., 2008),

and energy harvesting, conversion and storage (Kim et al., 2007; Ji & Zhang, 2009; Schulz et al., 2010; Dong et al., 2011; Zhang et al., 2011; Joshi et al., 2012; Zhou et al., 2012; Zhou & Wu, 2013; Zhou & Wu, 2014; Zhou et al., 2014), among others. This has triggered rapidly expanding research on the electrospinning process and electrospinability of various polymer solutions (Kirichenko et al., 1986; Saville, 1997; Spivak & Dzenis, 1998; Spivak et al., 2000; Feng, 2002, 2003; Reneker et al., 2007; Wu et al., 2020), mechanical characterization of nanofibers and nanofiber membranes (e.g., elastic modulus, tensile strength, plasticity, etc.) (Cuenot et al., 2000; Tan & Lim, 2004, 2006; Tan et al., 2005a; Tan et al., 2005b; Inai et al., 2005; Ji et al., 2006; Zussman et al., 2006; Yuya et al., 2007; Arinstein et al., 2007; Naraghi et al., 2007a, 2007b), and modeling of the mechanical behaviors of nanofibers and fiber networks (Wu & Dzenis, 2005, 2006, 2007a, 2007b, 2007c; Wu et al., 2008; Wu, 2010; Wu et al., 2010; Wu et al., 2012), etc.

2.1.2. Electrospinning Process and Surface Wrinkling in Electrospun Nanofibers

In a typical electrospinning process as illustrated in Figure 2-1, a polymer solution is fed into a capillary tube to form a droplet at the capillary tip. Under the action of a high-voltage direct current (DC) electrostatic field, the droplet deforms into a Taylor cone (Figure 2-2) (Taylor, 1969; Yarin et al., 2001b; Reneker et al. 2007; Reneker & Yarin, 2008). Once the electrostatic force overcomes the surface tension of the Taylor cone, the droplet is ejaculated and elongated into an electrospinning jet. After a variety of jet instabilities (Reneker et al., 2000; Yarin et al., 2001a, 2001b; Shin et al., 2001; Hohman et al., 2001; Reneker et al. 2007; Reneker & Yarin, 2008), solvent evaporation (Koombhongse et al., 2001; Wu et al., 2011), and polymer solidification, the drying jet is finally collected as a nonwoven nanofiber mat on the collector. The entire process of electrospinning is a multi-physics process involving electrohydrodynamics,

11

heat and mass transfer, phase separation, polymer solidification, etc. The fast solvent evaporation from the tiny jet may unavoidably induce the radial gradient in the material properties, microstructures (e.g., polymer chain orientation), and residual stresses and strains in the resulting fiber cross-section, though, experimental pieces of evidence are still lacking at this time. In the electrospinning process, the production of continuous nanofibers with controllable surface morphology is a desirable technological strategy to realize many promising applications of nanofibers such as high-grade gas and liquid filtration and tissue scaffolding. Typically, a dilute polymer solution made from a soft polymer dissolved in a highly volatile organic solvent will lead to the fast drying due to rapid solvent evaporation out of the thin electrospun jet, which may result in two competing fiber surface morphologies, i.e., the porous fiber surface due to thermodynamic phase separation of the binary polymer-solvent system (Bognitzki et al., 2001; Dayal et al., 2007) as well as the circumferentially wrinkled fiber surface due to nonuniform residual strains across the fiber section and mechanical destabilization of the glassy surface layer after radially uneven drying induced strain mismatch (see Figure 2-3) (Koombhongse et al., 2001; Pai et al., 2009). The latter are different from their counterparts of longitudinal surface winkles that were observed in electrospun thermoplastic nanofibers under uniaxial tension (Figure 2-4) (Naraghi et al., 2007a, 2007b) and quantitatively interpolated by continuum mechanics models and molecular dynamics simulations (Wu et al., 2008; Wu, 2010; Tang et al., 2015). To date, substantial experimental and modeling approaches have been made to control and understand the surface wrinkling in electrospun nanofibers.

12
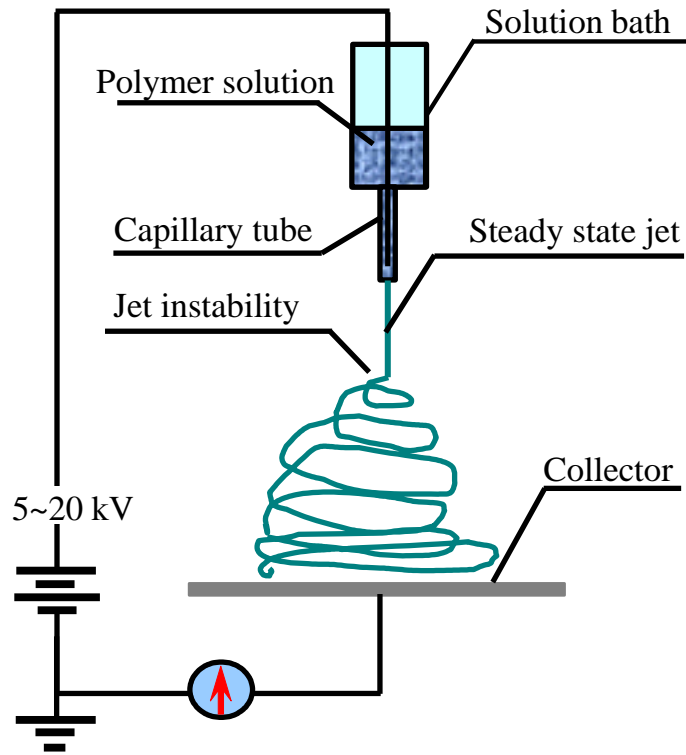
Figure 2-1. Schematic electrospinning process (Courtecy of Dr. Wu's group at NDSU).
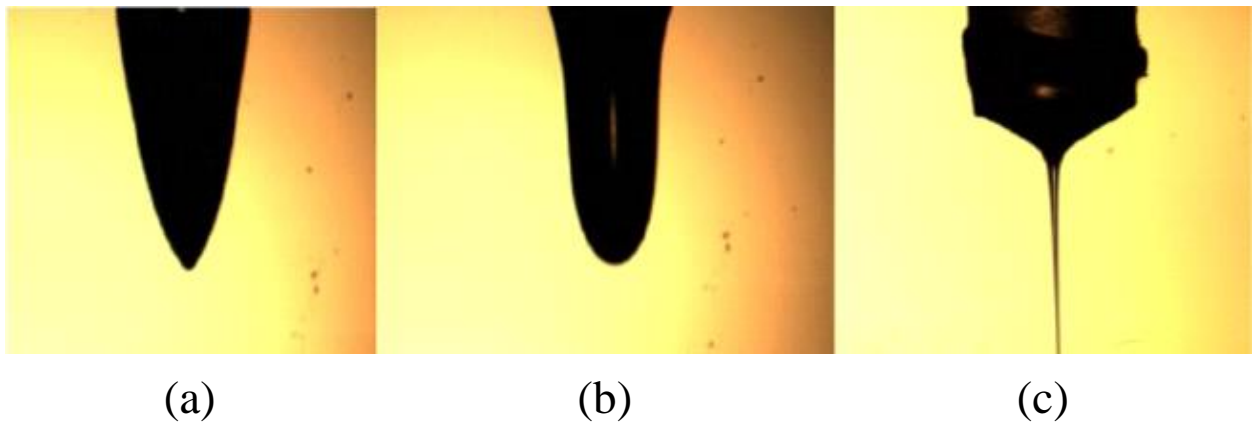
Figure 2-2. Formation of continuous nanofibers: (a) Taylor cone (a deformed droplet in a biased DC electrostatic field), (b) an electrostatically stretched droplet, (c) a thin jet ejaculated in a stable electrospinning process (Courtecy of Dr. Wu's group at NDSU).
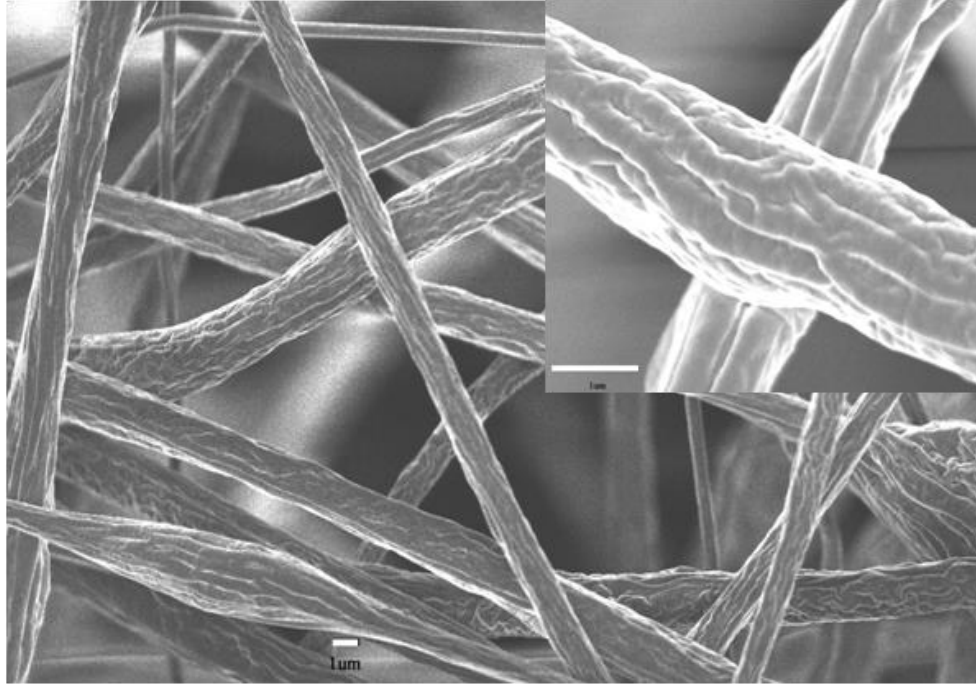
Figure 2-3. SEM micrographs of circumferential wrinkles on electrospun PS fibers prepared from 10 wt. % PS/THF solution (Courtecy of Dr. Wu's group at NDSU).
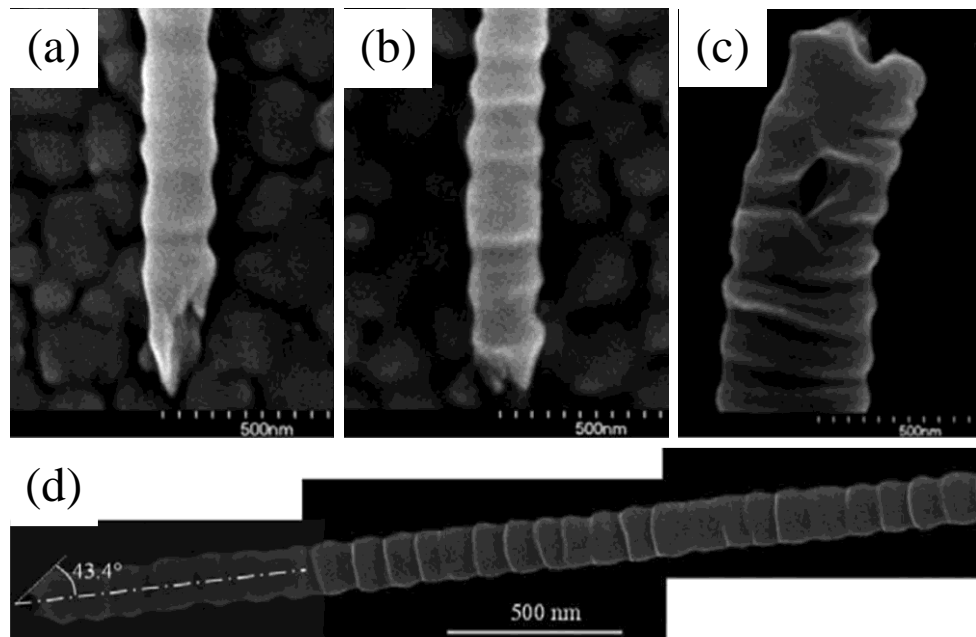
Figure 2-4. Longitudianl wrinkling (rippling) (a), (b) Scanning electron microscope (SEM) images of surface morphology of as-electrospun PAN nanofibers after tensile breakage. The fiber breakage was induced by extrusion of a 45° conic region. (c) SEM image of the fiber breakage due to the formation of voids. (d) SEM image of ripples formed on PAN nanofiber surfaces subjected to axial stretching (Naraghi et al., 2007a, 2007b, Wu et al., 2008).

Model-based simulation of solvent evaporation from a polymer jet in electrospinning has confirmed the drastically uneven radial distribution of solvent in the jet with the diameter of a few micrometers (Wu et al., 2011). Thus, the surface layer of an electrospun jet starts drying (solidification) instantaneously after the jet leaves the nozzle while the core of the jet is nearly intact up to seconds in the case of a typical electrospinning process. Such theoretical prediction provides the rational basis of ribbon-like structures observed in electrospun fibers by Koombhongse et al. (2001). They further proposed a kinematic mechanism responsible for the formation of shaped fibers in electrospinning such that the atmospheric pressure serves as the driving force to collapse the fast-drying glassy skin (shell) initially solidified on the jet surface. Such a mechanism is applicable to interpolate the wrinkled surface morphologies in electrospun fibers (Pai et al., 2009). Therefore, in principle, the surface wrinkling of electrospun fibers can be tuned via adjusting the process and material parameters of electrospinning such as the initial jet diameter (i.e., the nozzle outlet diameter), the solvent concentration, etc. For instance, the surface wettability (against water) of electrospun polystyrene (PS) nanofiber membranes can be tuned via controlling the diameter and drying-induced surface wrinkle modes of the ultrathin PS fibers, which was made possible through adjusting the tetrahydrofuran (THF) concentration of the PS/THF solution used in electrospinning. The PS nanofiber membranes have demonstrated promising applications for effective water filtration and oil-water separation (Yu, 2013; Zhou & Wu, 2015; Zhou et al., 2016).

Theoretically, Wu et al. (2008) and Wu (2010) first formulated a nonlinear elasticity model to explore the physical mechanisms governing the longitudinal wrinkling in soft nanofibers under axial stretching that was first discovered in single-nanofiber tension tests (Naraghi et al., 2007a, 2007b). The main contribution of these works is that surface energy as a

unique physical parameter for nanostructured materials was first introduced in wrinkling analysis of soft nanofibers and discovery of spontaneous wrinkling of soft nanofibers when the fiber radius is below a certain value. Such a threshold fiber radius is a function with respect to the surface energy and elastic properties of the nanofibers and is independent of the electrospinning process and process parameters. Due to the unique spontaneous wrinkling at small fiber radii, electrospinning is unable to fabricate continuous nanofibers below a certain fiber radius due to jet beading instability. In parallel, Mora et al. (2010) and Taffetani and Ciarletta (2015a) conducted the experimental study to show the Rayleigh-Plateau instability in slender gel cylinders and formulated the first-principle models to address their observations by means of linear perturbations within the framework of small deformations. The critical condition (Mora et al., 2010) to trigger such a longitudinal surface instability (beading) was determined as $\gamma = 6\mu R_0$, where γ, μ, and R_0 are the surface tension, shear modulus, and initial radius of the gel cylinder, respectively. This critical condition is similar to one to evoke the spontaneous longitudinal rippling in soft nanofibers under axial stretching (Wu et al., 2008; Wu, 2010) though the latter was based on a hyperelastic solid model for rubbery polymeric materials. Furthermore, Taffetani and Ciarletta (2015b) and Ciarletta et al. (2016) formulated a systematic nonlinear elastic framework to investigate the effect of capillary energy on the beading instability in soft cylindrical gels, a phenomenon similar to the longitudinal rippling in soft nanofibers under axial stretching (Wu et al., 2008). Sophisticated linear and nonlinear instability analyses were conducted in these studies while the effect of axial stretching as a common physical condition in practice was excluded in these studies and thus it is difficult to apply these theoretical results to guide the practical applications in materials science and other engineering fields such as nanofiber fabrication, single-fiber tensile test, etc.

16

In the above, longitudinal wrinkling on soft nanofibers has been explored at different extent of accuracy in the last decade. Yet, the continuum mechanics modeling of circumferential wrinkling on soft nanofibers has not been reported in the literature though such wrinkling phenomenon has been commonly observed in experiments.

In addition, within the framework of continuum mechanics, initiation of surface wrinkling in electrospun fibers can be modeled simply as classic circumferential buckling of elastic cylindrical shells containing an elastic core under external pressure (Wang et al., 2009), in which the effect of surface energy is ignored. The critical buckling pressure p_c can be expressed as (Herrmann & Forrestal, 1965)

$$p_c = \eta \left[\frac{n^2 - 1}{3} + \frac{4(1 - v_f^2)(E_s/E_f)(a/t)^3}{(1 + v_s)[2n(1 - v_s) - (1 - 2v_s)]} \right] p_0.$$

(2.1)

In Eq. (2.1), $\eta = 1 + (1 - v_f^2)/[(1 + v_s)(1 - 2v_s)](E_s/E_f)(a/t)$, $p_0 = E_f / [4(1 - v_f^2)](t/a)^3$, n is the wavenumber of the circumferential surface wrinkles, E_f and E_s are respectively the moduli of the surface layer (film) and core (substrate), v_f and v_s are respectively the Poisson's ratios of the film and substrate, t is the film thickness, and a is the radius of the substrate. With the assumption of incompressibility (i.e., $v_f = v_s = 0.5$), Wang et al. (2009) derived an expression of the critical wave number n_{crit} in minimizing the critical buckling pressure p_c in Eq. (2.1) as

$$n_{\text{crit}} = (a/t)(3\bar{E}_f / \bar{E}_s)^{1/3}.$$

(2.2)

where $\bar{E}_f = E_f / (1 - v_f^2)$ and $\bar{E}_s = E_s / (1 - v_s^2)$. In addition, Wang et al. (2009) conducted the nonlinear FEA to extract the surface wrinkle mode chart in terms of the surface morphology (i.e., the wavenumber n) against the stiffness (E_f/E_s) and aspect ratio (a/t) of the electrospun fibers. Yet, the corresponding critical mismatch strain was not predicted explicitly in their study.

17

Moreover, by using finite element method, Pai et al. (2009) conducted systematic simulations of nanofiber wrinkling to identify the correlations of critical strain to the corresponding circumferential wrinkle mode of the core-shell nanofibers at varying fiber geometries and elastic properties as observed in experiments. The simulation results can be utilized for active wrinkling control for desired surface morphologies in fiber fabrication and applications. Further justification is still needed on how to apply these theoretical predictions for the design and optimization of the surface wrinkle modes of electrospun fibers for various practical applications. Yet, how to actively control the surface wrinkling in nanofiber fabrication process has not been explored yet, and related intelligent mode-based numerical validation is still desired.

2.2. Inhomogeneous Swelling of Polymeric Hydrogels

2.2.1. Polymeric Hydrogels and Applications

Hydrogel, which is a three-dimensional (3D) network of cross-linked long polymer chains with hydrophilic branches or groups, is capable of large and reversible deformations. When a hydrogel is in contact with water, it is able to imbibe a large quantity of water from the environment and swell without dissolving (Tanaka, 1981; Shibayama & Tanaka, 1993; Kopeček, 2002; Ahmed, 2015; Zhao et al., 2008a; Hong et al., 2008b; Hong et al., 2009). The strong chemical cross-links prevent the long polymers from dissolving in the water and allow large elastic deformations of hydrogels, while the weak physical interconnection between the long polymer chains and water molecules arises viscous migration in hydrogels (Tanaka, 1981; Shibayama & Tanaka, 1993; Kopeček, 2002; Hong et al., 2008b; Hong et al., 2009; Ahmed, 2015).

18

Various hydrogels with broad tailorable functionalities have been under intensive investigations for decades including targeted molecular design and reversible synthesis from renewable natural polysaccharides and chitosan (Hennink & van Nostrum, 2002; Raschip et al., 2007; Popadyuk et al., 2014; Zholobko et al., 2014a; Zholobko et al., 2014b; Ahmed, 2015; Walker et al., 2019). Due to its hydrophilicity (comparable to biological tissues), softness (mechanical flexibility by tailorable network design), smartness, and ability to store a large amount of water, hydrogels have been extensively used for scaffolds for tissue engineering (Lee & Mooney, 2001; Nowak et al., 2002; Drury & Mooney, 2003; Luo & Shoichet, 2004; Wong et al., 2008; Jahani et al., 2018, 2020), vehicles for drug delivery (Fischel-Ghodsian et al., 1988; Jeong et al., 1997; Langer, 1998; Qiu & Park, 2001; Duncan, 2003; Peppas et al., 2006), sensors and actuators for optics and microfluidics (Beebe et al., 2000; Dong et al., 2006; Li et al., 2007; Sidorenko et al., 2007; Cho et al., 2008), model extracellular metrics for biological studies (Wichterle & Lim, 1960; Jagur-Grodzinski, 2006; Peppas, 2006; Discher, 2009; Ramzanpour et al., 2019, 2020a, 2020b; Hosseini Farid et al., 2019), and so on. Recent technological breakthroughs in hydrogels include synthesis of highly stretchable and tough hydrogels (Sun et al., 2012), which are able to contain ~90% water, to be stretched beyond 20 times their initial length, and have fracture energies of ~9,000 J/m^2, and hydrogel-based tough adhesives for diverse wet surfaces for use as tissue adhesives, wound dressings, and tissue repair (Li et al., 2017), among others.

2.2.2. Inhomogeneous and Anisotropic Equilibrium State in Swollen Hydrogels

According to the work by Hong et al. (2008b), two modes of large deformations can be considered for a gel (Figure 2-5). In the first mode, the gel changes its shape but not volume due

to the fast process of short-range rearrangement of molecules. But in the second mode, the gel changes both its shape and volume as a result of the slow process of long-range movement of water molecules. In the case of a sudden change in the environment (i.e., mechanical load), the hydrogel adjusts accordingly depending on the time limit. When it has a short-time limit, the hydrogel reaches the mechanical equilibrium but the water molecules inside the hydrogel do not have enough time to redistribute. At the long-time limit, the hydrogel reaches the equilibrium with both the mechanical load and the chemical potential of the water.
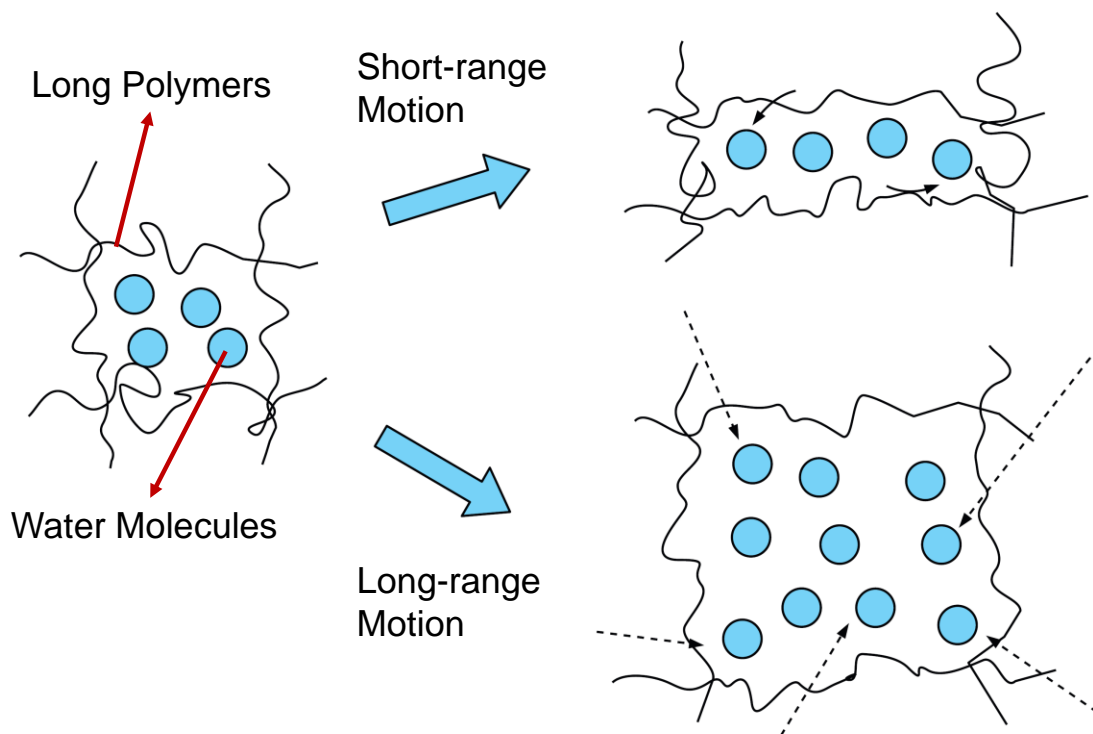
Figure 2-5. Schematic of two modes large of deformation in a gel (Hong et al., 2008b).

In this dissertation, the long-time limit of the hydrogel is assumed and considered in this study, in which the hydrogel achieves the state of equilibrium as the polymer network is in contact with the water molecules for a sufficiently long time. When a polymer network equilibrates with the environment in the absence of mechanical load or geometric constraint,

which rarely happens in practice, the hydrogel swells homogeneously and isotropically. As the mechanical load and/or geometric constraint are ubiquitous in the applications of hydrogels, inhomogeneous and/or anisotropic state of equilibrium occurs more commonly when the hydrogel is swelling (Hu et al., 1995; Kim et al., 2006; Klein et al., 2007; Zhao et al., 2008a; Ladet et al., 2008; Hong et al., 2009). Swelling in hydrogels can lead to a form of instability like debonding, wrinkling, creasing, cavitation, etc. (Southern & Thomas, 1965; Sidorenko et al., 2007; Hong et al., 2008a; Trujillo et al., 2008; Zhang et al., 2008; Hong et al., 2009).

In the view of applications, understanding of the responses (e.g., displacements, stresses, and water concentration) of hydrogels to external stimuli of either mechanical, chemical, electrical, electromagnetic loads or their combinations is crucial to design hydrogel-based functional materials and reliable soft devices/machines and predict relevant multifunctional performances (Peppas, 2000). Since the last decade, broad applications and research of soft materials have triggered the intensive research of swelling mechanics of hydrogels. Among others, Suo and his colleagues have formulated a set of rigorous field theories based on the work of Gibbs (1906) and Biot (1941) to delineate the nonlinear deformation and stress fields in hydrogel within the framework of continuum mechanics (Zhao et al., 2008b; Hong et al., 2008b; Hong et al., 2009; Hong et al., 2010), in which the Flory-Rehner free-energy function (Flory & Rehner Jr, 1943) is added as the contribution due to polymer network swelling and the mixture of water molecules and polymer chains after imbibing water. Suo's field theories of gels have been successfully used to solve various hydrogel swelling problems and can be conveniently implemented via designing user's subroutines into commercial finite element software packages as in nearly all the cases, the resulting problems are highly nonlinear. Only in a few simple cases, explicit semi-analytic solutions can be obtained. One example demonstrated by Zhao et al.

(2008a) was to consider a spherical shell of hydrogel bonded onto a hard core of another material as such core-shell structures have been fabricated in experimental studies (Pelton, 2000; Nayak & Lyon, 2005; Ballauff & Lu, 2007) and considered for potential applications of drug delivery (Ichikawa & Fukumori, 2000; Vodná et al., 2007), medical devices (Guo et al., 2005), controlled self-assembly (Nakahama & Fujimoto, 2002; Wei et al., 2006), etc. In their study, Zhao et al. (2008a) determined the nonlinear displacement, stress, and water concentration fields of the swollen spherical shell of hydrogel bonded onto a hard core after imbibing sufficient water. This problem was reduced into a two-point boundary value problem of a nonlinear 2nd-order ordinary differential equation (ODE) and solved numerically. Due to the geometrical constraint of the hard core, the resulting hydrogel is in an inhomogeneous and anisotropic equilibrium state.

In practice, composite hydrogels made of several hydrogels with tailorable material properties are desirable in achieving their optimal performances. Yet, no research has been reported yet in the literature on the swelling mechanics of composite hydrogels.

CHAPTER 3. CIRCUMFERENTIAL WRINKLING OF POLYMER NANOFIBERS

3.1. Introduction

In the practice of electrospinning, circumferential wrinkling is commonly observed in soft electrospun nanofibers. Yet, no theoretical model is available in the literature to explore the rational mechanisms of such surface instability in electrospun nanofibers such as the effects of surface energy and the threshold fiber diameter to trigger spontaneous circumferential wrinkling. This chapter is aimed to explore the critical condition to trigger circumferential wrinkling in polymer nanofibers under axial stretching. The content of the chapter is planned in the following. Section 3.2 is to formulate the nonlinear elasticity model to take into account the nonlinear elasticity, surface energy, and axial stretch of the soft nanofibers. As the first approach to understanding the surface instability, the soft nanofibers are treated as incompressible, isotropic, hyperelastic neo-Hookean solid, and the wrinkling condition is obtained via mathematical perturbation on the basis of the first principle of the nanofiber system. Section 3.3 is to conduct detailed numerical scaling analysis to demonstrate the correlation of critical axial stretch to the corresponding circumferential wrinkle mode. The threshold fiber radius to trigger the spontaneous circumferential wrinkling is determined in the limiting case of zero axial stretch. In consequence, concluding remarks of the present study are made in Section 3.4.

3.2. Model Formulation and Solutions

Consider a soft polymer nanofiber at its undisturbed stretch-free state as a thin, perfectly circular cylinder with the initial radius R_0. As mentioned above, the fast solvent evaporation in a thin polymer-solution jet during electrospinning may unavoidably induce the radial gradients of the material properties, microstructures, and residual stresses and strains in the nanofiber cross-

section. However, it is reasonable to consider these gradients as the secondary effects and assume the soft polymeric material of the fiber as an incompressible, isotropic, hyperelastic neo-Hookean solid. For the convenience of the discussion hereafter, three configurations are introduced to define the motion of a material point inside the fiber as shown in Figure 3-1:

1) Undisturbed stretch-free configuration (with surface tension ignored) (R, Θ, Z),

2) Pre-stretched configuration (with surface tension) (r, θ, z),

3) Current configuration (with circumferential wrinkles) ($\tilde{r}$, $\tilde{\theta}$, $\tilde{z}$).

In the following, the critical condition to trigger circumferential wrinkling is to be determined via linear perturbation of the elastic solution to the pre-stretched state of the soft polymer nanofiber in the current configuration.
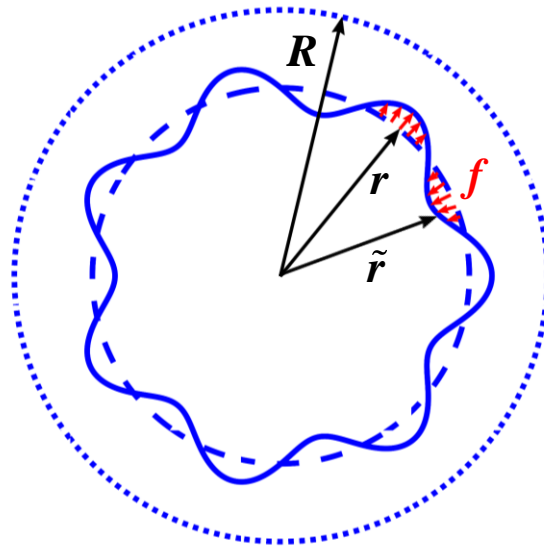
Figure 3-1. Coordinate systems of the undisturbed stretch-free configuration (R, Θ, Z), pre-stretched configuration (r, θ, z) without wrinkles, and current configuration ($\tilde{r}$, $\tilde{\theta}$, $\tilde{z}$) with circumferential wrinkles.

3.2.1. Thin Soft Polymer Nanofibers under Axial Pre-stretching

In the pre-stretched configuration, the soft polymer nanofiber is assumed under action of uniform axial stretching, and the solution to an axisymmetric deformation of the nanofiber can be expressed as (Wu & Dzenis, 2007a; Wu et al., 2008)

$$r = \lambda_1 R \quad (0 \le R \le R_0), \qquad \theta = \Theta \quad (0 \le \Theta \le 2\pi), \qquad z = \lambda_3 Z \quad (-\infty \le Z \le +\infty), \quad (3.1)$$

where λ_1 and λ_3 are the transverse and longitudinal stretches, respectively. The above deformation has the deformation gradient

$$\mathbf{F} = \begin{bmatrix} \dfrac{\partial r}{\partial R} & \dfrac{\partial r}{R\partial \Theta} & \dfrac{\partial r}{\partial Z} \\ \dfrac{r\partial \theta}{\partial R} & \dfrac{r\partial \theta}{R\partial \Theta} & \dfrac{r\partial \theta}{\partial Z} \\ \dfrac{\partial z}{\partial R} & \dfrac{\partial z}{R\partial \Theta} & \dfrac{\partial z}{\partial Z} \end{bmatrix} = \begin{bmatrix} \lambda_1 & 0 & 0 \\ 0 & \lambda_1 & 0 \\ 0 & 0 & \lambda_3 \end{bmatrix}. \qquad (3.2)$$

Material incompressibility of the polymer fiber gives the geometrical constraint of λ_1 and λ_3:

$$\lambda_1^2 \lambda_3 = 1. \qquad (3.3)$$

With the above deformations, the corresponding left Cauchy-Green tensor $\mathbf{B}$ is

$$\mathbf{B} = \mathbf{F}\mathbf{F}^T = \begin{bmatrix} \lambda_1^2 & 0 & 0 \\ 0 & \lambda_1^2 & 0 \\ 0 & 0 & \lambda_3^2 \end{bmatrix}. \qquad (3.4)$$

The three principal scalar invariants of $\mathbf{B}$ are

$$I_1 = 2\lambda_1^2 + \lambda_3^2 = 2\lambda_3^{-1} + \lambda_3^2, \qquad I_2 = 2\lambda_3 + \lambda_3^{-2}, \qquad I_3 = 1. \qquad (3.5)$$

In the present case, the soft nanofiber is treated as an incompressible, isotropic, hyperelastic neo-Hookean solid. Its constitutive relationship can be expressed in terms of Cauchy stress tensor $\mathbf{T}$ versus the left Cauchy-Green tensor $\mathbf{B}$ as

$$\mathbf{T} = -p\mathbf{I} + \mu\mathbf{B},\tag{3.6}$$

where p is the unknown hydrostatic pressure to be determined, and μ is the shear modulus. The stress tensor (3.6) can be further expressed in terms of stress components:

$$T_{rr} = T_{\theta\theta} = -p + \mu\lambda_1^2 = -p + \mu\lambda_3^{-1},\tag{3.7}$$

$$T_{zz} = -p + \mu\lambda_3^2,\tag{3.8}$$

$$T_{r\theta} = T_{rz} = T_{\theta z} = 0.\tag{3.9}$$

In terms of cylindrical coordinates, equilibrium equations of the axisymmetric fiber under uniform axial tension are

$$\frac{\partial T_{rr}}{\partial r} + \frac{T_{rr} - T_{\theta\theta}}{r} = 0,\tag{3.10}$$

$$\frac{\partial T_{\theta\theta}}{\partial \theta} = 0,\tag{3.11}$$

$$\frac{\partial T_{zz}}{\partial z} = 0.\tag{3.12}$$

In the above, two traction boundary conditions (BCs) are triggered at the fiber surface and along the fiber axis. In addition, surface tension produces a uniform radial compressive stress at the fiber surface as

$$T_{rr} = -\frac{\gamma}{r_0},\tag{3.13}$$

where γ (N/m) is the surface tension (surface energy) of the amorphous polymeric material and is assumed to be independent of the axial stretch and fiber radius, and r_0 is the fiber radius after deformation in the current configuration. Moreover, the force equilibrium along the fiber axis can be cast as

$$P = 2\pi \int_0^{r_0} r T_{zz} dr + 2\pi r_0 \gamma,\tag{3.14}$$

26

where P is the resultant of external axial tensile forces. By solving Eqs. (3.10) to (3.12) under traction conditions (3.13) and (3.14), the axial stress of the soft polymer nanofiber can be determined as

$$\frac{\sigma}{\mu} = \frac{P}{\pi r_0^2 \mu} = \lambda_3^2 - \frac{1}{\lambda_3} + \frac{l_0}{2r_0}, \tag{3.15}$$

where $l_0 = 2\gamma/\mu$ is the intrinsic length of the polymeric material. Eq. (3.15) can be further arranged as a function of the undisturbed radius of a stretch-free fiber (with surface tension ignored) by applying the deformation relation $r_0 = \lambda_1 R_0 = R_0 \lambda_3^{-1/2}$ as

$$\frac{\sigma}{\mu} = \frac{P}{\pi R_0^2 \mu} = \lambda_3 - \frac{1}{\lambda_3^2} + \frac{l_0}{2R_0} \frac{1}{\lambda_3^{1/2}}. \tag{3.16}$$

It can be concluded from the above derivations that under uniaxial tensile stress and surface tension, a soft nanofiber is in the triaxial stress state, and its three principal stress components at a material point are independent of the radial position of the fiber. Similar derivations have been considered in our previous studies of longitudinal wrinkling and wave propagation in soft polymer nanofibers (Wu et al., 2008; Wu, 2010).

3.2.2. Circumferential Wrinkling of Soft Polymer Nanofibers under Axial Stretching

Now let us consider the circumferential wrinkling deformation of a soft polymer nanofiber under uniform axial stretching as a small disturbance superimposed onto the elastic solution to the pre-stretched nanofiber as determined in Section 3.2.1. After wrinkling initiation on the nanofiber, a simple approach is to assume the coordinates of a material point in the current configuration as

$$\tilde{r} = [\lambda_1 + f(\Theta)]R, \qquad \tilde{\theta} = \Theta + g(\Theta), \qquad \tilde{z} = \lambda_3 Z, \tag{3.17}$$

27

where $f(\Theta)$ and $g(\Theta)$ are two small unknown disturbance functions satisfying BCs (3.13) and (3.14). It needs to be mentioned that choice of Eq. (3.17) belongs to one of the simplest possible incremental solutions of the present surface instability problem to avoid lengthy mathematical derivations based on a more general assumption of the possible displacement solutions as commonly used in nonlinear analysis of elastic instability (Taffetani & Ciarletta, 2015b; Ciarletta et al., 2016) while it can lead to practical, physically meaningful solutions. Thus, the corresponding deformation gradient matrix $\tilde{\mathbf{F}}$ and the left Cauchy-Green tensor $\tilde{\mathbf{B}}$ are

$$\tilde{\mathbf{F}} = \begin{bmatrix} \lambda_1 + f & f_\Theta & 0 \\ 0 & (\lambda_1 + f)(1 + g_\Theta) & 0 \\ 0 & 0 & \lambda_3 \end{bmatrix}, \tag{3.18}$$

$$\tilde{\mathbf{B}} = \tilde{\mathbf{F}}\tilde{\mathbf{F}}^T = \begin{bmatrix} (\lambda_1 + f)^2 + f_\Theta^2 & (\lambda_1 + f)(1 + g_\Theta)f_\Theta & 0 \\ (\lambda_1 + f)(1 + g_\Theta)f_\Theta & (\lambda_1 + f)^2(1 + g_\Theta)^2 & 0 \\ 0 & 0 & \lambda_3^2 \end{bmatrix}, \tag{3.19}$$

where f_Θ and g_Θ are derivatives of $f(\Theta)$ and $g(\Theta)$ with respect to Θ.

The scalar invariants of $\tilde{\mathbf{B}}$ above are

$$I_1 = (\lambda_1 + f)^2 + f_\Theta^2 + (\lambda_1 + f)^2(1 + g_\Theta)^2 + \lambda_3^2, \tag{3.20}$$

$$
\begin{aligned}
I_2 = {}& \frac{1}{2}\left[(\lambda_1 + f)^2 + f_\Theta^2 + (\lambda_1 + f)^2(1 + g_\Theta)^2 + \lambda_3^2\right]^2 - \frac{1}{2}\left[(\lambda_1 + f)^2 + f_\Theta^2\right]^2 \\
& -\frac{1}{2}(\lambda_1 + f)^4(1 + g_\Theta)^4 - (\lambda_1 + f)^2(1 + g_\Theta)^2 f_\Theta^2 - \frac{1}{2}\lambda_3^4
\end{aligned}
, \tag{3.21}
$$

$$I_3 = (\lambda_1 + f)^4(1 + g_\Theta)^2\lambda_3^2. \tag{3.22}$$

Material incompressibility of the polymer nanofiber in this state is

$$\det(\tilde{\mathbf{F}}) = 1, \tag{3.23}$$

which results in

$$(\lambda_1 + f)^2(1 + g_\Theta)\lambda_3 = 1. \tag{3.24}$$

The strain energy density for an incompressible, isotropic, hyperelastic neo-Hookean solid is

$$e = \frac{\mu}{2}(I_1 - 3), \tag{3.25}$$

where I_1 is the first principal invariant of $\tilde{\mathbf{B}}$, and μ is the shear modulus of the neo-Hookean solid as given in (3.6). Hence, the potential energy functional Π of the soft polymer nanofiber under uniaxial axial stretching and surface tension has the form

$$\Pi = \iiint e\tilde{r}d\tilde{\theta}d\tilde{r}d\tilde{z} + \iint \gamma\left(\tilde{r}^2 + \tilde{r}_\theta^2\right)^{1/2} d\tilde{\theta}d\tilde{z} - \int Pd(\tilde{z} - Z), \tag{3.26}$$

which can be expressed in terms of the coordinates defined in the configuration of undisturbed stretch-free fiber as

$$\Pi = \frac{1}{2}R_0^2 Z \int_\Theta ed\Theta + R_0 Z \int_\Theta \frac{\gamma}{\lambda_1 + f}d\Theta - PZ(\lambda_3 - 1), \tag{3.27}$$

where the higher-order terms in the 2nd integral of the surface energy have been ignored. By substituting (3.20) to (3.25) into (3.27), applying the functional variation on Eq. (3.27), evoking the material incompressibility (3.3), and finally ignoring the higher-order terms, a standard 2nd-order linear ordinary differential equation (ODE) of constant coefficients can be obtained as

$$R_0\mu\lambda_3^{1/2}f_{\Theta\Theta} - R_0(4\mu\lambda_3^{1/2} - 2\frac{\gamma}{R_0}\lambda_3^2)f + 2\gamma\lambda_3^{3/2} = 0. \tag{3.28}$$

Eq. (3.28) indicates that the condition to trigger circumferential wrinkling on a soft polymer nanofiber under uniform axial stretching is governed by the material elasticity, surface energy, initial fiber radius and axial stretch of the nanofiber. Furthermore, Eq. (3.28) can be recast as

29

$$Af_{\Theta\Theta} + Bf + C = 0, \tag{3.29}$$

where coefficients A, B, and C can be related to the material elasticity, surface energy, applied pre-stretch, and fiber geometry (radius) such that

$$A = R_0 \mu \lambda_3^{1/2}, \tag{3.30}$$

$$B = -R_0 (4\mu\lambda_3^{1/2} - 2\frac{\gamma}{R_0}\lambda_3^2), \tag{3.31}$$

$$C = 2\gamma\lambda_3^{3/2}. \tag{3.32}$$

Surface wrinkling on a soft polymer nanofiber can be determined by seeking periodic solutions to the homogeneous Eq. (3.29) as

$$Af_{\Theta\Theta} + Bf = 0. \tag{3.33}$$

Consider a periodic solution to (3.33) along the circumference with respect to Θ as

$$f(\Theta) = A_0 \exp(ik\Theta), \tag{3.34}$$

where A_0 is the complex amplitude of surface disturbance, and k is the wavenumber of the wrinkles. Consequently, substituting (3.34) into (3.33) leads to the wavenumber k as

$$k = \sqrt{B/A}, \tag{3.35}$$

which must be a positive number to ensure a physically meaningful circumferential wrinkle mode on the fiber surface. Therefore, the condition of surface wrinkling on soft rubbery polymer nanofibers is

$$B/A > 0, \tag{3.36}$$

which can be expressed in terms of material properties μ and γ, geometry R_0 and longitudinal stretch λ_3 as

$$\frac{R_0}{\lambda_3^{3/2}} < \frac{\gamma}{2\mu}. \tag{3.37}$$

Eq. (3.37) elucidates the scaling properties among initial fiber radius, material properties, and axial stretch for circumferential wrinkling of soft polymer nanofibers under axial stretching.

3.3. Numerical Examples and Discussions

3.3.1. Axial Stress of Pre-stretched Soft Polymer Nanofibers

In the cases of the intrinsic length taking l_0 = 50, 200, 500, and 1,000 nm and the initial fiber radius taking R_0 = 50, 100, 200, 500, and 1,000 nm, respectively, Eq. (3.16) predicts the dimensionless axial tensile stress σ/μ as shown in Figures 3-2 to 3-5. In common sense, the axial stress increases with increasing axial stretch. In addition, Figures 3-2 to 3-5 also indicate that l_0 has an increasing influence on the stress variation with increasing amplitude of l_0, which demonstrates the strong size effect in soft rubbery nanofibers. In the particular case of l_0 = 1,000, as shown in Figure 3-5, the soft nanofiber with a diameter of 50 nm exhibits longitudinal elastic instability.
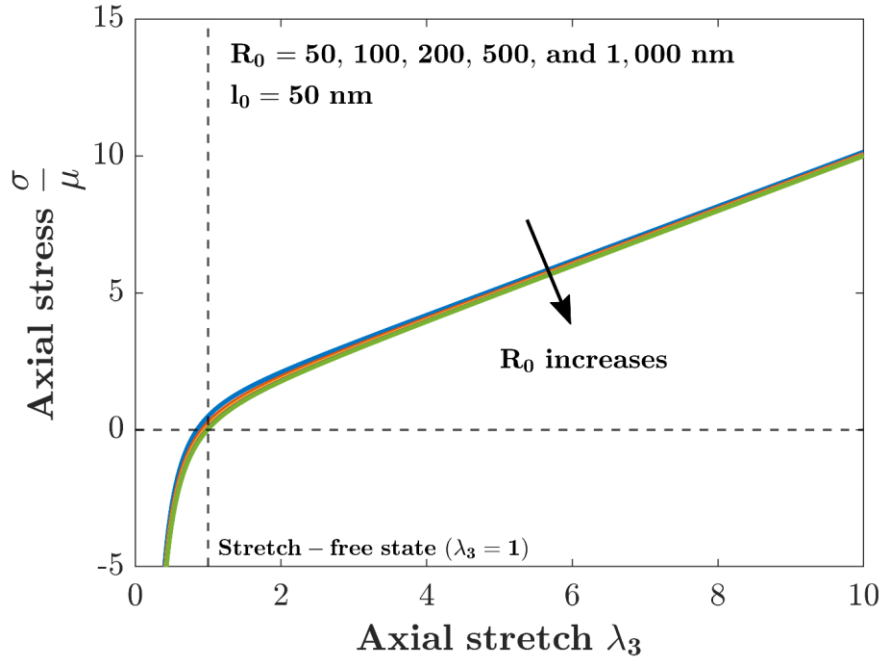
Figure 3-2. Variation of the dimensionless axial stress of pre-stretched soft nanofibers with respect to the axial stretch λ_3 at intrinsic length $l_0 = 50$ nm and five initial fiber radii ($R_0 = 50$, 100, 200, 500, and 1,000 nm).
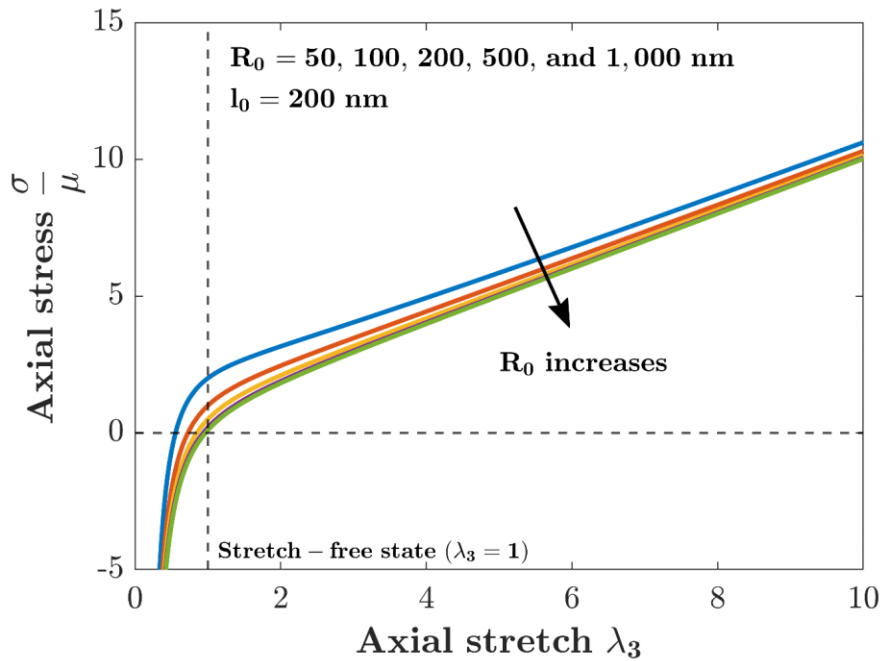
Figure 3-3. Variation of the dimensionless axial stress of pre-stretched soft nanofibers with respect to the axial stretch λ_3 at intrinsic length $l_0 = 200$ nm and five initial fiber radii ($R_0 = 50$, 100, 200, 500, and 1,000 nm).
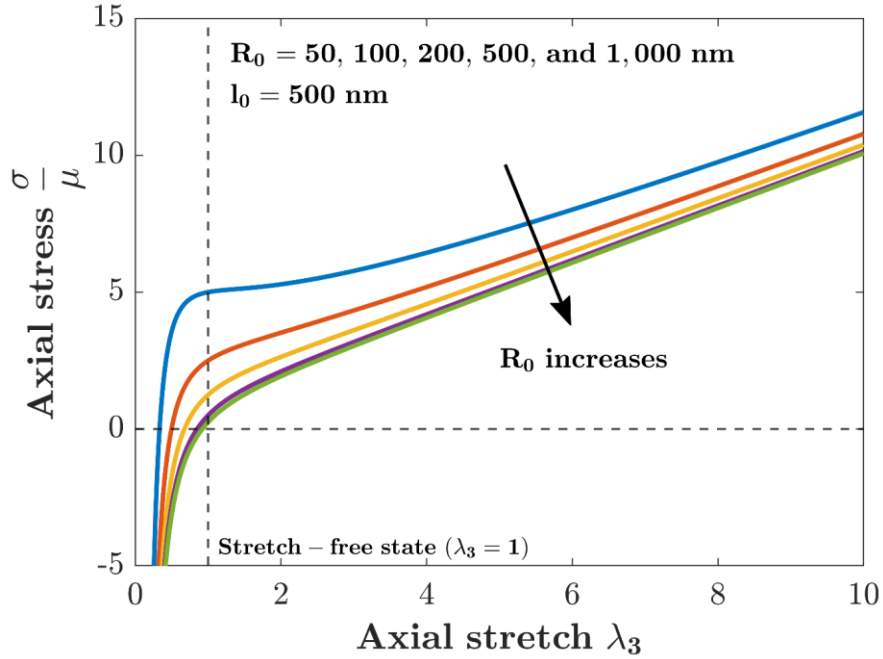
Figure 3-4. Variation of the dimensionless axial stress of pre-stretched soft nanofibers with respect to the axial stretch λ_3 at intrinsic length $l_0 = 500$ nm and five initial fiber radii ($R_0 = 50$, 100, 200, 500, and 1,000 nm).
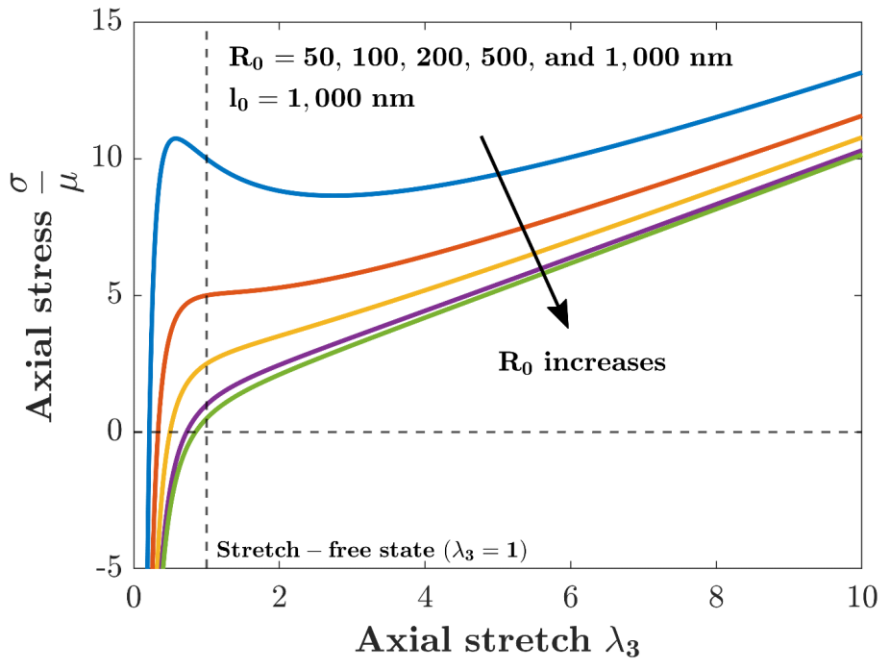
Figure 3-5. Variation of the dimensionless axial stress of pre-stretched soft nanofibers with respect to the axial stretch λ_3 at intrinsic length $l_0 = 1,000$ nm and five initial fiber radii ($R_0 = 50$, 100, 200, 500, and 1,000 nm).

3.3.2. Critical Condition of Circumferential Wrinkling in Soft Polymer Nanofibers

Eq. (3.36) indicates that the critical condition of surface wrinkling is $B = 0$, which results in the critical axial stretch as

$$\lambda_3 = (4\frac{R_0}{l_0})^{2/3}. \tag{3.38}$$

Yet, it needs to be mentioned that this critical stretch λ_3 only corresponds to $k = 0$, i.e., a mathematical critical condition for surface instability (wrinkling). For those physically meaningful wave numbers $k > 0$, $k = 1$ corresponds to a circular cross-sectional configuration; $k = 2$ corresponds to an elliptic cross-sectional configuration. Thus, it is reasonable to assume that the critical stretch λ_3 is the one that triggers the first physically meaningful wrinkle mode with $k = 2$, i.e.,

$$k = \sqrt{B/A} = 2. \tag{3.39}$$

Plugging (3.30) and (3.31) into (3.39) results in

$$\lambda_3 = (8\frac{R_0}{l_0})^{2/3}, \tag{3.40}$$

which is $2^{2/3} \approx 1.5874$ times the one predicted by Eq. (3.38).

Figure 3-8 illustrates the critical axial stretch λ_3 based on (3.40) with increasing initial fiber radius R_0 at four intrinsic lengths of $l_0 = 50, 200, 500,$ and $1,000$ nm, respectively. Given the value of R_0, the critical axial stretch λ_3 decreases rapidly with increasing l_0, i.e., the size effect is significant in the critical axial stretch λ_3 to trigger circumferential wrinkling. More noticeably, at small nanofiber sizes a large intrinsic length l_0 may evoke spontaneous wrinkling,

i.e., surface circumferential wrinkling may be directly evoked by surface energy without axial stretching and even under axial compression ($\lambda_3 < 1$).
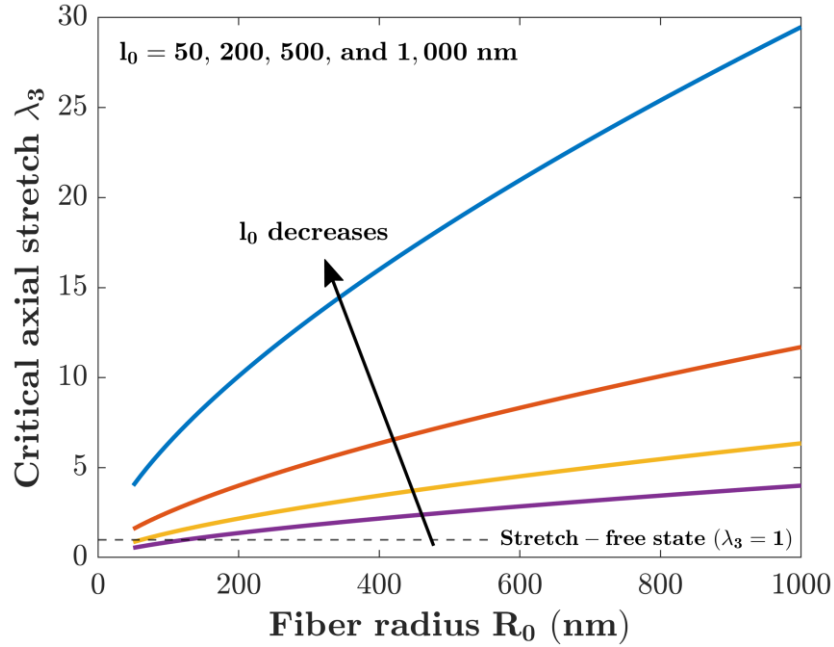
Figure 3-6. Variation of the critical axial stretch λ_3 with respect to varying fiber radius R at four different intrinsic lengths (l_0 = 50, 200, 500, and 1,000 nm, respectively) based on Eq. (3.40).

3.3.3. Critical Radii for Circumferential Wrinkling in Soft Polymer Nanofibers

Eq. (3.40) can further determine the critical fiber radius R_C to trigger circumferential wrinkling ($k = 2$) at the stretch-free condition, i.e. $\lambda_3 = 1$, such that

$$R_C = \frac{\gamma}{4\mu}. \tag{3.41}$$

Eq. (3.41) indicates that circumferential wrinkling of soft polymer nanofibers may happen without applying any axial tensile stretch, i.e., spontaneous circumferential wrinkling, if the initial fiber radius is smaller than the critical fiber radius R_C as also shown in Figure 3-6. This critical fiber radius R_C depends only on the surface energy and elastic properties of the soft

35

nanofiber, and is irrelevant to the material and process parameters adopted in an electrospinning process. In addition, by comparison with R_C to trigger spontaneous longitudinal wrinkling in soft nanofibers by Wu et al. (2008) and Wu (2010), i.e., $R_C = \gamma/(6\mu)$ after converting into the current neo-Hookean material model, it is found that R_C to trigger spontaneous circumferential wrinkling is 1.5 times that to trigger spontaneous longitudinal wrinkling. This demonstrates that spontaneous circumferential wrinkling occurs earlier than spontaneous longitudinal wrinkling in electrospun nanofibers as the electrospinning jet is shrinking from a larger size to a smaller one and wrinkling satisfying the critical condition at a large fiber radius first occurs. Thus, spontaneous circumferential wrinkles can be observed more often in electrospun soft nanofibers, which has been broadly validated in electrospinning experiments with one sample as shown in Figure 2-3.

3.3.4. Wavenumber (Wrinkle Mode) for Circumferential Wrinkling in Soft Polymer Nanofibers

Substitution of Eqs. (3.30) and (3.31) into (3.35) leads to the wavenumber k (wrinkle mode) of a compliant nanofiber as

$$k = \sqrt{-4 + \frac{l_0}{R_0} \lambda_3^{3/2}} \; . \tag{3.42}$$

Figure 3-6 shows the numerical scaling analysis of the dependencies of the wavenumber k upon the axial stretch λ_3 at five initial fiber radii R_0 and four intrinsic lengths l_0 as adopted in Section 3.3.1, respectively. Herein, wavenumbers $k = 1$ and 2 correspond to the circular and elliptical nanofiber cross-sections, respectively. The physically meaningful wrinkle modes can be considered for those with wavenumbers $k \geq 2$.

Figures 3-7 to 3-10 show variations of the wavenumber k (wrinkle mode) of soft nanofibers with respect to varying axial stretch λ_3 at five different initial fiber radii R_0 and four intrinsic lengths l_0, respectively. Given the values of R_0 and l_0, k increases in a slightly nonlinear feature with increasing λ_3. In addition, at a fixed value of λ_3, k increases with either increasing l_0 or decreasing R_0, i.e., the smaller soft nanofiber radii, the more do the circumferential surface wrinkles appear. Figures 3-7 to 3-10 also indicate that axial stretching can be utilized to tune the circumferential wrinkling in soft nanofibers and then rationally modify the surface morphology and specific surface area of the soft nanofibers for promising applications of gas/liquid filtration, water-oil separation, biological tissue scaffolding, etc. In principle, surface morphology can be actively altered to optimize the surface wetting performance of nanofiber mats (Zhou & Wu, 2015) according to Wenzel and Cassie and Baxter models for patterned superhydrophobic surfaces (Wenzel, 1936, 1949; Cassie & Baxter, 1944).
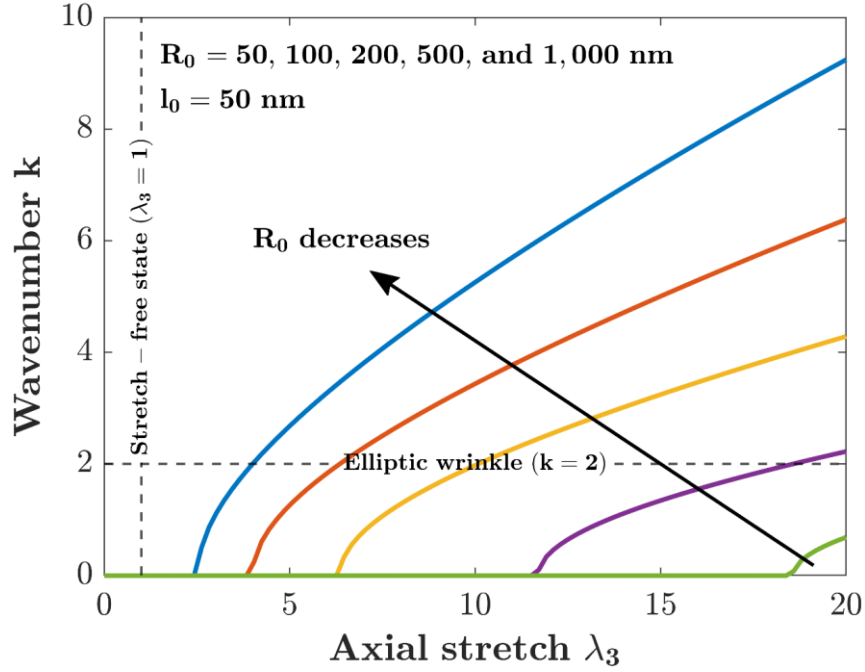
Figure 3-7. Variation of the wavenumber k (wrinkle mode) of soft nanofibers with respect to varying axial stretch λ_3 at intrinsic length $l_0 = 50$ nm and five different initial fiber radii ($R_0 = 50, 100, 200, 500$, and $1,000$ nm).
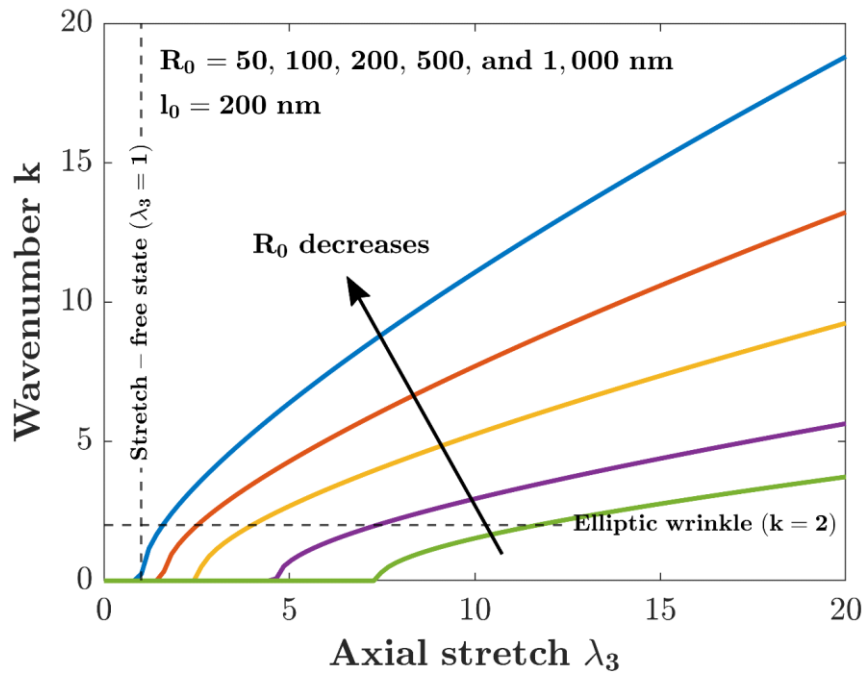
Figure 3-8. Variation of the wavenumber k (wrinkle mode) of soft nanofibers with respect to varying axial stretch λ_3 at intrinsic length $l_0 = 200$ nm and five different initial fiber radii ($R_0 = 50, 100, 200, 500$, and $1,000$ nm).
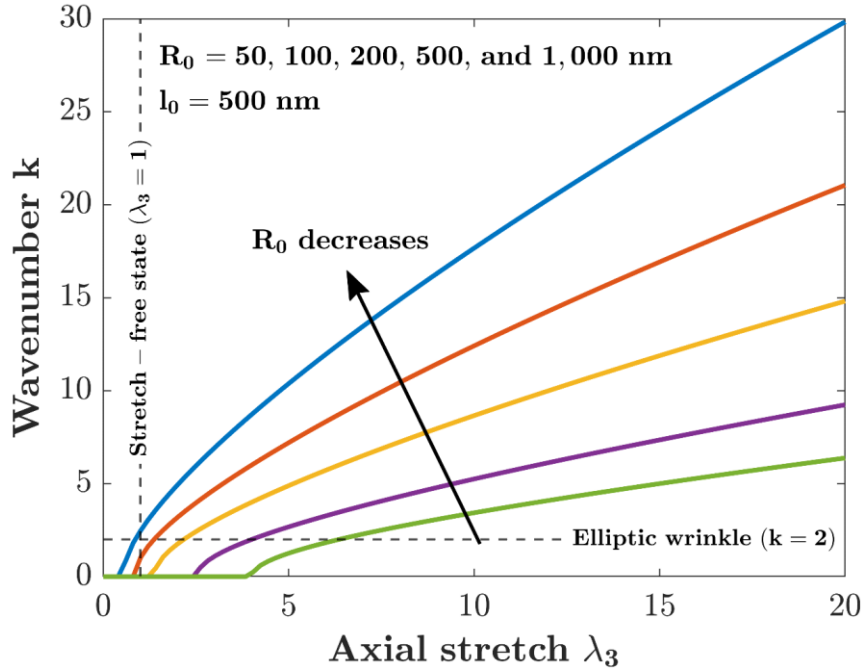
Figure 3-9. Variation of the wavenumber k (wrinkle mode) of soft nanofibers with respect to varying axial stretch λ_3 at intrinsic length l_0 = 500 nm and five different initial fiber radii (R_0 = 50, 100, 200, 500, and 1,000 nm).
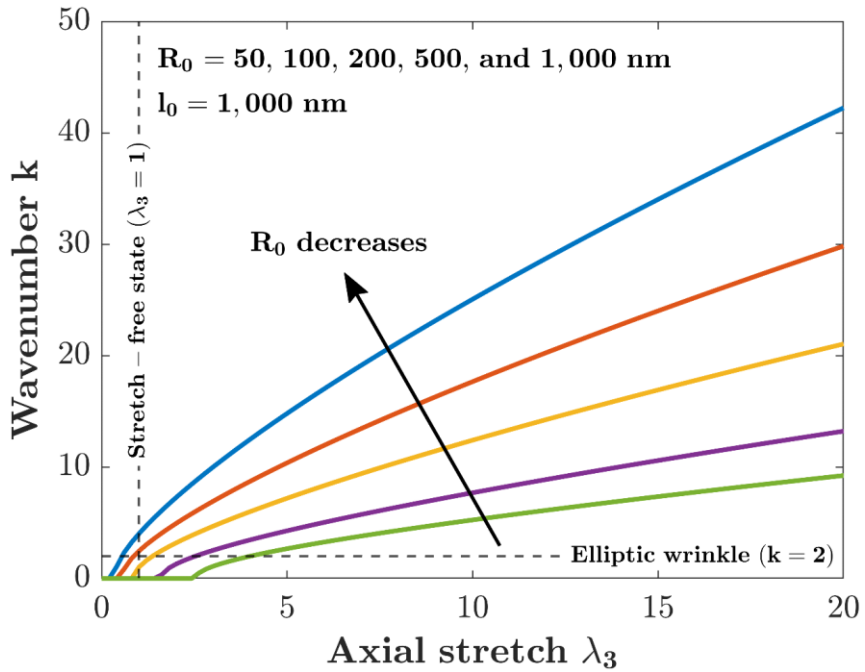
Figure 3-10. Variation of the wavenumber k (wrinkle mode) of soft nanofibers with respect to varying axial stretch λ_3 at intrinsic length l_0 = 1,000 nm and five different initial fiber radii (R_0 = 50, 100, 200, 500, and 1,000 nm).

Nevertheless, substantial experimental data are still desired for surface energy, mechanical properties, and drying induced residual strains across the electrospun polymer nanofibers. Thus, quantitative model validation is still pending at this stage though the present model is able to qualitatively predict the existence of circumferential wrinkling and to indicate the crucial role of surface energy in dominating the surface wrinkling phenomenon in electrospun polymer nanofibers. Additional model refinements and validation are expected once sufficient experimental data of soft polymer nanofibers are available.

3.3.5. Special Case of Infinitesimal Deformation in Soft Polymer Nanofibers

In the special case of simple uniaxial tension with zero deformation, $\lambda_3 = 1$ (i.e., infinitesimal deformation), by considering the constitutive Eqs. (3.7) and (3.8), the tangential modulus E_T of the material can be determined as

$$E_T = 3\mu , \tag{3.43}$$

and by considering the axial tensile stress (3.16)

$$\frac{\sigma}{\mu} = \frac{l_0}{2R_0} = \frac{\gamma}{\mu R_0} , \tag{3.44}$$

the critical radius for an infinitesimal deformation can be determined as

$$R_C = \frac{\gamma}{\sigma} . \tag{3.45}$$

Eq. (3.45) indicates that infinitesimal deformation of soft polymer nanofibers may happen for fibers smaller than R_C, which can also be rewritten as

$$R_C = \frac{\gamma}{E_T (\lambda_3 - 1)} , \tag{3.46}$$

for $\lambda_3 \neq 1$. For $\lambda_3 > 1$ (i.e., axial stretch), the right side value gets smaller than R_C and small elastic deformations start to appear on the polymer fiber. For $\lambda_3 < 1$ (i.e., axial compression), the right side value gets larger than R_C and prevents any deformation on the polymer fiber.

3.4. Concluding Remarks

In this study, the mechanism of circumferential surface wrinkling of soft polymer nanofibers under axial stretching has been explored via forming a simple 1D continuum mechanics model. During the process, the possible radial gradients of the mechanical properties in the fiber cross-section were ignored, and the material of the soft polymer nanofibers was treated as homogeneous, isotropic, hyperelastic neo-Hookean solid. The governing ODE for circumferential wrinkling has been determined. The critical axial stretch to trigger circumferential wrinkling and the critical initial fiber radius to evoke spontaneous circumferential wrinkling have been extracted in explicit expressions. Detailed numerical scaling analysis has been performed to illustrate the dependencies of critical axial stretch and critical fiber radius upon the material properties and geometries of the soft nanofibers. The present study provides the rational basis of circumferential wrinkling phenomenon commonly observed in soft polymer nanofibers produced by electrospinning. The present modeling study also demonstrated a potential technique to actively tune the surface morphology of soft polymer nanofibers via axial stretching to induce circumferential wrinkling. The present theorical study can be helpful for the applications where the surface morphology of the polymer nanofiber has an important role in that particular application, e.g., high-grade gas/liquid filtration, polymer nanocomposites, wound dressing, tissue scaffolding, drug delivery, and renewable energy harvesting, conversion, and storage, etc.

CHAPTER 4. TUNABLE WRINKLE MODES OF CORE-SHELL POLYMER FIBERS IN ELECTROSPINNING

4.1. Introduction

As it has been mentioned before, wrinkled surfaces are commonly observed on ultrathin polymer fibers produced in electrospinning process. Yet, the corresponding critical mismatch strain, which leads to the circumferential wrinkling in electrospun nanofibers with glassy shell and sol-gel core, has not been predicted yet for the design and optimization of the surface winkle modes of electrospun fibers for various practical applications. As a viable experimental approach, this chapter proposes to incorporate hard cores (e.g., carbon nanotubes (CNTs), silica particles, etc.) into polymer nanofibers via coaxial electrospinning, i.e., co-electrospinning (Figure 4-1), to intelligently alter the surface wrinkle modes of the resulting core-shell nanofibers. In this chapter, a continuum mechanics model and related FEA is formulated to explore the dependencies of surface wrinkle modes of the core-shell polymer fibers upon the thickness and stiffness of the glassy shell and inner soft sol-gel layers. Detailed discussions on the wrinkling mechanisms are made and conclusions of the present study are drawn in consequence.
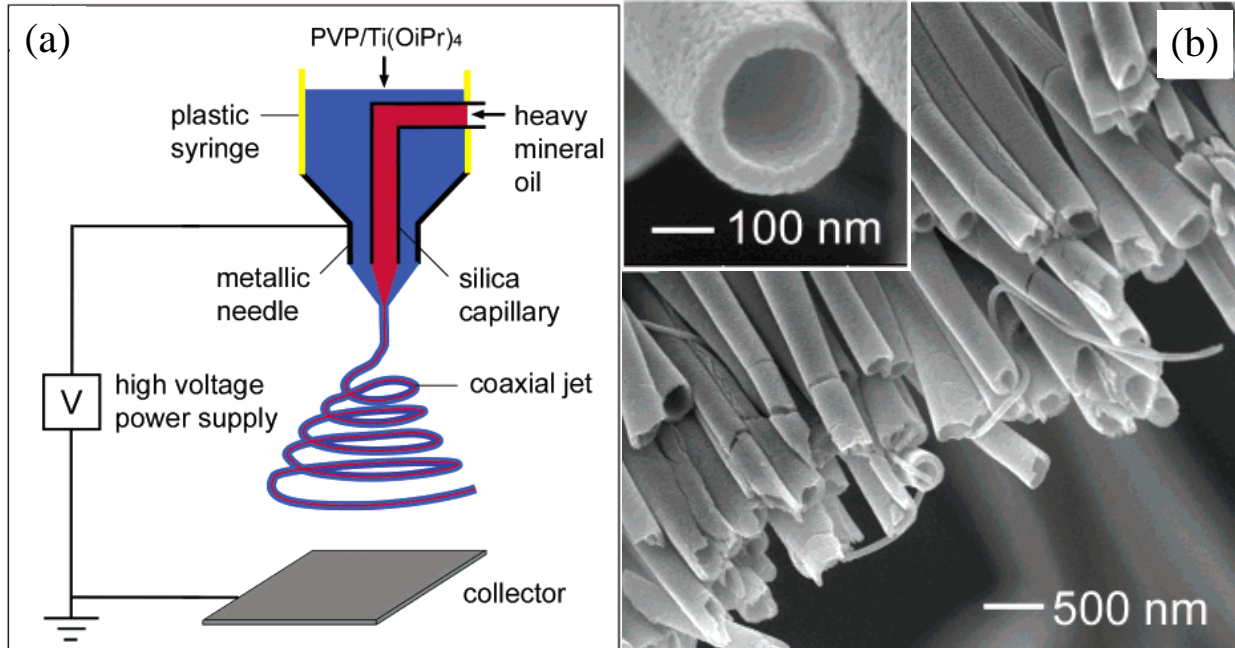
Figure 4-1. Nanotube formation using coaxial electrospinning: (a) Schematic coaxial electrospinning process; (b) SEM image of a uniaxially aligned array of TiO2 hollow fibers (Li & Xia, 2004a).

4.2. Problem Statement and Solution

Beyond control of the solvent evaporation in electrospinning, herein we formulate a continuum mechanics model to explore the potential of actively altering the surface wrinkle modes of electrospun fibers via introducing a second phase of an artificial hard core. This approach can be realized by means of co-electrospinning, in which hard micro/nanoparticles (e.g., CNTs, silica micro/nanoparticles, etc.) can be conveniently enwrapped into the electrospun fibers as the hard core via feeding these particles into the inner jet in co-electrospinning process. Therefore, in the jet whipping stage, the fast drying-induced glassy shell, the inner sol-gel layer and the hard core of enwrapped hard particles can be modeled as a tri-layered cylinder, as illustrated in Figure 4-2, to study the surface wrinkling initiation and regulation. The fast drying (solvent evaporation) of the surface skin (shell) and solvent diffusion in the jet results in the radial solvent-concentration gradient across the jet, leading to the excessive circumferential

43

compressive strain in the initially dried shell and finally triggering surface wrinkling when the critical buckling conditions are reached.

(a) Reference state

(b) Boundary conditions

(c) Patterned state
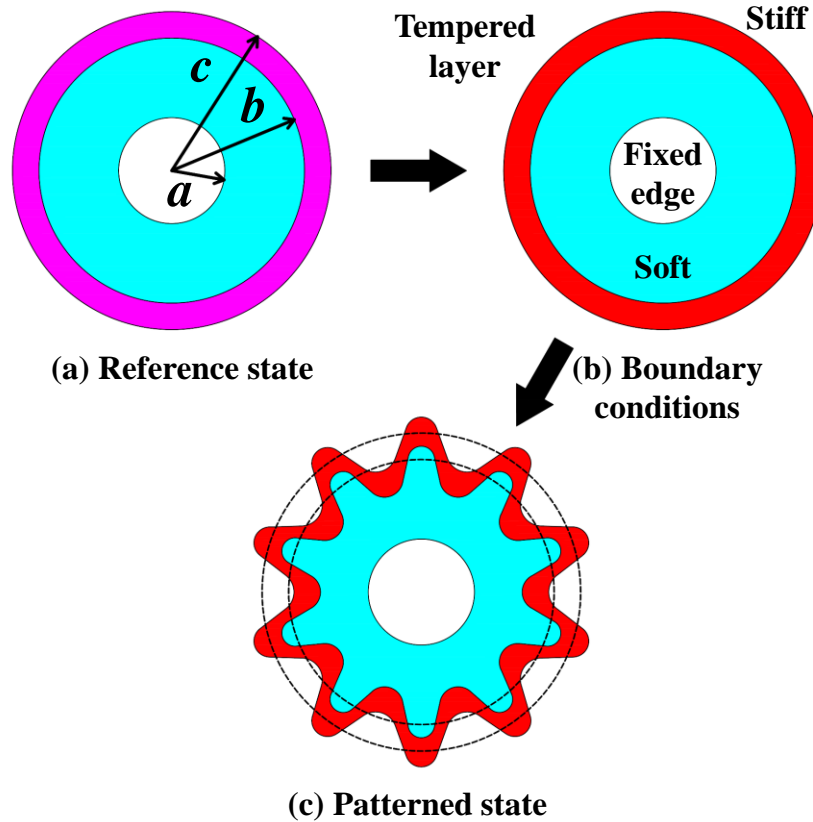
Figure 4-2. Schematic cross-section of a tri-layered electrospun fiber and surface winkling. (*a*) Initial reference state, (*b*) boundary conditions, and (*c*) surface wrinkling due to circumferential strain mismatch.

To explore the dependencies of the circumferential wrinkle modes upon the geometries and stiffness of the glassy shell and inner soft sol-gel layer on a hard core in co-electrospinning, nonlinear FEA is utilized for the wrinkling analysis for the present study. During the computational process, the glassy shell and inner soft sol-gel layer of the fiber are modeled as two incompressible hyperelastic neo-Hookean solids with different shear modulus μ. The strain energy density W of a hyperelastic neo-Hookean solid is given as

$$W = \frac{\mu}{2}\left(\lambda_1^2 + \lambda_2^2 + \lambda_3^2 - 3\right). \tag{4.1}$$

where $\mu = \mu_f$ for the glassy shell (film), $\mu = \mu_s$ for the inner sol-gel layer (substrate), and λ_1, λ_2 and λ_3 are the three principal stretches of the fiber along the radial r, circumferential θ, and axial z directions, respectively (Zhao & Zhao, 2017; Cowin & Doty, 2007). Without loss of generality, it is assumed that the fiber is in the plane-strain state as any existing axial strain along the fiber axis (z-axis) can be converted into the strains in the fiber cross-section according to material incompressibility of the neo-Hookean solids, which implies $\lambda_1 = 1/\lambda$, $\lambda_2 = \lambda$, and $\lambda_3 = 1$ with λ as a function with respect to r and θ. In reality of electrospinning, axial strain always exists and varies with jet elongation while surface wrinkling happens at the late whipping stage as the shell starts to solidify. By comparison with drying-induced circumferential strain mismatch, the axial strain does not dominate the surface wrinkling process in electrospun fibers. Hereafter, the computational nonlinear buckling (wrinkling) analysis is implemented by using a commercial FEA software package (ANSYS®) as follows. For a typical simulation, given the fiber aspect ratios a/c and t_f/t_s ($t_f = c - b$ and $t_s = b - a$), as shown in Figure 4-2(a), and the stiffness ratio μ_f/μ_s of the glassy shell to the inner soft layer, the hard core of radius a is modeled as a rigid body in FEA via applying fixed displacement boundary conditions (BCs) at the core surface; the initial "seeded" compressive strains in the glassy shell is made through applying an artificial thermal volumetric strain in the shell. Varying aspect ratios a/c and t_f/t_s as well as stiffness ratio μ_f/μ_s are employed in the computational simulations to examine the effects of the hard core of varying radius as well as the polymer-solvent system of varying solvent fraction and evaporation rate in co-electrospinning. Numerical results gained from the

45

computational simulation include the minimum critical compressive strain (ε_c) in the glassy shell and the corresponding wave number n of the surface wrinkle modes. In a realistic co-electrospinning process, the aspect ratios a/c and t_f/t_s and stiffness ratio μ_f/μ_s are governed by the process parameters, polymer-solvent system, and the jet drying rate, which further determine the residual compressive strain ε_r (i.e., the circumferential strain mismatch) in the glassy shell. Once ε_r in the shell is equal or larger than the critical wrinkling strain ε_c to evoke circumferential surface wrinkling, the predicted wrinkle mode with the wavenumber n is expected to be observable in electrospinning, as illustrated in Figure 4-2(c).

During the computational simulation, a variety of combinations of the aspect ratios (a/c and t_f/t_s), as shown in Figure 4-3, and stiffness ratio (μ_f/μ_s) are employed to examine the parameter effects of varying drying rates and polymer-solvent systems in the sense of physics. Three values of a/c (i.e., 0.25, 0.5, and 0.75) are considered to represent three types of hard core, i.e., small-, medium- and large-sized hard cores; for each a/c, four values of t_f/t_s (i.e., 0.1, 0.25, 0.5, and 1.0) are utilized to stand for four different types of polymer-solvent systems (with different drying rates). Furthermore, for each combination of a/c and t_f/t_s, three values of μ_f/μ_s (i.e., 10, 100, and 1,000) are employed in the computational simulations. As aforementioned, the values of t_f/t_s and μ_f/μ_s are employed to phenomenologically represent the relevant geometrical and elastic properties of the polymer-solvent system in co-electrospinning as the exact dependency is not available yet from the literature. Figures 4-4 to 4-6 show the critical surface wrinkle mode charts in terms of the wavenumber n (the lowest) and surface topology against the aspect ratio t_f/t_s and stiffness ratio μ_f/μ_s for $a/c = 0.25$, 0.5, and

0.75, respectively, in which the color contours of wrinkled fiber cross-sections represent the in-plane characteristic deformations in the fiber cross-section after wrinkling (i.e., eigen-deformation). It can be observed from Figure 4-4 that given the size of a hard core (a/c), the wavenumber n (i.e., the number of surface wrinkles) decreases from $n = 10$ to 3 with increasing either stiffness ratio μ_f/μ_s from 10 to 1,000 or fiber aspect ratio t_f/t_s from 0.1 to 1. This observation has a clear physical picture in co-electrospinning as a high stiffness ratio μ_f/μ_s and/or a high fiber aspect ratio t_f/t_s are directly correlated to a high gradient of solvent concentration across the fiber, i.e., a fast solvent evaporation (drying), which generally leads to a shaped electrospun fiber with fewer surface wrinkles (i.e., a lower value of the wavenumber n) as evidenced in electrospinning experiments (Koombhongse et al., 2001; Pai et al., 2009; Wang et al., 2009). In addition, within the framework of continuum mechanics (Herrmann & Forrestal, 1965; Wang et al., 2009), it has been shown that once buckled, a stiffer and thicker surface layer attached onto a compliant substrate under in-layer compression generally generates surface wrinkles with a smaller wavenumber n, i.e., a large wavelength. As a conclusion, the reduction of the solvent evaporation rate (drying rate) in electrospinning or more even drying across the jet (i.e., the lower μ_f/μ_s and t_f/t_s ratios) generally produces micro/nanofibers with more wrinkled surfaces (i.e., a higher wavenumber n).
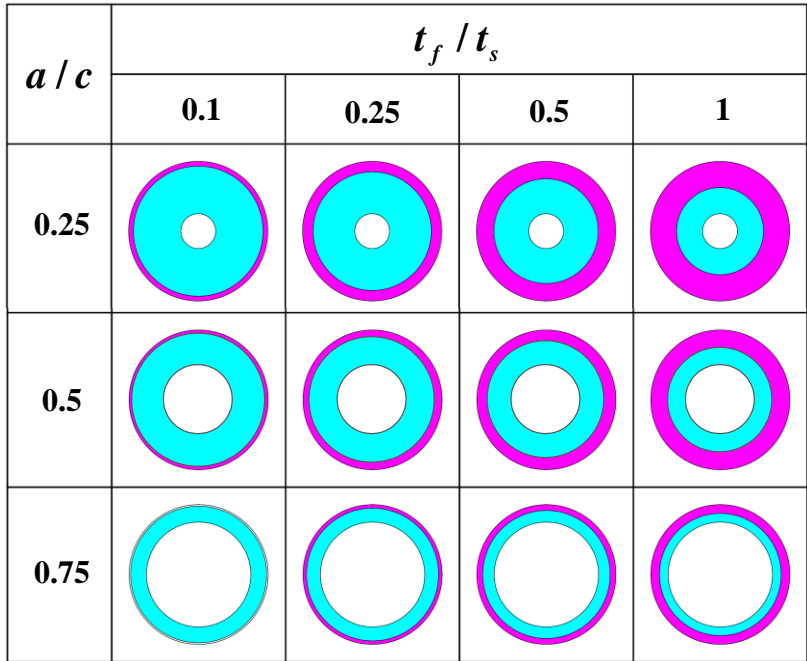
Figure 4-3. Schematic cross-section geometries of electrospun core-shell fibers of varying aspect ratios a/c and t_f/t_s used in computational wrinkling analysis.
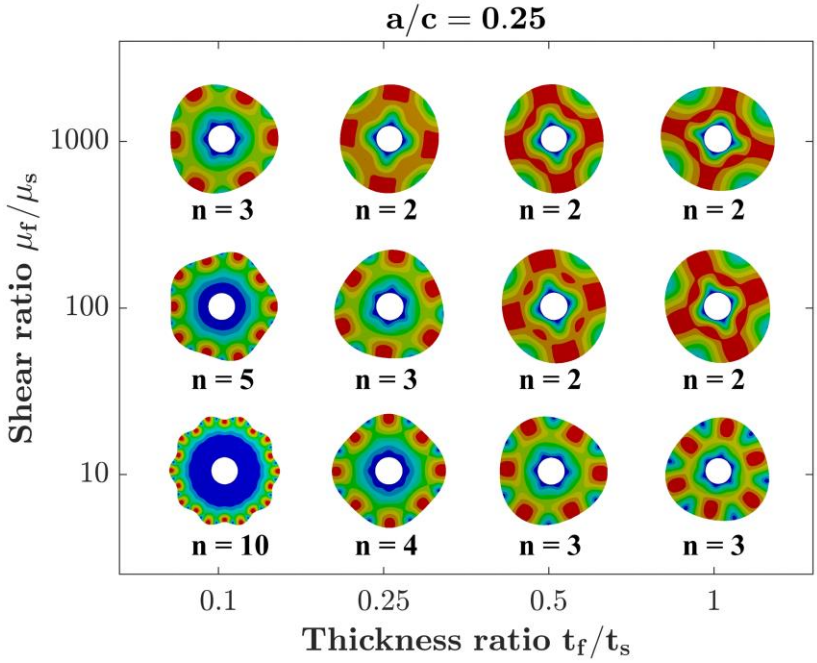
Figure 4-4. Critical surface wrinkle mode charts in terms of the wavenumber n and surface topology against the aspect ratio t_f/t_s and stiffness ratio μ_f/μ_s for $a/c = 0.25$.
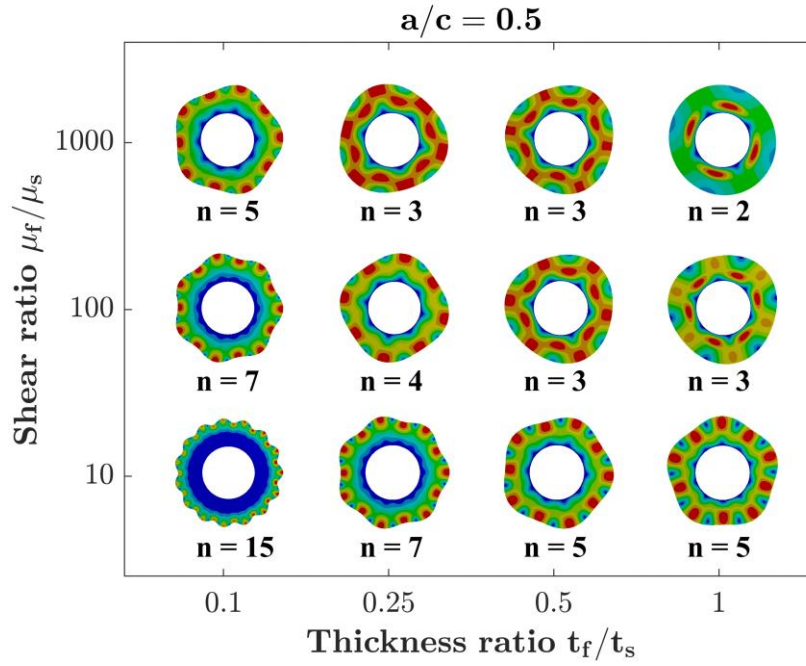
Figure 4-5. Critical surface wrinkle mode charts in terms of the wavenumber n and surface topology against the aspect ratio t_f/t_s and stiffness ratio μ_f/μ_s for $a/c = 0.5$.
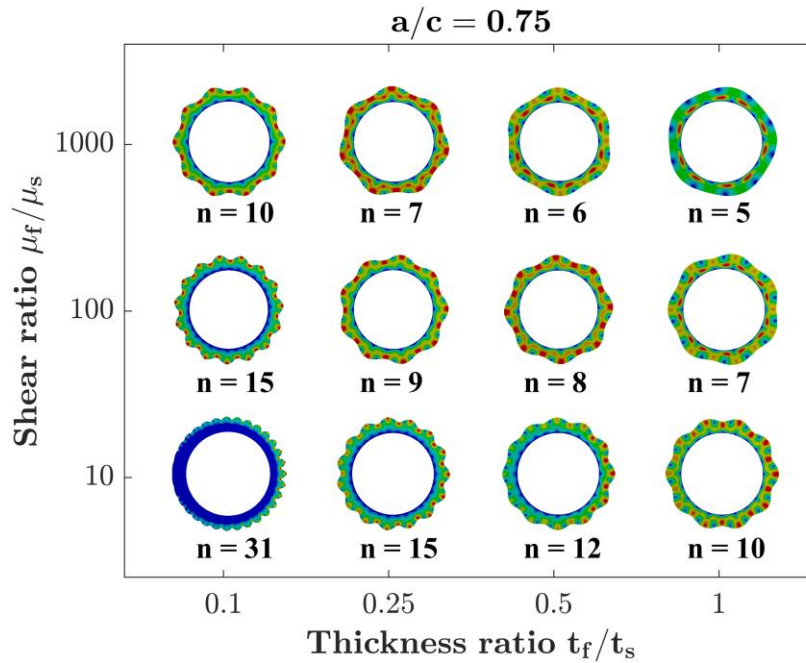
Figure 4-6. Critical surface wrinkle mode charts in terms of the wavenumber n and surface topology against the aspect ratio t_f/t_s and stiffness ratio μ_f/μ_s for $a/c = 0.75$.

Furthermore, comparison of Figures 4-4 to 4-6 shows that adoption of a hard core in co-electrospinning can significantly alter the surface wrinkling of the resulting electrospun fibers. At fixed t_f/t_s and μ_f/μ_s, i.e., the similar process parameters and polymer-solvent systems used in co-electrospinning, a large-sized hard core can trigger a larger wavenumber n, and the n-a/c correlation is roughly linear. This observation can be understood such that more surface wrinkles (with larger bending curvature and flexural energy) are needed to store the strain energy released from the compressed glassy shell upon surface wrinkling in the electrospun fibers with a large-sized hard core (i.e., with relatively thinner polymer layers). Thus, the surface wrinkle modes of electrospun fibers can be actively tuned via adjusting the size of the hard core in co-electrospinning.

Figures 4-7 to 4-15 further show the variation of the critical wrinkling compressive strain ε_c in the glassy shell with respect to the wavenumber n, i.e., the characteristic wrinkling ε_c-n diagram, at varying aspect ratios t_f/t_s and a/c and stiffness ratio μ_f/μ_s of the electrospun fibers with hard cores as shown in Figure 4-3. Figures 4-7 to 4-15 are extracted from the computational simulations for the surface wrinkle mode charts as shown in Figures 4-4 to 4-6. At fixed values of a/c (i.e., fixed size of the hard core) and μ_f/μ_s, Figures 4-7 to 4-15 indicate that ε_c in the glassy shell decrease rapidly with decreasing t_f/t_s, i.e., the thinner the glassy shell is (fast drying), the easier the surface wrinkling happens, which is correlated to the experimental observations (Koombhongse et al., 2001; Pai et al., 2009; Wang et al., 2009). In principle, the wrinkling of a thin elastic layer on a compliant substrate depends upon the flexural stiffness of the layer in term of $\sim t_f^3 \mu$; the cubic relation with respect to the layer thickness is roughly followed in Figures 4-7 to 4-15. In addition, for relatively thick glassy shells (e.g., $t_f/t_s = 0.25$,

50

0.5, and 1.0) of the electrospun fibers with a small-sized hard core ($a/c = 0.25$), ε_c increases nearly linearly with increasing wavenumber n; however, ε_c becomes insensitive to n for t_f/t_s = 0.1. In the case of the electrospun fibers with a large-sized core ($a/c = 0.75$), except for the case of t_f/t_s = 1.0, ε_c becomes insensitive to n for t_f/t_s = 0.1, 0.25 and 0.5. These observations show that fast drying (i.e., the thinner glassy shell or lower t_f/t_s) and large-sized hard core (i.e., larger a/c) typically result in a smaller ε_c, which is also insensitive to n, i.e., surface wrinkles corresponding to multiple values of n can coexist similar to multiple standing surface waves of varying wavelength/wavenumber. In addition, in the case of the electrospun fibers with a large-sized hard core (i.e., the large value of a/c), the characteristic wrinkling ε_c-n diagram behaves concave, implying that in the solvent evaporation process, the wavenumber n has the behavior of bifurcation with respect to ε_c. This bifurcation behavior can be understood such that with fast solvent evaporation from the jet, the compressive residual strain ε_r in the glassy shell grows and then exceeds the minimum ε_c, which may potentially trigger the surface wrinkling of two types of wrinkle mode. In addition, ε_c of electrospun fibers with a small-sized hard core (i.e., a small value of a/c) behaves more sensitive to μ_f/μ_s than that of electrospun fibers with a large-sized hard core. As a conclusion, the ε_c-n curves of electrospun fibers at varying a/c, t_f/t_s and μ_f/μ_s provide a complete scenario of the dependencies of surface wrinkle modes upon the process and material parameters adopted in co-electrospinning, which can be considered as the guidelines for surface wrinkling control and optimization. Furthermore, in the present computational study, the actual inhomogeneous fiber cross-section is modeled as two-layered coaxial structure with varying thickness ratio and stiffness ratio to

approach the stiffness gradient in the realistic fiber cross-section. In such a simplification scheme, the stiffness of the two-layered coaxial structure of the fiber is understood as a rational phenomenological approach to the effective stiffness of the inhomogeneous portion of the fiber cross-section, which would not result in noticeable errors in modeling.
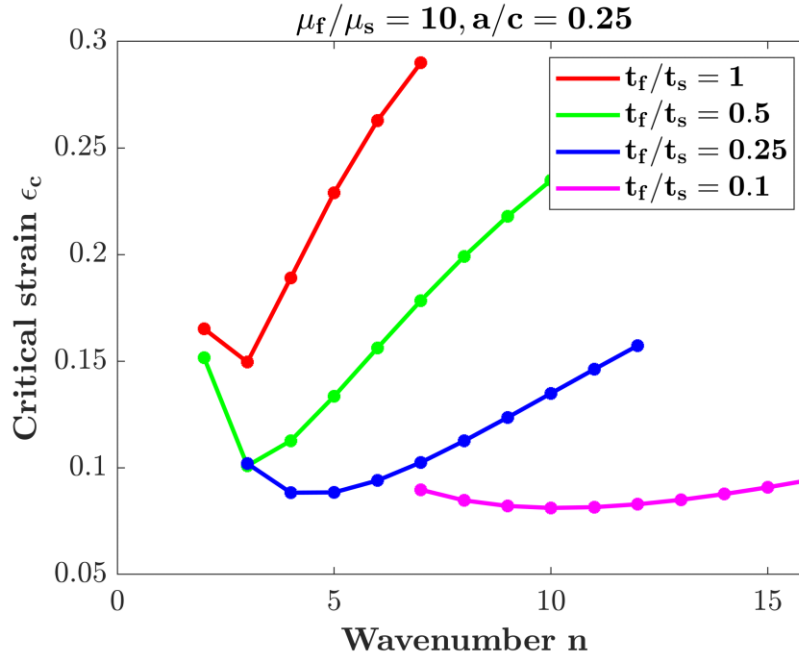
Figure 4-7. Variation of the critical wrinkling strain ε_c with respect to the wavenumber n of the surface wrinkle modes at varying aspect ratios t_f/t_s for $a/c = 0.25$ and $\mu_f/\mu_s = 10$.
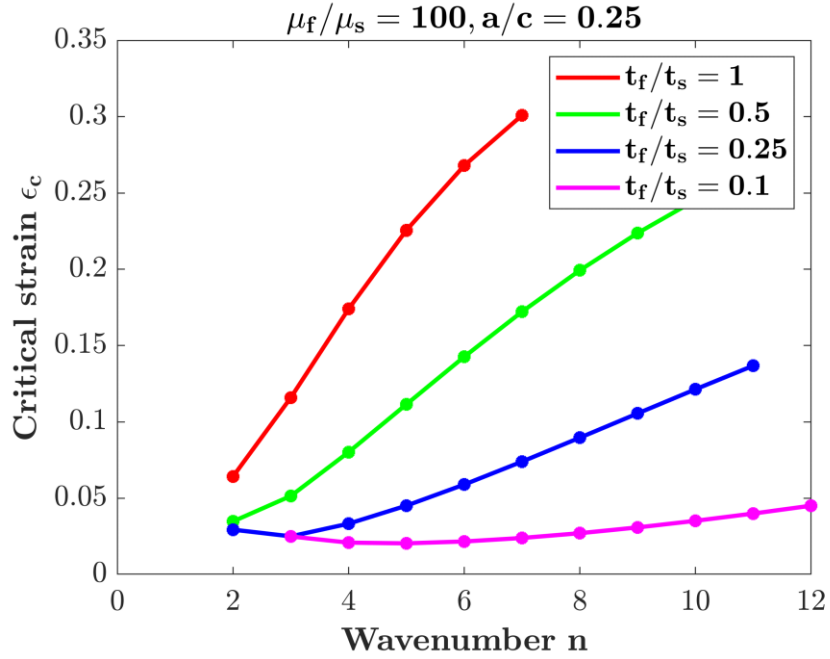
Figure 4-8. Variation of the critical wrinkling strain ε_c with respect to the wavenumber n of the surface wrinkle modes at varying aspect ratios t_f/t_s for $a/c = 0.25$ and $\mu_f/\mu_s = 100$.
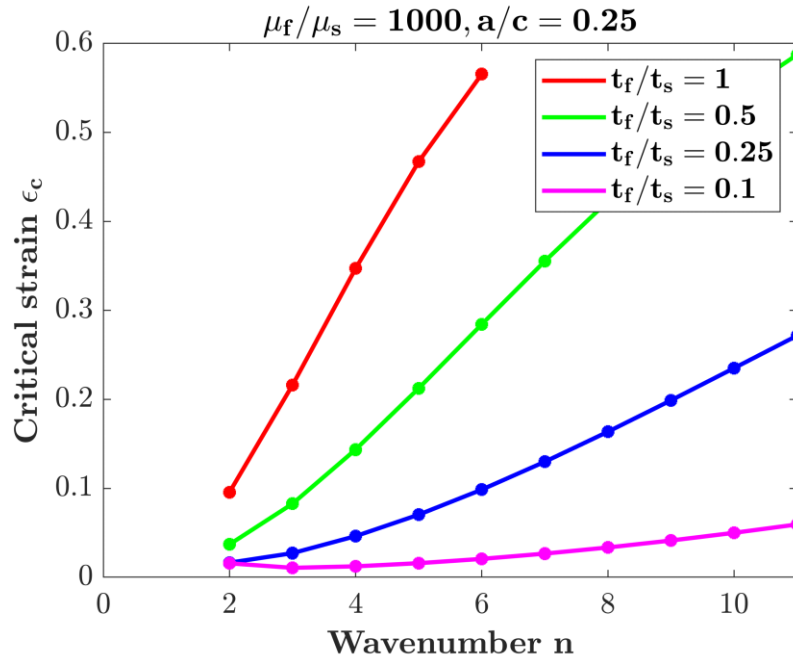
Figure 4-9. Variation of the critical wrinkling strain ε_c with respect to the wavenumber n of the surface wrinkle modes at varying aspect ratios t_f/t_s for $a/c = 0.25$ and $\mu_f/\mu_s = 1,000$.
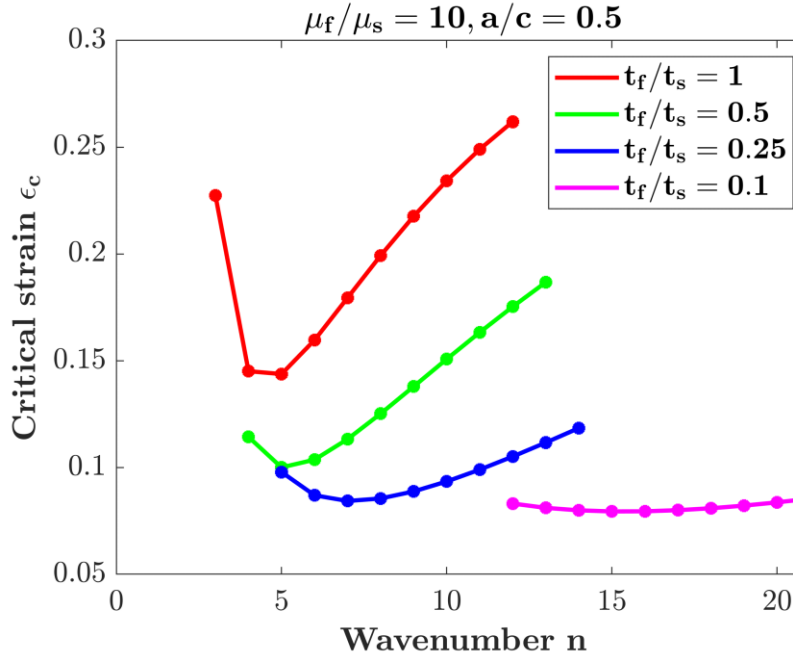
Figure 4-10. Variation of the critical wrinkling strain ε_c with respect to the wavenumber n of the surface wrinkle modes at varying aspect ratios t_f/t_s for $a/c = 0.5$ and $\mu_f/\mu_s = 10$.
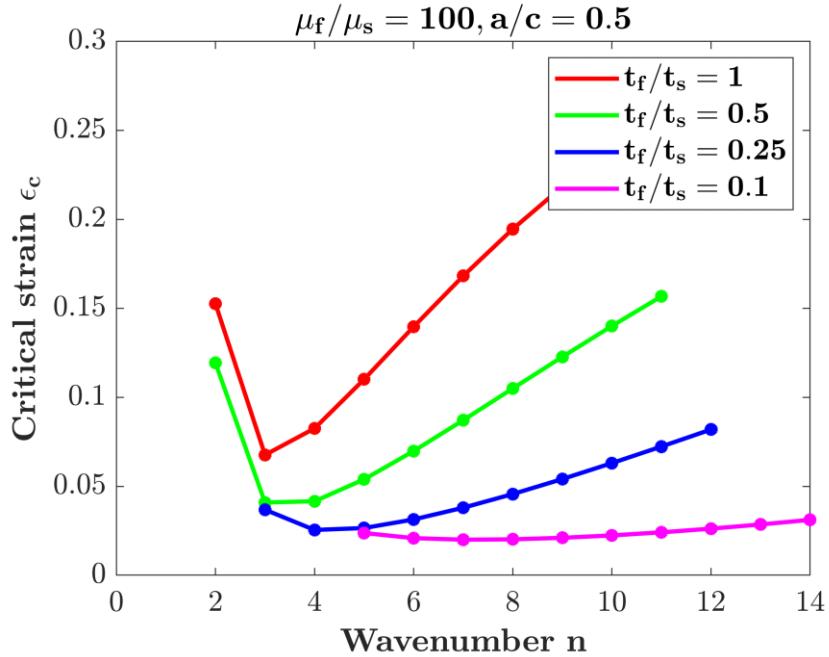
Figure 4-11. Variation of the critical wrinkling strain ε_c with respect to the wavenumber n of the surface wrinkle modes at varying aspect ratios t_f/t_s for $a/c = 0.5$ and $\mu_f/\mu_s = 100$.

54
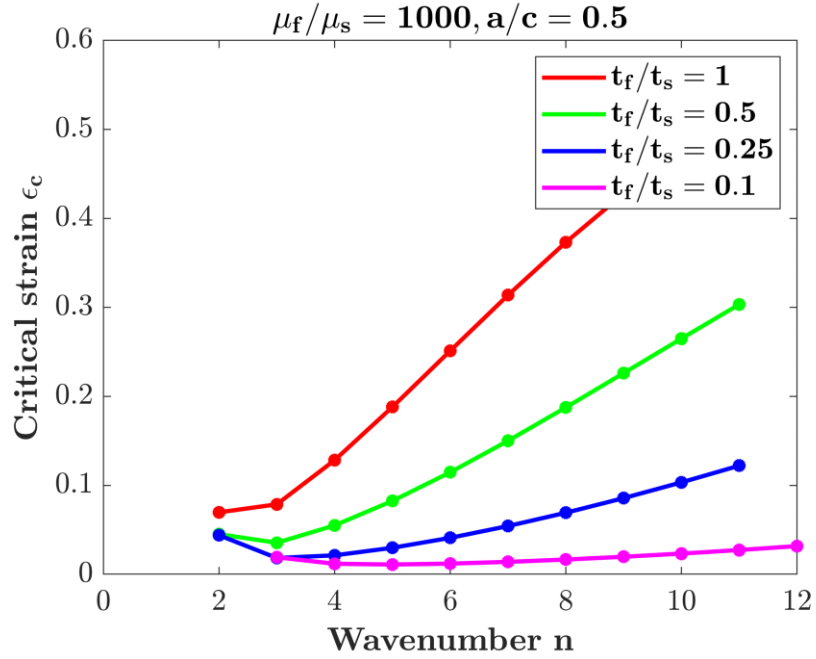
Figure 4-12. Variation of the critical wrinkling strain ε_c with respect to the wavenumber n of the surface wrinkle modes at varying aspect ratios t_f/t_s for $a/c = 0.5$ and $\mu_f/\mu_s = 1{,}000$.
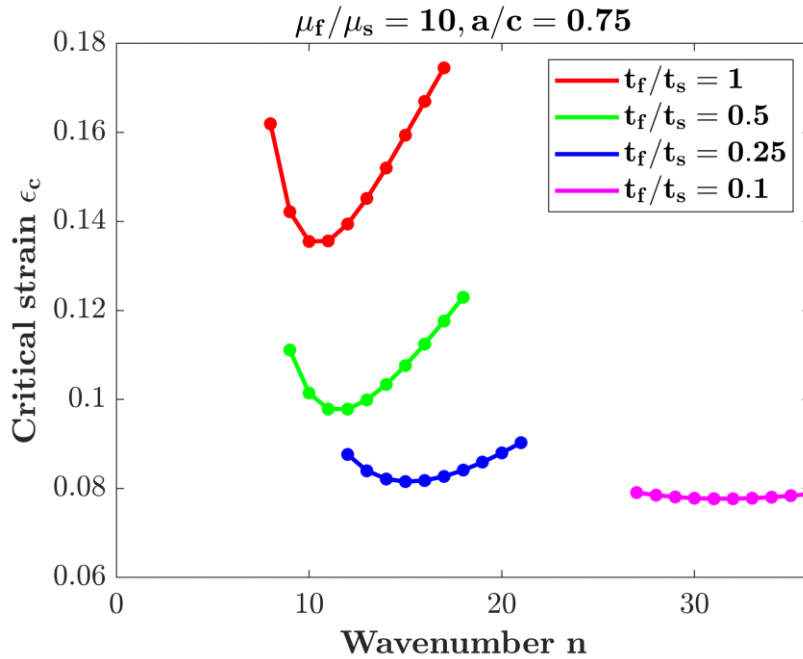
Figure 4-13. Variation of the critical wrinkling strain ε_c with respect to the wavenumber n of the surface wrinkle modes at varying aspect ratios t_f/t_s for $a/c = 0.75$ and $\mu_f/\mu_s = 10$.

55
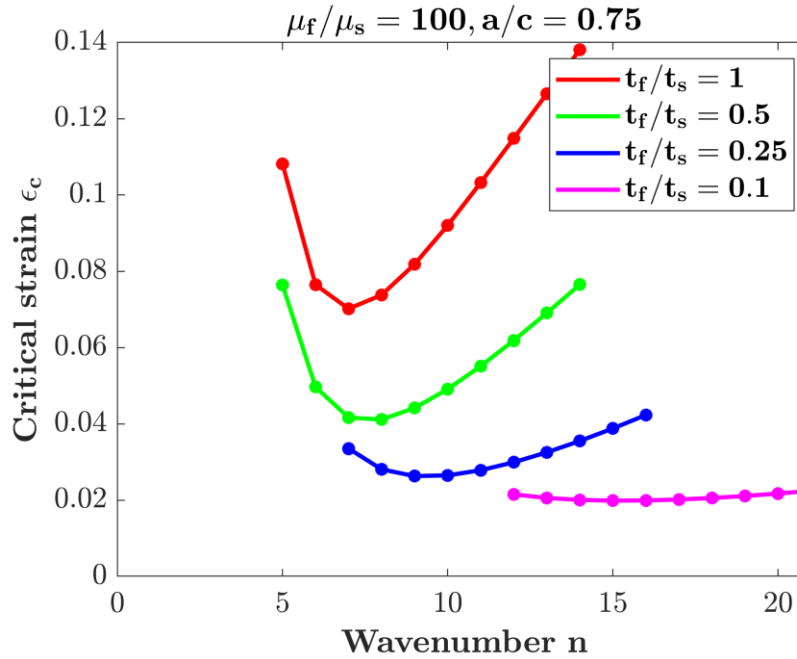
Figure 4-14. Variation of the critical wrinkling strain ε_c with respect to the wavenumber n of the surface wrinkle modes at varying aspect ratios t_f/t_s for $a/c = 0.75$ and $\mu_f/\mu_s = 100$.
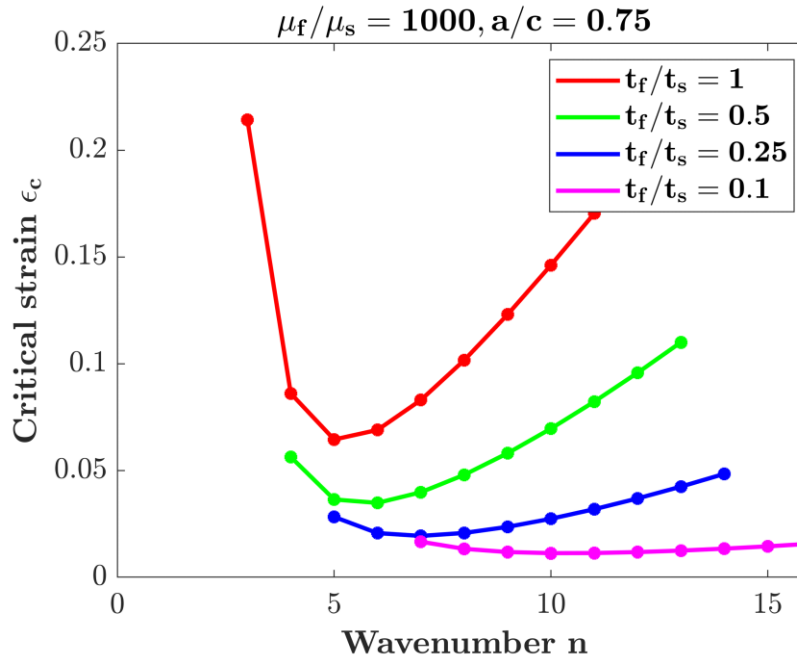
Figure 4-15. Variation of the critical wrinkling strain ε_c with respect to the wavenumber n of the surface wrinkle modes at varying aspect ratios t_f/t_s for $a/c = 0.75$ and $\mu_f/\mu_s = 1,000$.

Consequently, it needs to be mentioned that the typical diameters of electrospun fibers are in the range of a few nanometers to micrometers. Within such small scales, surface tension/energy of compliant electrospun fibers may influence their mechanical behavior (Wu et al., 2008; Wu, 2010; Wu & Dzenis, 2006, 2007a, 2007b, 2007c; Wu et al., 2010) and related critical wrinkling strain ε_c and surface wrinkle modes (the wavenumber n). As surface effects (e.g., surface tension/energy, etc.) are excluded in the present study due to the limitation of the commercial FEA software ANSYS®, the present computational scaling analysis indicates that the wrinkled surface topologies (i.e., the wavenumber n) only depends upon the aspect ratios (a/c and t_f/t_s) and stiffness ratio (μ_f/μ_s) while explicitly independent of the fiber radius c, i.e., the surface wrinkling phenomenon within the present continuum mechanics framework is size-independent. Therefore, all the numerical results gained above and conclusions drawn in this study are applicable to surface wrinkling analysis of all types of compliant fibers and cylinders with hard cores.

4.3. Concluding Remarks

Wrinkle modes of ultrathin polymer fibers produced in the electrospinning process can be intelligently regulated via incorporating hard cores of different size into the fibers. The dependencies of surface wrinkle modes of these core-shell polymer fibers enwrapped with hard cores upon the thickness and stiffness ratios of the glassy shell and inner soft sol-gel layers have been obtained via detailed computational buckling analysis, which provides a rational basis of producing ultrathin polymer micro/nanofibers with controllable surface morphologies. Such electrospun nanofibers carry greatly enhanced specific surface areas suitable for various

advanced applications such as oil-water separation, high-graded gas and liquid filtration, drug delivery, catalyst carriers, tissue scaffolding, etc.

CHAPTER 5. INHOMOGENEOUS SWELLING BEHAVIOR OF A BI-LAYERED SPHERICAL HYDROGEL CONTAINING A HARD CORE

5.1. Introduction

Hydrogels swell significantly when imbibing water and exhibit inhomogeneous deformation, stress, and water concentration fields when the swelling is constrained. This chapter studies the displacement, stress, and water concentration fields of a bi-layered spherical hydrogel bonded onto a hard core, which is an extension of the problem considered by Zhao et al. (2008a). Experimentally, it is convenient to coat a 2nd gel layer onto the 1st one to form a bi-layered hydrogel or a composite hydrogel layer. To do so, the 2nd layer can be used to regulate the swelling behavior of the entire hydrogel system. In practice, it is favorable to apply a relatively stiff surface gel layer to protect the inner hydrogel layer such as the generation of compressive radial stress to stabilize the core-shell structure and suppression of the wear and tear of the inner softer hydrogel layer. The present problem is reduced into a two-point boundary value problem of a 2nd-order ODE with inner continuity conditions between two neighboring layers and solved numerically. Effects of the outer layer stiffness on the displacement, stress, and water concentration fields are examined and compared. Consequently, conclusions and recommendations of the present study are made.

5.2. Model Development

Figure 5-1 illustrates two concentric spherical hydrogels, designated as Layers I and II, which are bonded perfectly together onto a hard core. In the reference state, the hydrogels are treated as dry and stress-free as shown in Figure 5-1(a), with the configurations such that Layer I has the inner radius of A and outer radius of B, while Layer II carries the inner radius of B and

59

outer radius of C. In the equilibrium state of the hydrogels after imbibing water, the hydrogels were swollen into the current configuration with an inner radius of $A\lambda_0$ for the hard core and radii b and c corresponding to the initial radii B and C, respectively, as shown in Figure 5-1(b). Herein, the initial stretch λ_0 is due to the preparation method of the hard core inside the inner gel. In the special case of $\lambda_0 = 1$, it means that the hard core has no deformation after the hydrogel system imbibes water.

Dry polymers

Gels

Core

(a)   **(b)**
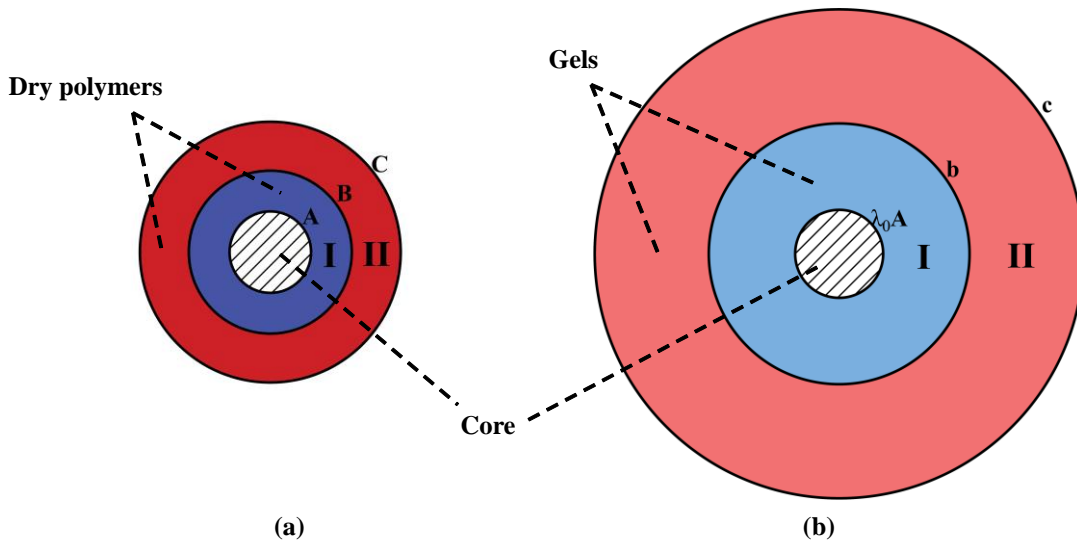
Figure 5-1. Two concentric spherical hydrogels layers bonded onto a hard core. Layers I and II carry different material properties. (a) Dry polymer networks, (b) Swollen hydrogels after imbibing water.

By submerging the hydrogel system into pure water, the hydrogel layers start to swell inhomogeneously and anisotropically till the water molecules inside the hydrogel polymer networks reach thermodynamic equilibrium with those out of the hydrogel in pure water. In this study, the hard core is assumed to be rigid and bonded perfectly to Layer I as shown in Figure 5-1(a), thus only the radial stretch of the network exists at the core-hydrogel interface. Correspondingly, the circumferential stretch of the network near the core-hydrogel interface is

dominated by the rigidity of the hard core instead of the swelling of the inner hydrogel. On the other hand, the hydrogel polymer networks out of the core-hydrogel interface can expand in all three directions. Thus, it is expected that a lower volume fraction of water appears near the core-hydrogel interface (Zhao et al., 2008a).

As shown in Figure 5-1, the radius of an arbitrary mass point in the initial dry hydrogels is denoted as R, which is ranging from A to B for Layer I and ranging from B to C for Layer II. In the equilibrium state of the hydrogels after imbibing water, the spherical symmetry of the problem expects that the swollen networks will sustain its spherical symmetry (Zhao et al., 2008a), and the radius of an arbitrary mass point in the swollen hydrogels can be denoted as $r(R)$, which varies from $\lambda_0 A$ to b for Layer I and from b to c for Layer II. Therefore, the radial stretch of the hydrogels is

$$\lambda_r = \frac{dr}{dR},$$

(5.1)

and the circumferential stretch is

$$\lambda_\theta = \frac{r}{R},$$

(5.2)

which lead to the deformation gradient as

$$\mathbf{F} = \begin{bmatrix} \dfrac{\partial r}{\partial R} & \dfrac{\partial r}{R\partial \Theta} & \dfrac{\partial r}{R\partial \Phi} \\ \dfrac{r\partial \theta}{\partial R} & \dfrac{r\partial \theta}{R\partial \Theta} & \dfrac{r\partial \theta}{R\partial \Phi} \\ \dfrac{r\partial \phi}{\partial R} & \dfrac{r\partial \phi}{R\partial \Theta} & \dfrac{r\partial \phi}{R\partial \Phi} \end{bmatrix} = \begin{bmatrix} \lambda_r & 0 & 0 \\ 0 & \lambda_\theta & 0 \\ 0 & 0 & \lambda_\theta \end{bmatrix},$$

(5.3)

and the corresponding left Cauchy-Green tensor and its three principal scalar invariants as

$$\mathbf{B} = \mathbf{F}\mathbf{F}^T = \begin{bmatrix} \lambda_r^2 & 0 & 0 \\ 0 & \lambda_\theta^2 & 0 \\ 0 & 0 & \lambda_\theta^2 \end{bmatrix}, \tag{5.4}$$

$$I_1 = \lambda_r^2 + 2\lambda_\theta^2, \qquad I_2 = 2\lambda_r^2\lambda_\theta^2 + \lambda_\theta^4, \qquad I_3 = \lambda_r^2\lambda_\theta^4. \tag{5.5}$$

Imbibing water molecules causes the volume change of the hydrogels. Assume that the individual water molecules and the individual long polymers of the hydrogels are incompressible. Thus, the molecular incompressibility condition of the hydrogels follows (Hong et al. 2008b; Zhao et al., 2008a)

$$\det(\mathbf{F}) = 1 + vC, \tag{5.6}$$

which can be recast as

$$vC = \lambda_\theta^2\lambda_r - 1. \tag{5.7}$$

In above, v is the volume per water molecules and C is the water concentration in a hydrogel, that is the number of water molecules in an element of the hydrogel in the equilibrium state divided by the volume of the dry hydrogel polymer in the reference configuration (Hong et al. 2008b; Zhao et al., 2008a).

Once the swollen hydrogel reaches the equilibrium state after imbibing water, it develops a stress field according to the work by Gibbs (1906) who derived the state equations from a free-energy density, $W(\mathbf{F}, C)$, which is a function with respect to the deformation gradient $\mathbf{F}$ and water concentration C (Hong et al., 2009; Zhao et al., 2008a). Correspondingly, the Cauchy stress components, s_r and s_θ, and chemical potential μ in the current configuration of the hydrogels can be expressed as.

$$s_r = \frac{\partial W(\mathbf{F}, C)}{\partial \lambda_r}, \tag{5.8}$$

$$s_\theta = \frac{\partial W(\mathbf{F}, C)}{\partial \lambda_\theta}, \tag{5.9}$$

$$\mu = \frac{\partial W(\mathbf{F}, C)}{\partial C}, \tag{5.10}$$

where $s_r(R)$ is the nominal radial stress, $s_\theta(R)$ is the nominal circumferential stress, and μ is the chemical potential of the solvent molecules. The stress equilibrium equation in the spherical coordinate system can be expressed as

$$\frac{ds_r}{dR} + 2\frac{s_r - s_\theta}{R} = 0. \tag{5.11}$$

The condition of molecular incompressibility can be added to the free-energy density of the hydrogel as a constraint in terms of $W(\mathbf{F}, C) + \Pi(1 + vC - \det(\mathbf{F}))$, where Π is a Lagrange multiplier (Zhao et al., 2008b; Nayak & Lyon, 2005). Thus, the formal expressions for nominal stresses (5.8) and (5.9) and chemical potential (5.10) are

$$s_r = \frac{\partial W(\mathbf{F}, C)}{\partial \lambda_r} - \Pi \frac{\partial \det(\mathbf{F})}{\partial \lambda_r}, \tag{5.12}$$

$$s_\theta = \frac{\partial W(\mathbf{F}, C)}{\partial \lambda_\theta} - \Pi \frac{\partial \det(\mathbf{F})}{\partial \lambda_\theta}, \tag{5.13}$$

$$\mu = \frac{\partial W(\mathbf{F}, C)}{\partial C} + \Pi v. \tag{5.14}$$

Due to the geometrical constraint of the inner hard core, the hydrogels are inhomogeneous and anisotropic at their equilibrium state after imbibing water. This equilibrium state can be determined via solving (5.11) as a mixed boundary value problem once the free-energy function is available (Hong et al., 2008b). Among others, one commonly used free-energy density function for a swollen elastomer developed by Flory and Rehner (1943) with the notation by Hong et al. (2008b) can be adopted for such purpose,

63

$$W(\mathbf{F},C) = \frac{1}{2}NkT\left[I_1 - 3 - 2\log\left(\det(\mathbf{F})\right)\right] - \frac{kT}{v}\left[vC\log\left(1 + \frac{1}{vC}\right) + \frac{\chi}{1+vC}\right], \qquad (5.15)$$

where N is the number of polymer chains in the hydrogel divided by the volume of the dry

polymer networks, kT is the temperature in the unit of energy, and χ is a dimensionless

parameter from the enthalpy of mixing (Flory & Rehner, 1943; Hong et al., 2008b).

In this study, the solvent is considered as pure water, and its chemical potential μ is set

to be zero. Substitution of (5.15) into (5.12) and (5.14) with $\mu = 0$ leads to the state equations

(Hong et al., 2008b):

$$\frac{s_r}{NkT} = \lambda_r - \lambda_r^{-1} + \frac{\lambda_\theta^2}{vN}\left[\log\frac{vC}{1+vC} + \frac{1}{1+vC} + \frac{\chi}{(1+vC)^2}\right], \qquad (5.16)$$

$$\frac{s_\theta}{NkT} = \lambda_\theta - \lambda_\theta^{-1} + \frac{\lambda_\theta\lambda_r}{vN}\left[\log\frac{vC}{1+vC} + \frac{1}{1+vC} + \frac{\chi}{(1+vC)^2}\right]. \qquad (5.17)$$

According to Zhao et al. (2008a), in the absence of external mechanical constraints, the

polymer network swells freely and ends up with a homogeneous and isotropic expansion to reach

its equilibrium state. The equilibrium water concentration vC_{free} in a free-swelling hydrogel can

be determined by solving a nonlinear algebraic equation numerically after setting

$\lambda_r = \lambda_\theta = \lambda_{\text{free}} = (vC_{\text{free}} + 1)^{1/3}$ and $s_r = 0$ in (5.16) as

$$(vC_{\text{free}} + 1)^{1/3} - \frac{1}{(vC_{\text{free}} + 1)^{1/3}} + \frac{(vC_{\text{free}} + 1)^{2/3}}{vN}\left[\log\frac{vC_{\text{free}}}{1+vC_{\text{free}}} + \frac{1}{1+vC_{\text{free}}} + \frac{\chi}{(1+vC_{\text{free}})^2}\right] = 0. \quad (5.18)$$

For a constrained hydrogel network, the governing equation of swollen hydrogels can be

derived by substituting (5.16) and (5.17) into (5.11) and considering (5.1), (5.2), and (5.7) to

form a nonlinear 2$^{\text{nd}}$-order ODE:

$$\frac{d^2r}{dR^2} - \frac{d}{dR}\left(\frac{dR}{dr}\right) + \frac{1}{vN}\frac{d}{dR}\left\{\frac{r^2}{R^2}\left[\log\left(1 - \frac{R^2}{r^2}\frac{dR}{dr}\right) + \frac{R^2}{r^2}\frac{dR}{dr} + \chi\left(\frac{R^2}{r^2}\frac{dR}{dr}\right)^2\right]\right\} +$$

$$\frac{2}{R}\left\{\frac{dr}{dR} - \frac{dR}{dr} - \frac{r}{R} + \frac{R}{r} + \frac{1}{vN}\left(\frac{r^2}{R^2} - \frac{r}{R}\frac{dr}{dR}\right)\left[\log\left(1 - \frac{R^2}{r^2}\frac{dR}{dr}\right) + \frac{R^2}{r^2}\frac{dR}{dr} + \chi\left(\frac{R^2}{r^2}\frac{dR}{dr}\right)^2\right]\right\} = 0 . \quad (5.19)$$

In this study, a hard core and two layers of concentric hydrogels are assumed to be bonded together perfectly. In this case, Eq. (5.19) can be solved numerically with the BCs: $r(A)$ $= \lambda_0 A$ and $s_r(C) = 0$ as well as the interface continuity conditions, i.e., $r(R)$ and $s_r(R)$ as continuous functions across at the hydrogel-hydrogel interface at $R = B$ such that $r(R^{-0}) = r(R^{+0})$ and $s_r(R^{-0}) = s_r(R^{+0})$.

5.3. Numerical Examples and Discussions

5.3.1. The Equilibrium State of Two Bonded Swollen Hydrogels Containing a Hard Core

In the numerical analysis of the equilibrium state of the two bonded spherical swollen hydrogels layers as shown in Figure 5-1, the initial stretch of the hard core is assumed as $\lambda_0 = 1.077$, the dimensionless parameters vN and χ are considered in the range of $10^{-5} - 10^{-1}$ and $0 - 1.2$, respectively (Hong et al., 2009; Zhao et al., 2008a).

Figures 5-2 to 5-5 show the displacement, water concentration, stretch, and stress fields of the hydrogel system in equilibrium state after imbibing sufficient water, in which the two hydrogel layers are assumed to carry different stiffness. Herein the lines in green represent the results of the case where both the hydrogel layers in the system carry identical properties (i.e., $vN = 10^{-3}$ and $\chi = 0.2$), i.e., the case of a single hydrogel layer that has been considered and

65

validated by Zhao et al. (2008a). Thus, the present swelling mechanics model of hydrogels can cover those available in the literature in the limiting case of a single hydrogel layer.

In addition, if taking the lines in green as the reference, two other cases (lines in red and blue) are further considered, of which one layer (the inner or outer) is set to be softer with $vN = 10^{-4}$ and $\chi = 0.1$, in an alternative. Figure 5-3 shows that in either case, the softer hydrogel layer tends to imbibe more water and results in a higher water concentration compared to that of the reference case. Though the softer layer is constrained by the hard core and the outer layer, it can still swell significantly and pushes out the outer hydrogel layer. Figure 5-4 stands for the variations of radial and circumferential stretches with respect to the dimensionless radius R/A. It can be observed that the stretches of the inner layer for both the cases (lines in red and blue) are close to those of the reference case, while the stretches of the outer layer show a large deviation as the one with a softer outer hydrogel is experiencing larger stretches in the outer layer compared to the reference case and the case of the system with a softer inner hydrogel. Figure 5-5 shows the variations of radial and circumferential stresses with respect to the dimensionless radius R/A. Lines in blue show that when the outer layer is softer, the entire system would experience tensile radial stress; lines in red show that when the inner layer is softer, the radial stress at the interface between two hydrogel layers is compressive. In Figure 5-5, all the dimensionless stresses are measured on the basis of the shear modulus of the dry polymer network NkT (Hong et al., 2009; Zhao et al., 2008a).

Figure 5-2. Variation of the dimensionless radial deformation with respect to the dimensionless dry hydrogel radius in an equilibrium state of two spherical hydrogel layers (with one layer softer than the reference hydrogel) bonded onto a hard core.

Figure 5-3. Variation of the water concentration with respect to the dimensionless dry hydrogel radius in an equilibrium state of two spherical hydrogel layers (with one layer softer than the reference hydrogel) bonded onto a hard core.

Figure 5-4. Variation of the principle stretches with respect to the dimensionless dry hydrogel radius in an equilibrium state of two spherical hydrogel layers (with one layer softer than the reference hydrogel) bonded onto a hard core.

Figure 5-5. Variation of the principle nominal stresses with respect to the dimensionless dry hydrogel radius in an equilibrium state of two spherical hydrogel layers (with one layer softer than the reference hydrogel) bonded onto a hard core.

68

Figures 5-6 to 5-9 show the displacement, water concentration, stretch, and stress fields of the hydrogel system in the equilibrium state after imbibing sufficient water when one hydrogel layer is stiffer than the reference one. Similar to Figures 5-2 to 5-5, lines in green are the results of the reference case for the purpose of comparison, while lines in red and blue show the results of two cases, of which one of the hydrogel layers (either the inner or outer) is set to be stiffer with $vN = 10^{-2}$ and $\chi = 0.4$, alternatively. Figure 5-7 shows that the stiffer hydrogel layer tends to imbibe much less water than that of the reference case. Though the stiffer hydrogel layer is swollen while it constrains the swelling of the softer hydrogel layer. Figure 5-8 represents the variations of radial and circumferential stretches with respect to the dimensionless radius R/A. It can be found that the stretches in the inner hydrogel layer in both the cases (lines in red and blue) are close to each other. However, stretches in the outer hydrogel layer exhibit a noticeable difference such that the stiffer outer hydrogel layer experiences lower stretches than either the reference case or the case with a stiffer inner hydrogel. Figure 5-9 shows the variations of radial and circumferential stresses with respect to the dimensionless radius R/A. Herein lines in blue show that in the case of the system with a stiffer outer hydrogel layer, the radial stress at the interface is compressive. In contrast, in the case of the system with a stiffer inner hydrogel layer, lines in red show that the entire system experiences tensile radial stress.
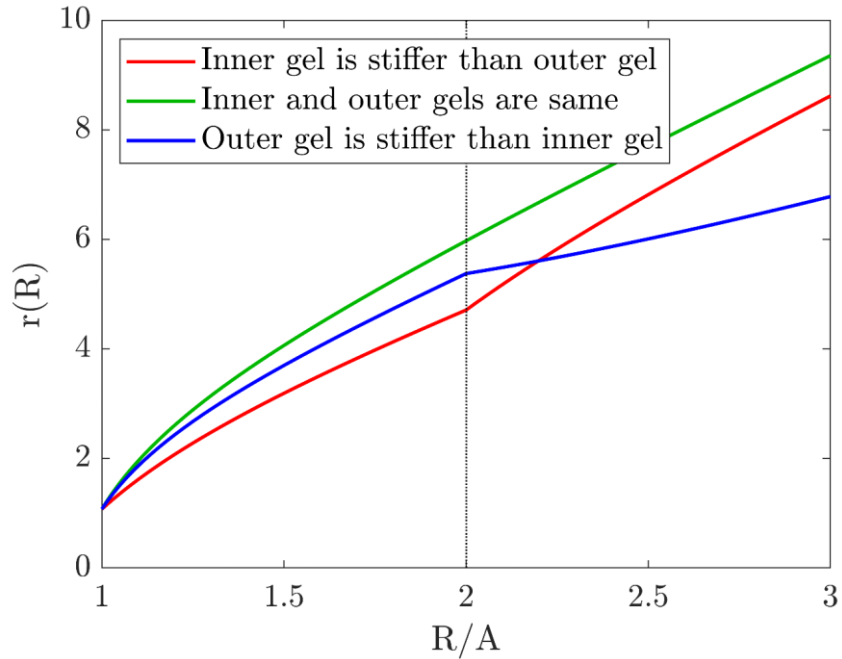
Figure 5-6. Variation of the dimensionless radial deformation with respect to the dimensionless dry hydrogel radius in an equilibrium state of two spherical hydrogel layers (with one layer stiffer than the reference hydrogel) bonded onto a hard core.
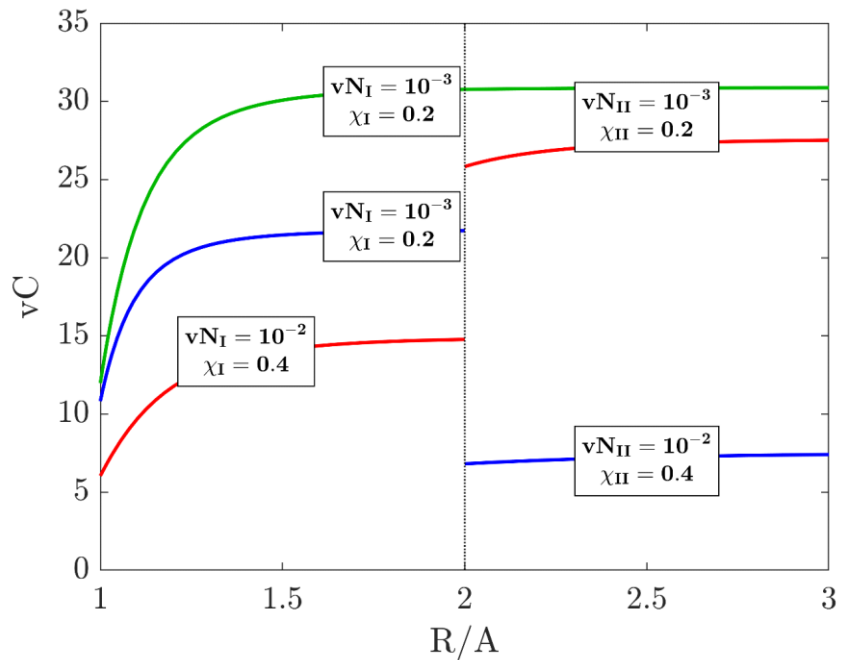
Figure 5-7. Variation of the water concentration with respect to the dimensionless dry hydrogel radius in an equilibrium state of two spherical hydrogel layers (with one layer stiffer than the reference hydrogel) bonded onto a hard core.
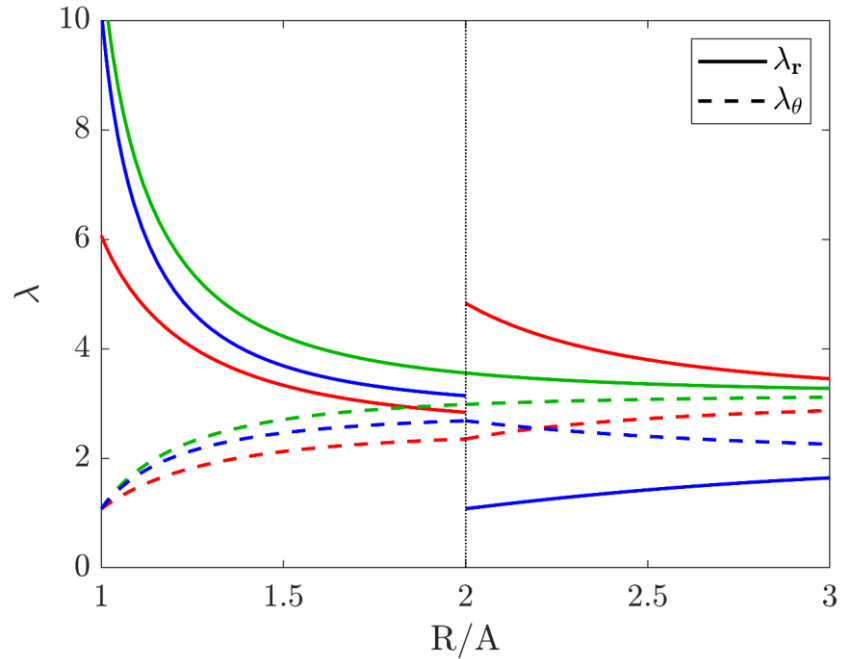
Figure 5-8. Variation of the principle stretches with respect to the dimensionless dry hydrogel radius in an equilibrium state of two spherical hydrogel layers (with one layer stiffer than the reference hydrogel) bonded onto a hard core.
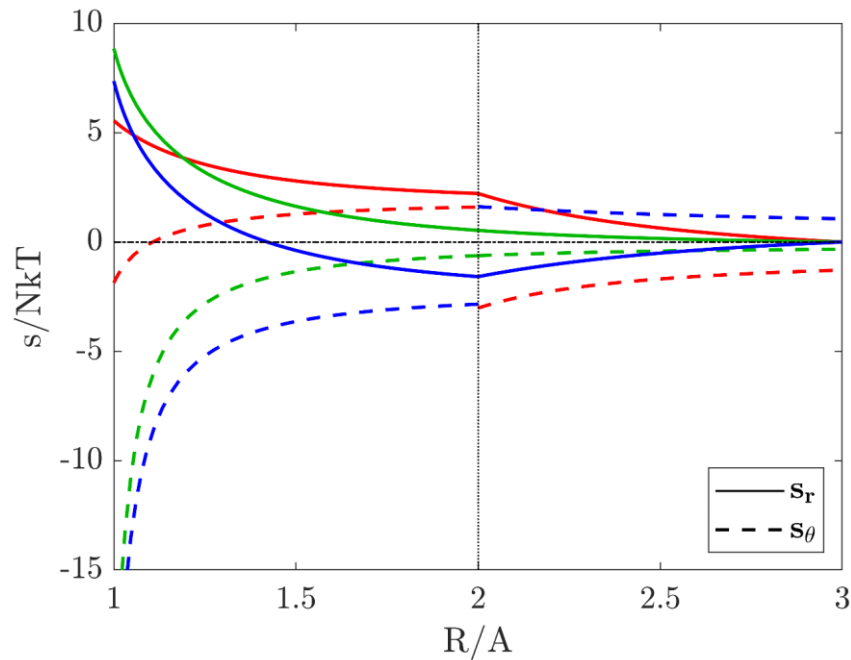
Figure 5-9. Variation of the principle nominal stresses with respect to the dimensionless dry hydrogel radius in an equilibrium state of two spherical hydrogel layers (with one layer stiffer than the reference hydrogel) bonded onto a hard core.

5.3.2. The Equilibrium State of a Soft Hydrogel Enclosed by an Extremely Stiff Gel

In this case study, the outer layer of the bi-layered hydrogel system is assumed extremely stiff with parameters vN and χ to take very large values that can be physically realized via increasing the network density and hydrophobic behavior of the polymer networks. Herein, the inner soft hydrogel is treated to be bonded perfectly onto a hard core with $\lambda_0 = 1.077$.

Figures 5-10 to 5-13 show the displacement, water concentration, stretch, and stress fields in the equilibrium state of a soft hydrogel enclosed by an extremely stiff hydrogel bonded perfectly onto a hard core as aforementioned. Herein, lines in blue show the results of the reference case for the purpose of comparison ($vN = 10^{-4}$ and $\chi = 0.1$); lines in red indicate the results of the system with an inner soft hydrogel layer with $vN = 10^{-4}$ and $\chi = 0.1$ and the outer stiff hydrogel layer with $vN = 10^{-1}$ and $\chi = 1.2$. Figure 5-11 shows that the outer stiff hydrogel layer does not imbibe noticeable water and the water concentration is nearly zero, i.e., the outer hydrogel layer does not swell. From Figure 5-12, it can be noticed that the radial stretch λ_r of the stiff outer hydrogel layer is below 1, i.e., in radial compression. As λ_{free} of the outer stiff hydrogel layer is close to 1, increasing the outer layer thickness (radius) will not noticeably alter the deformation of the outer layer. Figure 5-13 shows the variations of stresses (s_r and s_θ) with respect to the dimensionless dry hydrogel radius R/A. It can be found that in this case, the inner hydrogel layer is under high tensile radial stress s_r at the core-gel interface that may induce the debonding of the hydrogel layer from the hard core (Crassous et al., 2006; Ballauff & Lu, 2007). With increasing the radius from the core-hydrogel interface, the tensile radial stress s_r diminishes till it becomes compressive. At the gel-gel interface, the radial stress s_r reaches its

compressive peak value, and with further increasing the radius away from the gel-gel interface,

s_r tends to vanish at the outer rim.
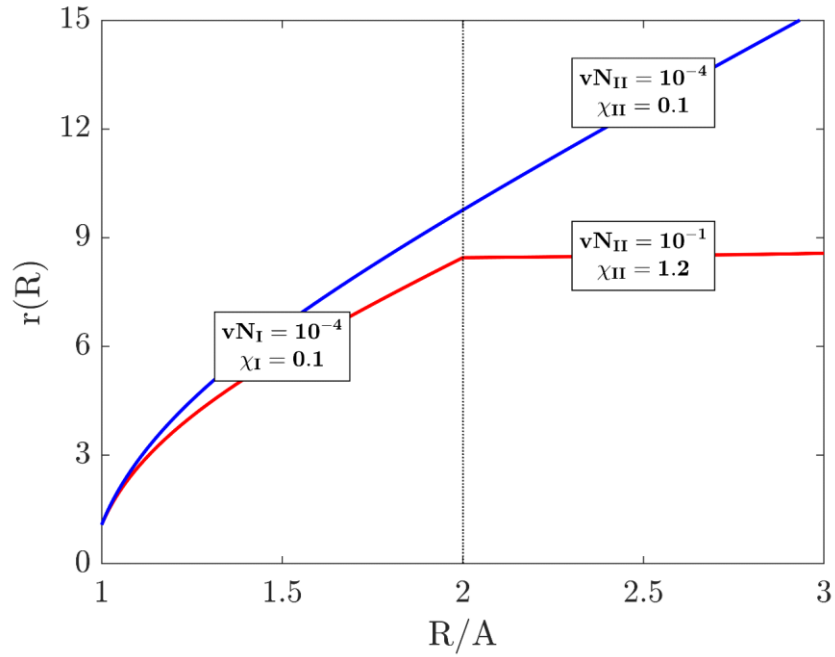
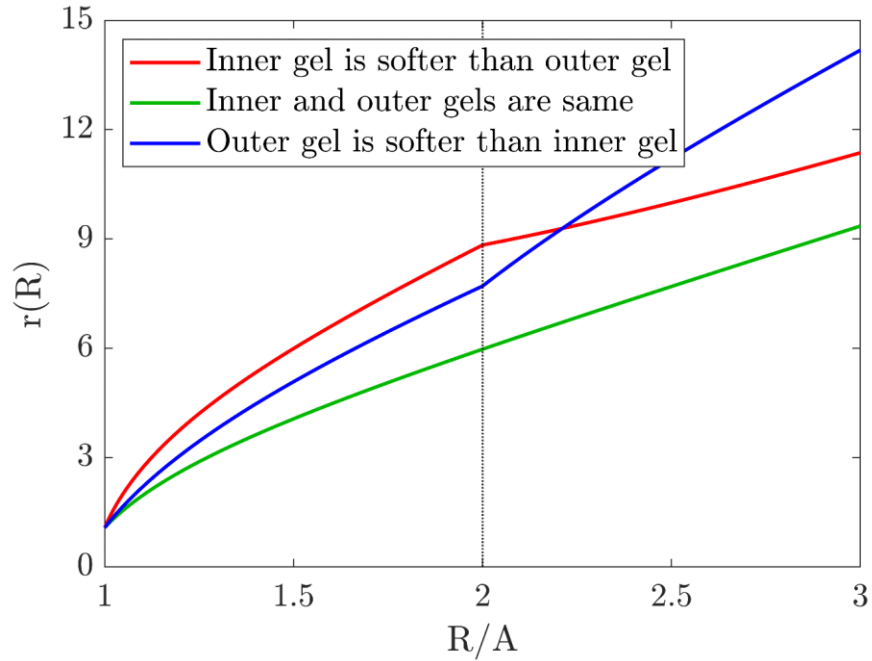Figure 5-10. Variation of the dimensionless radial deformation with respect to the dimensionless dry hydrogel radius in an equilibrium state of one soft spherical hydrogel layer enclosed by an extremely stiff hydrogel layer.
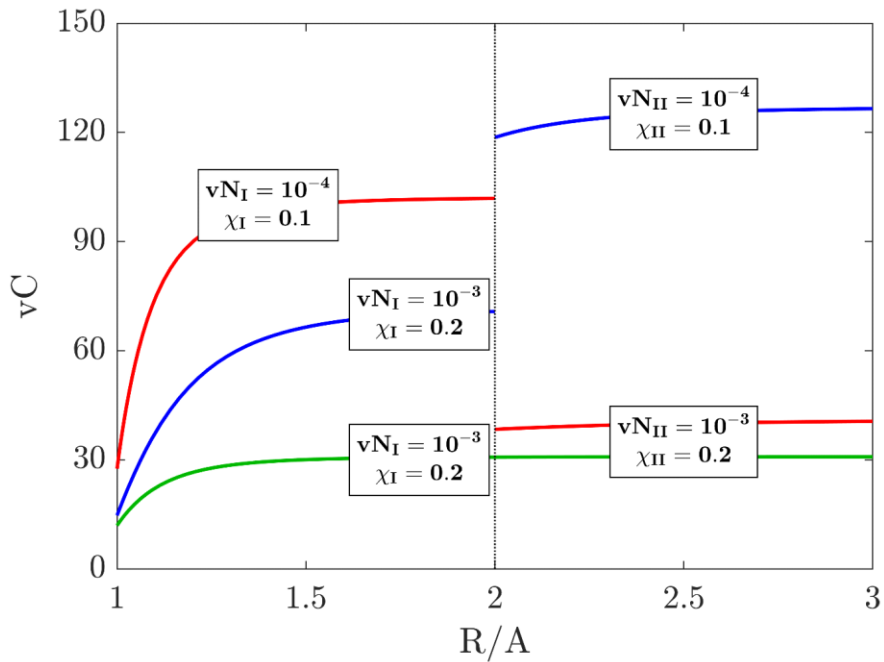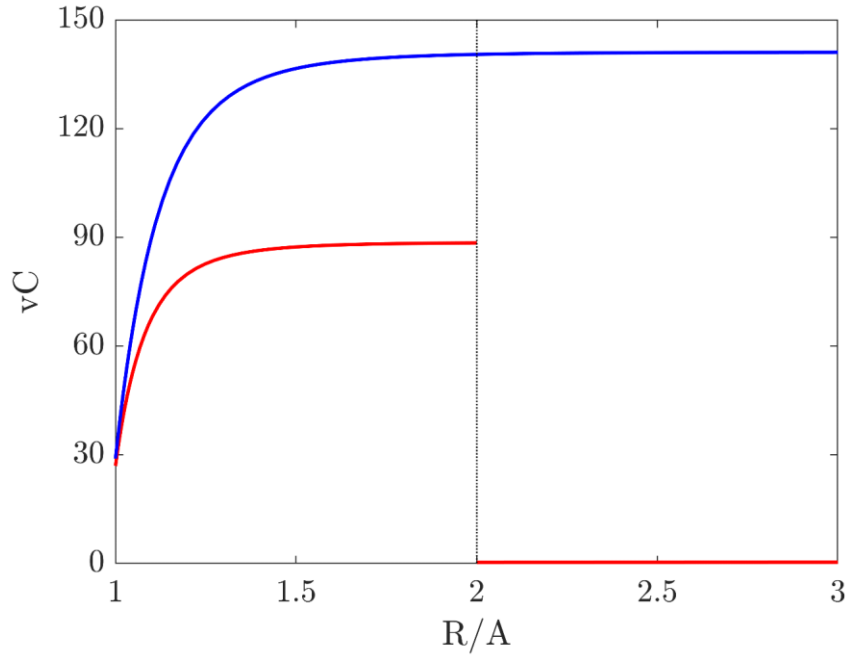
Figure 5-11. Variation of the water concentration with respect to the dimensionless dry hydrogel radius in an equilibrium state of one soft spherical hydrogel layer enclosed by an extremely stiff hydrogel layer.
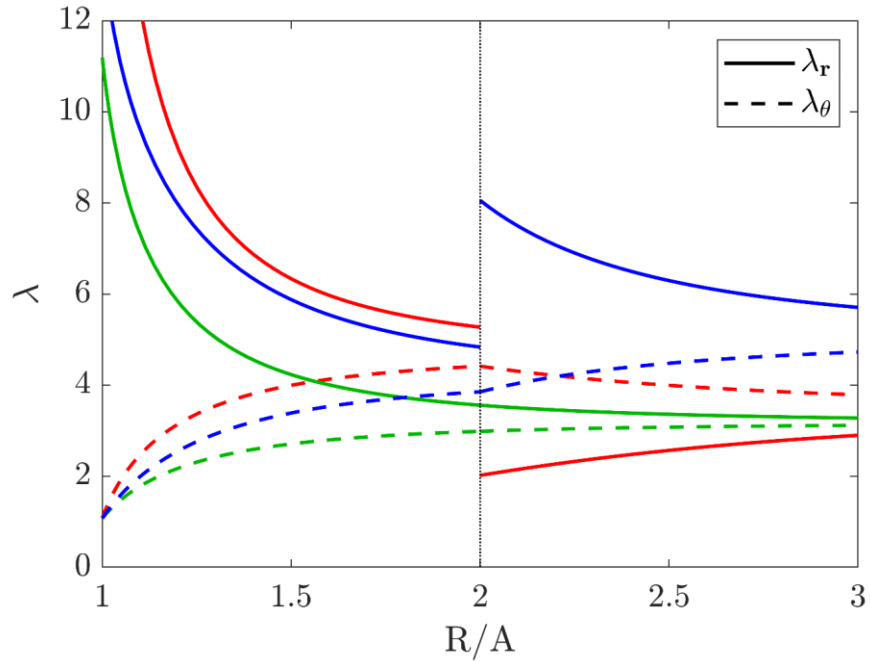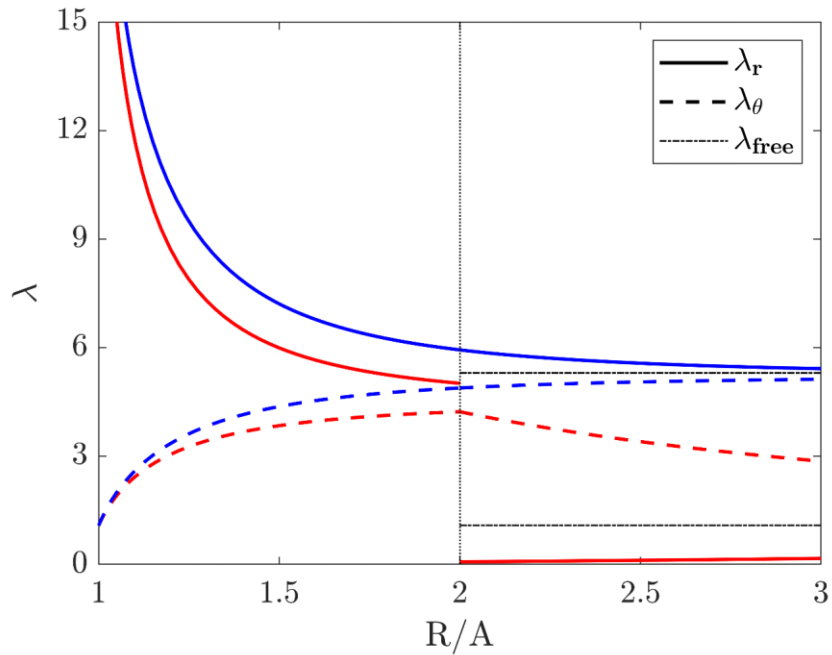

Figure 5-12. Variation of the principle stretches with respect to the dimensionless dry hydrogel radius in an equilibrium state of one soft spherical hydrogel layer enclosed by an extremely stiff hydrogel layer.
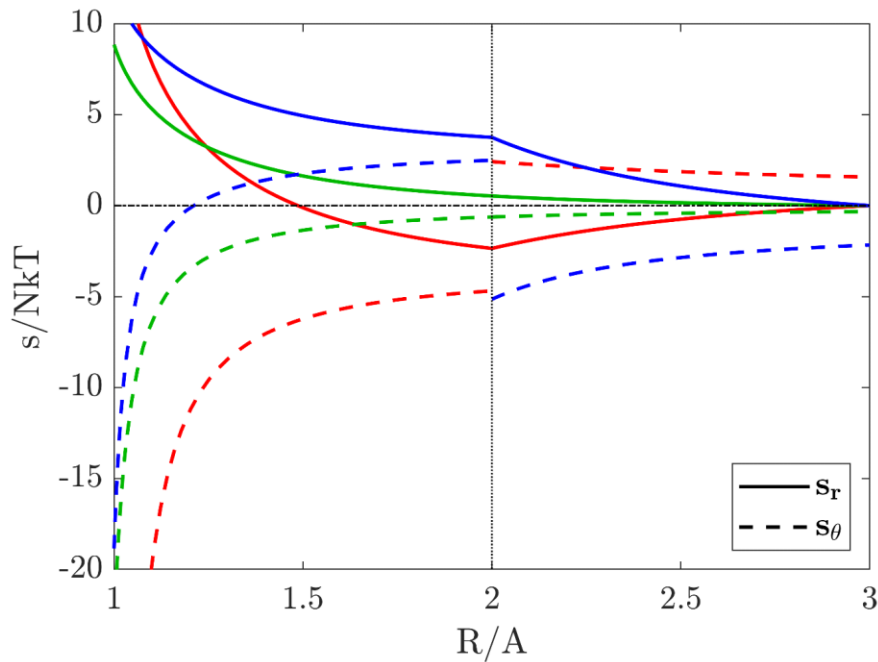
74
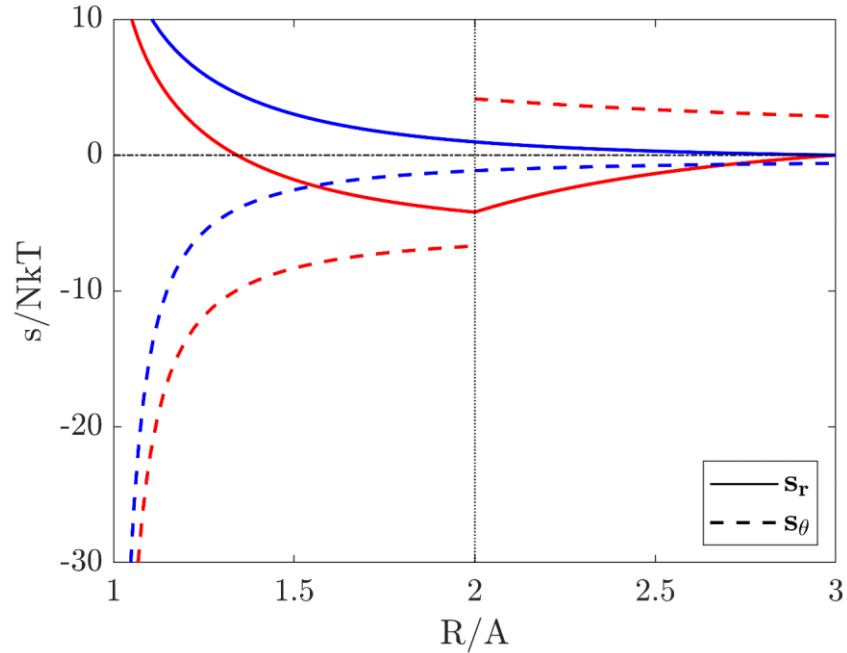
Figure 5-13. Variation of the principle nominal stresses with respect to the dimensionless dry hydrogel radius in an equilibrium state of one soft spherical hydrogel layer enclosed by an extremely stiff hydrogel layer.

As one application of the present case study, a polymer hydrogel can be used to block the leakage of water or an aqueous solution in pipe joints, cavities, or porous structures. In this case, after imbibing water, the hydrogel will swell and seal the cavities to block leakage. The present study gives a detailed rational justification on how to design and optimize the material properties and structural geometries of a bi-layered hydrogel system to reach the targeted water concentration and sealing stresses.

5.4. Concluding Remarks

In summary, a swelling mechanics model was successfully formulated for determining the displacement, stretch, stress, and water concentration fields of a spherical bi-layered hydrogel bonded on a hard core. The problem was reduced to solve a two-point boundary value problem

of a 2nd-order nonlinear ODE. In the limiting case of a single hydrogel layer, the present model has been validated by literature results. The effects of material properties on the displacement, stretch, stress, and water concentration fields of the hydrogel layers were examined in detail. The scaling results provide the rational basis for the design and optimization of hydrogel systems for controlled swelling in broad applications such as drug delivery, tissue engineering, leakage blocking, etc.

CHAPTER 6. CONCLUSIONS AND SUGGESTIONS FOR FUTURE WORKS

6.1. Conclusions

The research work of this dissertation was focused on the fundamental understanding of the circumferential wrinkling on electrospun soft nanofibers and the swelling mechanics of composite hydrogels as electrospun nanofibers and hydrogels have been finding broad applications in various engineering sectors. The outcomes of the present theoretical and computational studies can be employed for quality control and intelligent fabrication of continuous nanofibers by electrospinning and active control of the swelling behaviors of hydrogels in biomedical applications, etc. The research results of the dissertation can be summarized below.

For the first objective as covered in Chapter 3, a 1D continuum mechanics model has been successfully formulated, which is capable of understanding the mechanism of circumferential surface wrinkling of soft polymer nanofibers under axial stretching. During the modeling process, the material of the soft polymer nanofibers was treated as homogeneous, isotropic, hyperelastic neo-Hookean solid. The resulting ODE that governs the circumferential wrinkling has been determined. The critical axial stretch to trigger circumferential wrinkling has been gained in explicit expression. In addition, this study first discovered the unique spontaneous circumferential wrinkling in electrospun soft nanofibers that is evoked purely by surface energy at zero axial stretch, and the related critical fiber radius was determined. Such critical fiber radius is technically important to electrospinning practice as it determines the theoretical minimum fiber radius that can be realized in electrospinning, i.e., below this minimum fiber radius, continuous nanofibers cannot be fabricated by electrospinning due to the jet beading instability. Furthermore, detailed numerical scaling analysis has been performed to illustrate the

77

dependencies of critical axial stretch and critical fiber radius upon the material properties and geometries of the soft nanofibers. This study provides the rational basis of circumferential wrinkling phenomenon commonly observed in soft polymer nanofibers produced by electrospinning. The study also demonstrated a potential technique to actively tune the surface morphology of soft polymer nanofibers via axial stretching to induce circumferential wrinkling.

In Chapter 4, which covers the second objective of this thesis work, a feasible technique of incorporating hard cores into the soft ultrathin fibers via co-electrospinning was proposed and numerically verified for actively regulating the circumferential wrinkle modes of ultrathin polymer fibers. The dependencies of surface wrinkle modes of these core-shell polymer fibers enwrapped with hard cores upon the thickness and stiffness of the glassy shell and inner soft sol-gel layers have been obtained via detailed FEA-based nonlinear buckling analysis, which provide a theoretical background for producing ultrathin polymer micro/nanofibers with controlled surface morphologies. Such electrospun nanofibers carry greatly enhanced specific surface areas suitable for use in oil-water separation, fine filtration, drug delivery, catalyst carriers, tissue scaffolding, etc.

Chapter 5 covers the third objective. A swelling mechanics model was formulated successfully for determining the displacement, stretch, stress, and water concentration fields of a bi-layered spherical hydrogel bonded on a hard core. This problem was reduced to solve a two-point boundary value problem of a 2nd-order nonlinear ODE. In the limiting case of a single hydrogel layer, the present model was validated by the literature results. The effects of material properties on the physical quantity fields of the hydrogel layers were examined in detail, which provides the theoretical supports of broad opportunities to design and optimize hydrogel systems

for controlled swelling in extensive applications such as drug delivery, tissue engineering, leakage blocking, etc.

6.2. Suggestions for Future Works

As an extension of the present thesis studies, several research topics can be further considered to refine and advance the understanding of these topics.

- Significant solvent evaporation (drying) is the unique feature in the electrospinning process, which unavoidably induces inhomogeneous microstructure and related physical and mechanical properties across the resulting nanofibers. Thus, with available nanotechnology to measure the gradient of the mechanical properties across the nanofibers, an improved continuum mechanics model taking into account such gradient can be established to refine the prediction of the circumferential wrinkling on electrospun nanofibers.

- It is desirable to combine the effects of both residual strain and mismatch strain to predict the final wrinkle mode in electrospun nanofibers, as both of these strains may occur in the process of nanofiber formation. Both analytical and computational (finite element method-FEM) models can be formulated and implemented for such effects.

- It is technologically very important to formulate a temporal continuum mechanics model of electrospinning jet to simulate the time-dependent wrinkling process during drying, which can comprehensively take into account the effects of material properties of polymers, solvents, drying process, etc. on the fiber formation and wrinkling evolution.

- Co-electrospinning core-shell nanofibers containing hard cores of different sizes can be made to evaluate the computational results predicted in the present thesis work.

79

- Swelling of soft hydrogels may lead to various structural instabilities. It is scientifically interesting and technologically important to predict the critical conditions of composite hydrogels made of multiple monolithic hydrogels. More importantly, it is useful to formulate the temporal field theories of composite hydrogels to address their time-dependent deformation, stress, and water concentration fields and structural instabilities during constrained swelling.

REFERENCES

Ahmadi, M., & Wu, X. F. (2019). Tunable wrinkle modes of core-shell polymer fibers in electrospinning. *Journal of Physics Communications, 3*(4), 045001.

Ahmed, E. M. (2015). Hydrogel: Preparation, characterization, and applications: A review. *Journal of Advanced Research, 6*(2), 105-121.

Arinstein, A., Burman, M., Gendelman, O., & Zussman, E. (2007). Effect of supramolecular structure on polymer nanofibre elasticity. *Nature Nanotechnology, 2*(1), 59.

Ballauff, M., & Lu, Y. (2007). "Smart" nanoparticles: preparation, characterization and applications. *Polymer, 48*(7), 1815-1823.

Barhate, R. S., & Ramakrishna, S. (2007). Nanofibrous filtering media: filtration problems and solutions from tiny materials. *Journal of Membrane Science, 296*(1-2), 1-8.

Barnes, C. P., Sell, S. A., Boland, E. D., Simpson, D. G., & Bowlin, G. L. (2007). Nanofiber technology: designing the next generation of tissue engineering scaffolds. *Advanced Drug Delivery Reviews, 59*(14), 1413-1433.

Beebe, D. J., Moore, J. S., Bauer, J. M., Yu, Q., Liu, R. H., Devadoss, C., & Jo, B. H. (2000). Functional hydrogel structures for autonomous flow control inside microfluidic channels. *Nature, 404*(6778), 588-590.

Biot, M. A. (1941). General theory of three-dimensional consolidation. *Journal of applied physics, 12*(2), 155-164.

Bognitzki, M., Czado, W., Frese, T., Schaper, A., Hellwig, M., Steinhart, M., ... & Wendorff, J. H. (2001). Nanostructured fibers via electrospinning. *Advanced Materials, 13*(1), 70-72.

Burger, C., Hsiao, B. S., & Chu, B. (2006). Nanofibrous materials and their applications. *Annual Review of Materials Research, 36*, 333-368.

Cassie, A. B. D., & Baxter, S. (1944). Wettability of porous surfaces. *Transactions of the Faraday society, 40*, 546-551.

Chen, Q., Zhang, L., Rahman, A., Zhou, Z., Wu, X. F., & Fong, H. (2011). Hybrid multi-scale epoxy composite made of conventional carbon fiber fabrics with interlaminar regions containing electrospun carbon nanofiber mats. *Composites Part A: Applied Science and Manufacturing, 42*(12), 2036-2042.

Chew, S. Y., Wen, Y., Dzenis, Y., & Leong, K. W. (2006). The role of electrospinning in the emerging field of nanomedicine. *Current Pharmaceutical Design, 12*(36), 4751-4770.

Cho, E. C., Kim, J. W., Fernández-Nieves, A., & Weitz, D. A. (2008). Highly responsive hydrogel scaffolds formed by three-dimensional organization of microgel nanoparticles. *Nano Letters, 8*(1), 168-172.

Ciarletta, P., Destrade, M., Gower, A. L., & Taffetani, M. (2016). Morphology of residually stressed tubular tissues: Beyond the elastic multiplicative decomposition. *Journal of the Mechanics and Physics of Solids, 90*, 242-253.

Cowin, S. C., & Doty, S. B. (2007). *Tissue mechanics*. Springer Science & Business Media.

Crassous, J. J., Ballauff, M., Drechsler, M., Schmidt, J., & Talmon, Y. (2006). Imaging the volume transition in thermosensitive core-shell particles by cryo-transmission electron microscopy. *Langmuir, 22*(6), 2403-2406.

Cuenot, S., Demoustier-Champagne, S., & Nysten, B. (2000). Elastic modulus of polypyrrole nanotubes. *Physical Review Letters, 85*(8), 1690.

Dayal, P., Liu, J., Kumar, S., & Kyu, T. (2007). Experimental and theoretical investigations of porous structure formation in electrospun fibers. *Macromolecules, 40*(21), 7689-7694.

Discher, D. E., Mooney, D. J., & Zandstra, P. W. (2009). Growth factors, matrices, and forces combine and control stem cells. *Science, 324*(5935), 1673-1677.

Dong, L., Agarwal, A. K., Beebe, D. J., & Jiang, H. (2006). Adaptive liquid microlenses activated by stimuli-responsive hydrogels. *Nature, 442*(7102), 551-554.

Dong, Z., Kennedy, S. J., & Wu, Y. (2011). Electrospinning materials for energy-related applications and devices. *Journal of Power Sources, 196*(11), 4886-4904.

Drury, J. L., & Mooney, D. J. (2003). Hydrogels for tissue engineering: scaffold design variables and applications. *Biomaterials, 24*(24), 4337-4351.

Duncan, R. (2003). The dawning era of polymer therapeutics. *Nature Reviews Drug Discovery, 2*(5), 347-360.

Dzenis, Y. (2004). Spinning continuous fibers for nanotechnology. *Science, 304*(5679), 1917-1919.

Dzenis, Y. (2008). Structural nanocomposites. *Science, 319*(5862), 419-420.

Feng, J. J. (2002). The stretching of an electrified non-Newtonian jet: A model for electrospinning. *Physics of Fluids, 14*(11), 3912-3926.

Feng, J. J. (2003). Stretching of a straight electrically charged viscoelastic jet. *Journal of Non-Newtonian Fluid Mechanics, 116*(1), 55-70.

Fischel-Ghodsian, F., Brown, L., Mathiowitz, E., Brandenburg, D., & Langer, R. (1988). Enzymatically controlled drug delivery. *Proceedings of the National Academy of Sciences, 85*(7), 2403-2406.

Flory, P. J. (1953). *Principles of Polymer Chemistry*. Cornell University Press.

Flory, P. J., & Rehner Jr, J. (1943). Statistical Mechanics of Cross-Linked Polymer Networks II. Swelling. *The Journal of Chemical Physics, 11*(11), 521.

Gibbs, J. W. (1906). *The scientific papers of J. Willard Gibbs* (Vol. 1). Longmans, Green and Company.

Gibson, P., Schreuder-Gibson, H., & Rivin, D. (2001). Transport properties of porous membranes based on electrospun nanofibers. *Colloids and Surfaces A: Physicochemical and Engineering Aspects, 187*, 469-481.

Gopal, R., Kaur, S., Ma, Z., Chan, C., Ramakrishna, S., & Matsuura, T. (2006). Electrospun nanofibrous filtration membrane. *Journal of Membrane Science, 281*(1-2), 581-586.

Guo, J., Yang, W., Deng, Y., Wang, C., & Fu, S. (2005). Organic-dye-coupled magnetic nanoparticles encaged inside thermoresponsive PNIPAM microcapsules. *Small, 1*(7), 737-743.

Hennink, W. E., & van Nostrum, C. F. (2002). Novel crosslinking methods to design hydrogels. *Advanced Drug Delivery Reviews, 54*(1), 13-36.

Herrmann, G., & Forrestal, M. J. (1965). Buckling of a long cylindrical shell containing an elastic core. *AIAA Journal, 3*(9), 1710-1715.

Hohman, M. M., Shin, M., Rutledge, G., & Brenner, M. P. (2001). Electrospinning and electrically forced jets. II. Applications. *Physics of Fluids, 13*(8), 2221-2236.

Hong, W., Zhao, X., & Suo, Z. (2008a). Drying-induced bifurcation in a hydrogel-actuated nanostructure. *Journal of Applied Physics, 104*(8), 084905.

Hong, W., Zhao, X., Zhou, J., & Suo, Z. (2008b). A theory of coupled diffusion and large deformation in polymeric gels. *Journal of the Mechanics and Physics of Solids, 56*(5), 1779-1793.

Hong, W., Liu, Z., & Suo, Z. (2009). Inhomogeneous swelling of a gel in equilibrium with a solvent and mechanical load. *International Journal of Solids and Structures, 46*(17), 3282-3289.

Hong, W., Zhao, X., & Suo, Z. (2010). Large deformation and electrochemistry of polyelectrolyte gels. *Journal of the Mechanics and Physics of Solids, 58*(4), 558-577.

Hosseini Farid, M., Ramzanpour, M., Ziejewski, M., & Karami, G. (2019). A constitutive material model with strain-rate dependency for brain tissue. In *ASME International Mechanical Engineering Congress and Exposition* (Vol. 59407, p. V003T04A004). American Society of Mechanical Engineers.

Hu, Z., Zhang, X., & Li, Y. (1995). Synthesis and application of modulated polymer gels. *Science, 269*(5223), 525-527.

Huang, Z. M., Zhang, Y. Z., Kotaki, M., & Ramakrishna, S. (2003). A review on polymer nanofibers by electrospinning and their applications in nanocomposites. *Composites Science and Technology, 63*(15), 2223-2253.

Ichikawa, H., & Fukumori, Y. (2000). A novel positively thermosensitive controlled-release microcapsule with membrane of nano-sized poly (N-isopropylacrylamide) gel dispersed in ethylcellulose matrix. *Journal of Controlled Release, 63*(1-2), 107-119.

Inai, R., Kotaki, M., & Ramakrishna, S. (2005). Structure and properties of electrospun PLLA single nanofibres. *Nanotechnology, 16*(2), 208.

Jagur-Grodzinski, J. (2006). Polymers for tissue engineering, medical devices, and regenerative medicine. Concise general review of recent studies. *Polymers for Advanced Technologies, 17*(6), 395-418.

Jahani, B., Brooks, A., & Azarmi, F. (2018). Development of antibacterial surfaces via thermal spray coating techniques. *Biomedical Sciences Instrumentation, 54*(1), 116-122.

Jahani, B., Meesterb, K., Wanga, X., & Brooksc, A. (2020). Biodegradable magnesium-based alloys for bone repair applications: prospects and challenges. *Biomedical Sciences Instrumentation, 56*(2), 292-304.

Jeong, B., Bae, Y. H., Lee, D. S., & Kim, S. W. (1997). Biodegradable block copolymers as injectable drug-delivery systems. *Nature, 388*(6645), 860-862.

Ji, Y., Li, B., Ge, S., Sokolov, J. C., & Rafailovich, M. H. (2006). Structure and nanomechanical characterization of electrospun PS/clay nanocomposite fibers. *Langmuir, 22*(3), 1321-1328.

Ji, L., & Zhang, X. (2009). Electrospun carbon nanofibers containing silicon particles as an energy-storage medium. *Carbon, 47*(14), 3219-3226.

Joshi, P., Zhou, Z., Poudel, P., Thapa, A., Wu, X. F., & Qiao, Q. (2012). Nickel incorporated carbon nanotube/nanofiber composites as counter electrodes for dye-sensitized solar cells. *Nanoscale, 4*(18), 5659-5664.

Kenawy, E. R., Bowlin, G. L., Mansfield, K., Layman, J., Simpson, D. G., Sanders, E. H., & Wnek, G. E. (2002). Release of tetracycline hydrochloride from electrospun poly (ethylene-co-vinylacetate), poly (lactic acid), and a blend. *Journal of Controlled Release, 81*(1-2), 57-64.

Kim, J. S., & Reneker, D. H. (1999). Mechanical properties of composites using ultrafine electrospun fibers. *Polymer Composites, 20*(1), 124-131.

Kim, S. J., Spinks, G. M., Prosser, S., Whitten, P. G., Wallace, G. G., & Kim, S. I. (2006). Surprising shrinkage of expanding gels under an external load. *Nature Materials, 5*(1), 48-51.

Kim, C., Ngoc, B. T., Yang, K. S., Kojima, M., Kim, Y. A., Kim, Y. J., ... & Yang, S. C. (2007). Self-sustained thin webs consisting of porous carbon nanofibers for supercapacitors via the electrospinning of polyacrylonitrile solutions containing zinc chloride. *Advanced Materials, 19*(17), 2341-2346.

Kirichenko, V. N., Petryanov-Sokolov, I. V., Suprun, N. N., & Shutov, A. A. (1986). Asymptotic radius of a slightly conducting liquid jet in an electric field. *Soviet Physics Doklady, 31*, 611-613.

Klein, Y., Efrati, E., & Sharon, E. (2007). Shaping of elastic sheets by prescription of non-Euclidean metrics. *Science, 315*(5815), 1116-1120.

Koombhongse, S., Liu, W., & Reneker, D. H. (2001). Flat polymer ribbons and other shapes by electrospinning. *Journal of Polymer Science Part B: Polymer Physics, 39*(21), 2598-2606.

Kopeček, J. (2002). Swell gels. *Nature, 417*(6887), 389-391.

Ladet, S., David, L., & Domard, A. (2008). Multi-membrane hydrogels. *Nature, 452*(7183), 76-79.

Lai, C., Guo, Q., Wu, X. F., Reneker, D. H., & Hou, H. (2008). Growth of carbon nanostructures on carbonized electrospun nanofibers with palladium nanoparticles. *Nanotechnology, 19*(19), 195303.

Langer, R. (1998). Drug delivery and targeting. *Nature, 392*, 5-10.

Lee, K. Y., & Mooney, D. J. (2001). Hydrogels for tissue engineering. *Chemical Reviews, 101*(7), 1869-1880.

Li, W. J., Laurencin, C. T., Caterson, E. J., Tuan, R. S., & Ko, F. K. (2002). Electrospun nanofibrous structure: a novel scaffold for tissue engineering. *Journal of Biomedical Materials Research: An Official Journal of The Society for Biomaterials, The Japanese Society for Biomaterials, and The Australian Society for Biomaterials and the Korean Society for Biomaterials, 60*(4), 613-621.

Li, D., & Xia, Y. (2004a). Electrospinning of nanofibers: reinventing the wheel?. *Advanced Materials, 16(*14), 1151-1170.

Li, D., & Xia, Y. (2004b). Direct fabrication of composite and ceramic hollow nanofibers by electrospinning. *Nano letters, 4*(5), 933-938.

Li, H., Luo, R., Birgersson, E., & Lam, K. Y. (2007). Modeling of multiphase smart hydrogels responding to p H and electric voltage coupled stimuli. *Journal of Applied Physics, 101*(11), 114905.

Li, J., Celiz, A. D., Yang, J., Yang, Q., Wamala, I., Whyte, W., ... & Mooney, D. J. (2017). Tough adhesives for diverse wet surfaces. *Science, 357*(6349), 378-381.

Liang, D., Hsiao, B. S., & Chu, B. (2007). Functional electrospun nanofibrous scaffolds for biomedical applications. *Advanced Drug Delivery Reviews, 59*(14), 1392-1412.

Luo, Y., & Shoichet, M. S. (2004). A photolabile hydrogel for guided three-dimensional cell growth and migration. *Nature Materials, 3*(4), 249-253.

Matthews, J. A., Wnek, G. E., Simpson, D. G., & Bowlin, G. L. (2002). Electrospinning of collagen nanofibers. *Biomacromolecules, 3*(2), 232-238.

Maze, B., Tafreshi, H. V., Wang, Q., & Pourdeyhimi, B. (2007). A simulation of unsteady-state filtration via nanofiber media at reduced operating pressures. *Journal of Aerosol Science, 38*(5), 550-571.

Mora, S., Phou, T., Fromental, J. M., Pismen, L. M., & Pomeau, Y. (2010). Capillarity driven instability of a soft solid. *Physical Review Letters, 105*(21), 214301.

Mohammadzadehmoghadam, S., Dong, Y., & Jeffery Davies, I. (2015). Recent progress in electrospun nanofibers: reinforcement effect and mechanical performance. *Journal of Polymer Science Part B: Polymer Physics, 53*(17), 1171-1212.

Nakahama, K., & Fujimoto, K. (2002). Thermosensitive two-dimensional arrays of hydrogel particles. *Langmuir, 18*(26), 10095-10099.

Naraghi, M., Chasiotis, I., Kahn, H., Wen, Y., & Dzenis, Y. (2007a). Mechanical deformation and failure of electrospun polyacrylonitrile nanofibers as a function of strain rate. *Applied Physics Letters, 91*(15), 151901.

Naraghi, M., Chasiotis, I., Kahn, H., Wen, Y., & Dzenis, Y. (2007b). Novel method for mechanical characterization of polymeric nanofibers. *Review of Scientific Instruments, 78*(8), 085108.

Nayak, S., & Lyon, L. A. (2005). Soft nanotechnology with soft nanoparticles. *Angewandte Chemie International Edition, 44*(47), 7686-7708.

Nowak, A. P., Breedveld, V., Pakstis, L., Ozbas, B., Pine, D. J., Pochan, D., & Deming, T. J. (2002). Rapidly recovering hydrogel scaffolds from self-assembling diblock copolypeptide amphiphiles. *Nature, 417*(6887), 424-428.

Pai, C. L., Boyce, M. C., & Rutledge, G. C. (2009). Morphology of porous and wrinkled fibers of polystyrene electrospun from dimethylformamide. *Macromolecules, 42*(6), 2102-2114.

Pelton, R. (2000). Temperature-sensitive aqueous microgels. *Advances in Colloid and Interface Science, 85*(1), 1-33.

Peppas, N. A., Huang, Y., Torres-Lugo, M., Ward, J. H., & Zhang, J. (2000). Physicochemical foundations and structural design of hydrogels in medicine and biology. *Annual Review of Biomedical Engineering, 2*(1), 9-29.

Peppas, N. A., Hilt, J. Z., Khademhosseini, A., & Langer, R. (2006). Hydrogels in biology and medicine: from molecular principles to bionanotechnology. *Advanced Materials, 18*(11), 1345-1360.

Pham, Q. P., Sharma, U., & Mikos, A. G. (2006). Electrospinning of polymeric nanofibers for tissue engineering applications: a review. *Tissue Engineering, 12*(5), 1197-1211.

Popadyuk, N., Zholobko, O., Donchak, V., Harhay, K., Budishevska, O., Voronov, A., ... & Voronov, S. (2014). Ionically and covalently crosslinked hydrogel particles based on chitosan and poly (ethylene glycol). *Chemistry & Chemical Technology, 8*(2), 171-176.

Qiu, Y., & Park, K. (2001). Environment-sensitive hydrogels for drug delivery. *Advanced Drug Delivery Reviews, 53*(3), 321-339.

Ramzanpour, M., Hosseini-Farid, M., Ziejewski, M., & Karami, G. (2019). Particle swarm optimization method for hyperelastic characterization of soft tissues. In *ASME International Mechanical Engineering Congress and Exposition* (Vol. 59469, p. V009T11A028). American Society of Mechanical Engineers.

Ramzanpour, M., Hosseini-Farid, M., McLean, J., Ziejewski, M., & Karami, G. (2020a). Visco-hyperelastic characterization of human brain white matter micro-level constituents in different strain rates. *Medical & Biological Engineering & Computing*, 1-12.

Ramzanpour, M., Hosseini-Farid, M., Ziejewski, M., & Karami, G. (2020b). A constrained particle swarm optimization algorithm for hyperelastic and visco-hyperelastic characterization of soft biological tissues. *International Journal for Computational Methods in Engineering Science and Mechanics*, 1-16.

Raschip, I. E., Vasile, C., Ciolacu, D., & Cazacu, G. (2007). Semi-interpenetrating polymer networks containing polysaccharides. I Xanthan/Lignin networks. *High Performance Polymers, 19*(5-6), 603-620.

Reneker, D. H., & Chun, I. (1996). Nanometre diameter fibres of polymer, produced by electrospinning. *Nanotechnology, 7*(3), 216.

Reneker, D. H., Yarin, A. L., Fong, H., & Koombhongse, S. (2000). Bending instability of electrically charged liquid jets of polymer solutions in electrospinning. *Journal of Applied Physics, 87*(9), 4531-4547.

Reneker, D. H., Yarin, A. L., Zussman, E., & Xu, H. (2007). Electrospinning of nanofibers from polymer solutions and melts. *Advances in Applied Mechanics, 41*, 43-346.

Reneker, D. H., & Yarin, A. L. (2008). Electrospinning jets and polymer nanofibers. *Polymer, 49*(10), 2387-2425.

Saville, D. A. (1997). Electrohydrodynamics: the Taylor-Melcher leaky dielectric model. *Annual Review of Fluid Mechanics, 29*(1), 27-64.

Schulz, D. L., Hoey, J., Smith, J., Elangovan, A., Wu, X., Akhatov, I., ... & Xiao, J. (2010). Si6H12/Polymer inks for electrospinning a-Si nanowire lithium ion battery anodes. *Electrochemical and Solid-State Letters, 13*(10), A143-A145.

Shibayama, M., & Tanaka, T. (1993). Volume phase transition and related phenomena of polymer gels. *Advances in Polymer Science, 109*, 1-62.

Shin, Y. M., Hohman, M. M., Brenner, M. P., & Rutledge, G. C. (2001). Electrospinning: A whipping fluid jet generates submicron polymer fibers. *Applied Physics Letters, 78*(8), 1149-1151.

Sidorenko, A., Krupenkin, T., Taylor, A., Fratzl, P., & Aizenberg, J. (2007). Reversible switching of hydrogel-actuated nanostructures into complex micropatterns. *Science, 315*(5811), 487-490.

Sinha-Ray, S., Pelot, D. D., Zhou, Z. P., Rahman, A., Wu, X. F., & Yarin, A. L. (2012). Encapsulation of self-healing materials by coelectrospinning, emulsion electrospinning, solution blowing and intercalation. *Journal of Materials Chemistry, 22*(18), 9138-9146.

Smith, D. J., Kataphinan, W., Reneker, D. H., & Dabney, S. (2004a). *U.S. Patent No. 6,821,479*. Washington, DC: U.S. Patent and Trademark Office.

Smith, D. J., Reneker, D. H., McManus, A. T., Schreuder-Gibson, H. L., Mello, C., & Sennett, M. S. (2004b). *U.S. Patent No. 6,753,454*. Washington, DC: U.S. Patent and Trademark Office.

Southern, E., & Thomas, A. G. (1965). Effect of constraints on the equilibrium swelling of rubber vulcanizates. *Journal of Polymer Science Part A: General Papers, 3*(2), 641-646.

Spivak, A. F., & Dzenis, Y. A. (1998). Asymptotic decay of radius of a weakly conductive viscous jet in an external electric field. *Applied Physics Letters, 73*(21), 3067-3069.

Spivak, A. F., Dzenis, Y., & Reneker, D. H. (2000). Model of steady state jet in the electrospinning process. *Mechanics Research Communications, 27*(1), 37-42.

Sun, J. Y., Zhao, X., Illeperuma, W. R., Chaudhuri, O., Oh, K. H., Mooney, D. J., ... & Suo, Z. (2012). Highly stretchable and tough hydrogels. *Nature, 489*(7414), 133-136.

Taffetani, M., & Ciarletta, P. (2015a). Elastocapillarity can control the formation and the morphology of beads-on-string structures in solid fibers. *Physical Review E, 91*(3), 032413.

Taffetani, M., & Ciarletta, P. (2015b). Beading instability in soft cylindrical gels with capillary energy: weakly non-linear analysis and numerical simulations. *Journal of the Mechanics and Physics of Solids, 81*, 91-120.

Tan, E. P. S., & Lim, C. T. (2004). Novel approach to tensile testing of micro-and nanoscale fibers. *Review of Scientific Instruments, 75*(8), 2581-2585.

Tan, E. P. S., Goh, C. N., Sow, C. H., & Lim, C. T. (2005a). Tensile test of a single nanofiber using an atomic force microscope tip. *Applied Physics Letters, 86*(7), 073115.

Tan, E. P. S., Ng, S. Y., & Lim, C. T. (2005b). Tensile testing of a single ultrafine polymeric fiber. *Biomaterials, 26*(13), 1453-1456.

Tan, E. P. S., & Lim, C. T. (2006). Mechanical characterization of nanofibers–a review. *Composites Science and Technology, 66*(9), 1102-1111.

Tanaka, T. (1981). Gels. *Scientific American, 244*(1), 124-S.

Tang, S., Li, Y., Kam Liu, W., Hu, N., He Peng, X., & Guo, Z. (2015). Tensile stress-driven surface wrinkles on cylindrical core–shell soft solids. *Journal of Applied Mechanics, 82*(12).

Taylor, G. I. (1969). Electrically driven jets. *Proceedings of the Royal Society of London. A. Mathematical and Physical Sciences, 313*(1515), 453-475.

Trujillo, V., Kim, J., & Hayward, R. C. (2008). Creasing instability of surface-attached hydrogels. *Soft Matter, 4*(3), 564-569.

Vodná, L., Bubeníková, S., & Bakoš, D. (2007). Chitosan based hydrogel microspheres as drug carriers. *Macromolecular Bioscience, 7*(5), 629-634.

Walker, B. W., Lara, R. P., Mogadam, E., Yu, C. H., Kimball, W., & Annabi, N. (2019). Rational design of microfabricated electroconductive hydrogels for biomedical applications. *Progress in Polymer Science, 92*, 135-157.

Wang, L., Pai, C. L., Boyce, M. C., & Rutledge, G. C. (2009). Wrinkled surface topographies of electrospun polymer fibers. *Applied Physics Letters, 94*(15), 151916.

Wei, H., Zhang, X. Z., Zhou, Y., Cheng, S. X., & Zhuo, R. X. (2006). Self-assembled thermoresponsive micelles of poly (N-isopropylacrylamide-b-methyl methacrylate). *Biomaterials, 27*(9), 2028-2034.

Wenzel, R. N. (1936). Resistance of solid surfaces to wetting by water. *Industrial & Engineering Chemistry, 28*(8), 988-994.

Wenzel, R. N. (1949). Surface roughness and contact angle. *The Journal of Physical Chemistry, 53*(9), 1466-1467.

Wichterle, O., & Lim, D. (1960). Hydrophilic gels for biological use. *Nature, 185*(4706), 117-118.

Wong, A. P., Perez-Castillejos, R., Love, J. C., & Whitesides, G. M. (2008). Partitioning microfluidic channels with hydrogel to construct tunable 3-D cellular microenvironments. *Biomaterials, 29*(12), 1853-1861.

Wu, X. F., & Dzenis, Y. A. (2005). Elasticity of planar fiber networks. *Journal of Applied Physics, 98*(9), 093501.

Wu, X. F., & Dzenis, Y. A. (2006). Wave propagation in nanofibers. *Journal of Applied Physics, 100*(12), 124318.

Wu, X. F., & Dzenis, Y. A. (2007a). Size effect in polymer nanofibers under tension. *Journal of Applied Physics, 102*(4), 044306.

Wu, X. F., & Dzenis, Y. A. (2007b). Adhesive contact in filaments. *Journal of Physics D: Applied Physics, 40*(14), 4276.

Wu, X. F., & Dzenis, Y. A. (2007c). Collapse analysis of nanofibres. *Nanotechnology, 18*(28), 285702.

Wu, X. F., Kostogorova-Beller, Y. Y., Goponenko, A. V., Hou, H., & Dzenis, Y. A. (2008). Rippling of polymer nanofibers. *Physical Review E, 78*(6), 061804.

Wu, X. (2009). *Fracture of Advanced Composites with Nanofiber Reinforced Interfaces: Fabrication, Characterization and Modeling*. VDM Publishing.

Wu, X. F. (2010). Wave propagation in prestretched polymer nanofibers. *Journal of Applied Physics, 107*(1), 013509.

Wu, X. F., Bedarkar, A., & Akhatov, I. S. (2010). Hydroelastic analysis of an axially loaded compliant fiber wetted with a droplet. *Journal of Applied Physics, 108*(8), 083518.

Wu, X. F., Salkovskiy, Y., & Dzenis, Y. A. (2011). Modeling of solvent evaporation from polymer jets in electrospinning. *Applied Physics Letters, 98*(22), 223108.

Wu, X. F., Zhou, Z., & Zhou, W. M. (2012). Electrical contact resistance in filaments. *Applied Physics Letters, 100*(19), 193115.

Wu, X. F., & Yarin, A. L. (2013). Recent progress in interfacial toughening and damage self-healing of polymer composites based on electrospun and solution-blown nanofibers: An overview. *Journal of Applied Polymer Science, 130*(4), 2225-2237.

Wu, X. F., Rahman, A., Zhou, Z., Pelot, D. D., Sinha-Ray, S., Chen, B., ... & Yarin, A. L. (2013). Electrospinning core-shell nanofibers for interfacial toughening and self-healing

of carbon-fiber/epoxy composites. *Journal of Applied Polymer Science, 129*(3), 1383-1393.

Wu, X. F., Zhou, Z., Zholobko, O., Jenniges, J. J., Baatz, B., Ahmadi, M., & Chen, J. (2020). Critical condition of electrohydrodynamic jetting from a polymer-solution droplet on a conductive wire. *Journal of Applied Physics, 127*(5), 054303.

Xie, J., Li, X., & Xia, Y. (2008). Putting electrospun nanofibers to work for biomedical research. *Macromolecular Rapid Communications, 29*(22), 1775-1792.

Yarin, A. L., Koombhongse, S., & Reneker, D. H. (2001a). Bending instability in electrospinning of nanofibers. *Journal of Applied Physics, 89*(5), 3018-3026.

Yarin, A. L., Koombhongse, S., & Reneker, D. H. (2001b). Taylor cone and jetting from liquid droplets in electrospinning of nanofibers. *Journal of Applied Physics, 90*(9), 4836-4846.

Yu, M. (2013). *Theoretical and Experimental Studies of Droplets Wetting on Micro/Nano-Fibrous Materials and their Applications in Oil-Water Separation* (Publication No. 1548656) [Master's Thesis, North Dakota State University]. ProQuest Dissertations Publishing.

Yuya, P. A., Wen, Y., Turner, J. A., Dzenis, Y. A., & Li, Z. (2007). Determination of Young's modulus of individual electrospun nanofibers by microcantilever vibration method. *Applied Physics Letters, 90*(11), 111909.

Zhang, Y., Matsumoto, E. A., Peter, A., Lin, P. C., Kamien, R. D., & Yang, S. (2008). One-step nanoscale assembly of complex structures via harnessing of an elastic instability. *Nano Letters, 8*(4), 1192-1196.

Zhang, X., Ji, L., Toprakci, O., Liang, Y., & Alcoutlabi, M. (2011). Electrospun nanofiber-based anodes, cathodes, and separators for advanced lithium-ion batteries. *Polymer Reviews, 51*(3), 239-264.

Zhao, R., & Zhao, X. (2017). Multimodal surface instabilities in curved film–substrate structures. *Journal of Applied Mechanics, 84*(8).

Zhao, X., Hong, W., & Suo, Z. (2008a). Inhomogeneous and anisotropic equilibrium state of a swollen hydrogel containing a hard core. *Applied Physics Letters, 92*(5), 051904.

Zhao, X., Hong, W., & Suo, Z. (2008b). Stretching and polarizing a dielectric gel immersed in a solvent. *International Journal of Solids and Structures, 45*(14-15), 4021-4031.

Zholobko, O. Y., Tarnavchyk, I. T., Voronov, A. S., Budishevska, O. G., Kohut, A. M., & Voronov, S. A. (2014a). Peculiarities of the development of hydrogels based on chitosan and poly (ethylene glycol) disuccinate at elevated temperature. *Reports of the National Academy of Sciences of Ukraine, 5*, 128-137.

Zholobko, O. Y., Tarnavchyk, I. T., Voronov, A. S., Demchuk, Z. I., Budishevska, O. G., Kohut, A. M., & Voronov, S. A. (2014b). Formation of hydrogels based on chitosan and poly (ethylene glycol) disuccinates. *Polym. J., 36* (1), 78-84

Zhou, Z., Wu, X. F., & Fong, H. (2012). Electrospun carbon nanofibers surface-grafted with vapor-grown carbon nanotubes as hierarchical electrodes for supercapacitors. *Applied Physics Letters, 100*(2), 023115.

Zhou, Z., & Wu, X. F. (2013). Graphene-beaded carbon nanofibers for use in supercapacitor electrodes: Synthesis and electrochemical characterization. *Journal of Power Sources, 222*, 410-416.

Zhou, Z., & Wu, X. F. (2014). High-performance porous electrodes for pseudosupercapacitors based on graphene-beaded carbon nanofibers surface-coated with nanostructured conducting polymers. *Journal of Power Sources, 262*, 44-49.

Zhou, Z., Wu, X. F., & Hou, H. (2014). Electrospun carbon nanofibers surface-grown with carbon nanotubes and polyaniline for use as high-performance electrode materials of supercapacitors. *RSC Advances, 4*(45), 23622-23629.

Zhou, Z., & Wu, X. F. (2015). Electrospinning superhydrophobic–superoleophilic fibrous PVDF membranes for high-efficiency water–oil separation. *Materials Letters, 160*, 423-427.

Zhou, Z., Lin, W., & Wu, X. F. (2016). Electrospinning ultrathin continuous cellulose acetate fibers for high-flux water filtration. *Colloids and Surfaces A: Physicochemical and Engineering Aspects, 494*, 21-29.

Zussman, E., Burman, M., Yarin, A. L., Khalfin, R., & Cohen, Y. (2006). Tensile deformation of electrospun nylon-6, 6 nanofibers. *Journal of Polymer Science Part B: Polymer Physics, 44*(10), 1482-1489.

APPENDIX A. SUPPLEMENTAL MATERIALS OF CHAPTER 3

Eqs. (3.17) to (3.35) in Chapter 3 were derived by developing a MATLAB™ code as

follow:

- Current configuration (circumferentially wrinkled):

```
% The parameters are defined as:
% R = initial radius, T = initial angle (Theta), Z = initial length,
% f(T) = disturbance function along R direction,
% g(T) = disturbance function along Z direction,
% L1 = stretch in R direction (lambda_1), L3 = stretch in Z direction
% (lambda_3),
% mu = shear modulus, G = surface tension (gamma),
% P = axial pulling load applied on the fiber.
syms R T Z f(T) g(T) L1 L3 c1 G P
r = R*(L1+f)         %current radius
t = T+g              %current angle
z = Z*L3             %current length
```

$$r = [\lambda_1 + f(\Theta)]R, \qquad \theta = \Theta + g(\Theta), \qquad z = \lambda_3 Z. \qquad (A.1)$$

- Deformation gradient matrix ($\mathbf{F}$) and the left Cauchy-Green tensor ($\mathbf{B}$):

```
drR = diff(r,R)
drT = 1/R*diff(r,T)
drZ = diff(r,Z)
dtR = r*diff(t,R)
dtT = r/R*diff(t,T)
dtZ = r*diff(t,Z)
dzR = diff(z,R)
dzT = 1/R*diff(z,T)
dzZ = diff(z,Z)
%
F = [drR drT drZ;dtR dtT dtZ;dzR dzT dzZ]
B = simplify(F*transpose(F))
```

$$\mathbf{F} = \begin{bmatrix} \dfrac{\partial r}{\partial R} & \dfrac{\partial r}{R\partial \Theta} & \dfrac{\partial r}{\partial Z} \\ \dfrac{r\partial \theta}{\partial R} & \dfrac{r\partial \theta}{R\partial \Theta} & \dfrac{r\partial \theta}{\partial Z} \\ \dfrac{\partial z}{\partial R} & \dfrac{\partial z}{R\partial \Theta} & \dfrac{\partial z}{\partial Z} \end{bmatrix} = \begin{bmatrix} \lambda_1 + f & f_\Theta & 0 \\ 0 & (\lambda_1 + f)(1+g_\Theta) & 0 \\ 0 & 0 & \lambda_3 \end{bmatrix}, \qquad (A.2)$$

$$\mathbf{B} = \mathbf{F}\mathbf{F}^T = \begin{bmatrix} (\lambda_1 + f)^2 + f_\Theta^2 & (\lambda_1 + f)(1+g_\Theta)f_\Theta & 0 \\ (\lambda_1 + f)(1+g_\Theta)f_\Theta & (\lambda_1 + f)^2(1+g_\Theta)^2 & 0 \\ 0 & 0 & \lambda_3^2 \end{bmatrix}. \qquad (A.3)$$

99

- The three scalar invariants of **B**:

```
I1 = simplify(trace(B))
I2 = simplify(1/2*((trace(B))^2-trace(B^2)))
I3 = simplify(det(B))
```

$$I_1 = \text{tr}(\mathbf{B}) = (\lambda_1 + f)^2 + f_\Theta^2 + (\lambda_1 + f)^2(1 + g_\Theta)^2 + \lambda_3^2, \tag{A.4}$$

$$I_2 = \frac{1}{2}\left[\text{tr}(\mathbf{B})^2 - \text{tr}(\mathbf{B}^2)\right] = \frac{1}{2}\left[(\lambda_1 + f)^2 + f_\Theta^2 + (\lambda_1 + f)^2(1 + g_\Theta)^2 + \lambda_3^2\right]^2$$
$$-\frac{1}{2}\left[(\lambda_1 + f)^2 + f_\Theta^2\right]^2 - \frac{1}{2}(\lambda_1 + f)^4(1 + g_\Theta)^4 - (\lambda_1 + f)^2(1 + g_\Theta)^2 f_\Theta^2 - \frac{1}{2}\lambda_3^4, \tag{A.5}$$

$$I_3 = \det(\mathbf{B}) = (\lambda_1 + f)^4(1 + g_\Theta)^2 \lambda_3^2. \tag{A.6}$$

- Incompressibility condition:

```
eqn1 = simplify(det(F)) == 1
%
syms ff ggT                                 % new symbolic variables
eqn12 = subs(eqn1,[f diff(g(T), T)],[ff ggT]);   % replacing variables
assume(L1 ~= 0 & L3 ~= 0);   % required assumption for non-trivial solution
h = simplify(solve(eqn12, ggT))
% applying the incompressibility condition L1^2*L3 = 1
h1 = simplify(subs(h, L1^2*L3, 1))
dgT = subs(h1, ff, f)
```

$$\det(\mathbf{F}) = (\lambda_1 + f)^2(1 + g_\Theta)\lambda_3 = 1, \tag{A.7}$$

$$g_\Theta = \frac{\lambda_3}{(\lambda_1 + f)^2} - 1. \tag{A.8}$$

- Strain energy density:

```
e = simplify(mu/2*(I1-3))
```

$$e = \frac{\mu}{2}(I_1 - 3) = \frac{\mu}{2}\left[(\lambda_1 + f)^2 + f_\Theta^2 + (\lambda_1 + f)^2(1 + g_\Theta)^2 + \lambda_3^2 - 3\right]. \tag{A.9}$$

- Total potential energy:

$$\Pi = \int e \, dV + \int \gamma \, dA - \int P \, d(z - Z), \tag{A.10}$$

$$\Pi = \int_Z \int_R \int_\Theta e R \, d\Theta dR dZ + \int_Z \int_\Theta \gamma \frac{R}{\lambda_1 + f} d\Theta dZ - \int_Z P(\lambda_3 - 1) dZ, \tag{A.11}$$

100

$$\Pi = \frac{1}{2} R_0^2 Z \int_\Theta e\,d\Theta + R_0 Z \int_\Theta \frac{\gamma}{\lambda_1 + f}\,d\Theta - PZ(\lambda_3 - 1)\,. \tag{A.12}$$

- Total potential energy density:

$$\frac{\partial \Pi}{\partial \Theta} = \frac{\partial}{\partial \Theta}\left[\frac{1}{2} R_0^2 Z \int_\Theta e\,d\Theta + R_0 Z \int_\Theta \frac{\gamma}{\lambda_1 + f}\,d\Theta - PZ(\lambda_3 - 1)\right], \tag{A.13}$$

$$\frac{\partial \Pi}{\partial \Theta} = \frac{1}{2} R_0^2 Z e + R_0 Z \frac{\gamma}{\lambda_1 + f}\,, \tag{A.14}$$

```
% Total potential enegry density:
L = (1/2)*Z*R^2*e+G*Z*R/(L1+f)      % PI = integral(L, dT)
LL = subs(L,diff(g(T), T),dgT)      % substituting g(T) as a function of f(T)
into L
```

$$L = \frac{\partial \Pi}{\partial \Theta} = \frac{1}{2} R_0^2 Z e + R_0 Z \frac{\gamma}{\lambda_1 + f}\,, \tag{A.15}$$

$$L = R_0^2 Z \frac{\mu}{4}\left[(\lambda_1 + f)^2 + f_\Theta^2 + \frac{\lambda_3^2}{(\lambda_1 + f)^2} + \lambda_3^2 - 3\right] + R_0 Z \frac{\gamma}{\lambda_1 + f}\,. \tag{A.16}$$

- Solving for the maximum potential energy:

```
% required assumption for non-trivial solution
assume(L1 ~= 0 & L3 ~= 0 & R ~= 0 & Z ~= 0);
% Using functional derivative with respect to f(T) instead of taking the
derivative of PI with respect to Theta to solve for the maximum potential
energy:
eqn2 = functionalDerivative(LL,f) == 0
```

$$R_0 \frac{\mu}{2}\left[1 + \lambda_3^2(\lambda_1 + f)^3 f_{\Theta\Theta} - \lambda_3^2(\lambda_1 + f)^4\right] + \gamma\lambda_3^2(f + \lambda_1) = 0\,, \tag{A.17}$$

```
% Removing higher order terms from the solution to form the final 2nd order
ODE:
for n = 2:16
    FF(1,n-1) = f^n;
end
FF(1,n) = (diff(f(T),T))^2;
FF(1,n+1) = (diff(f(T),T))^4;
FF(1,n+2) = f*diff(f(T),T,T);
SS = zeros(1,n+2);
eqn3 = simplify(simplify(subs(eqn2,FF,SS)))
```

$$R_0 \frac{\mu}{2} + \lambda_1^3 \lambda_3^2 R_0 \frac{\mu}{2}(f_{\Theta\Theta} - 4f - \lambda_1) + \gamma\lambda_3^2(\lambda_1 + f) = 0\,, \tag{A.18}$$

```
% substituting L1 = L3^(-1/2)
eqn5 = simplify(subs(eqn3,L1,L3^(-1/2)))
```

$$\lambda_3^{1/2} R_0 \frac{\mu}{2} f_{\Theta\Theta} - (4\lambda_3^{1/2} R_0 \frac{\mu}{2} - \gamma\lambda_3^2) f + \gamma\lambda_3^{3/2} = 0 \, . \tag{A.19}$$

Now a 2nd-order ODE is obtained in the form of $Af_{\Theta\Theta} + Bf + C = 0$ with considering

$f(\Theta) = A_0 \exp(ik\Theta)$ as a periodic solution to (A.19), where A_0 is the complex amplitude of

surface disturbance, and k is the wavenumber of the wrinkles. In order to determine

wavenumber k, we need to determine A and B as follow:

```
% Now we have a 2nd order ODE in the form of: A*diff(f(T),T,T)+B*f(T)+C=0
% In order to obtain the A and B coefficients from the final ODE we need to
% define a new pair of symbolic variables to use instead of diff(f(T),T,T)
% and f(T), which are symbolic functions:
syms X Y                    % new symbolic variables
eqn6 = simplify(subs(eqn5,[diff(f(T),T,T) f],[Y X]))   % replacing variables
C = equationsToMatrix(eqn6,[Y X])        % forming the matrix of coefficients
[A, B]
```

$$A = \lambda_3^{1/2} R_0 \frac{\mu}{2} \, , \tag{A.20}$$

$$B = -4\lambda_3^{1/2} R_0 \frac{\mu}{2} + \gamma\lambda_3^2 \, . \tag{A.21}$$

- Wavenumber k:

```
% Determining wave number (k = sqrt(B/A)):
k = simplify(sqrt(C(2)/C(1)))
```

$$k = \sqrt{\frac{B}{A}} = \sqrt{-4 + \frac{2\gamma\lambda_3^{3/2}}{R_0\mu}} \, . \tag{A.22}$$

```
% In order to make all the parameter dimensionless we should replace 2*G/mu
with L0, respectively. L0 is dimensionless that make the solution scalable
for different problems.
syms L0      % L0: Intrinsic Length Scale
CC = simplify(subs(C,[mu/2 G],[1 L0]))
kk = simplify(sqrt(CC(2)/CC(1)))
```

$$k = \sqrt{-4 + \frac{l_0}{R_0}\lambda_3^{3/2}} \, . \tag{A.23}$$

- MATLAB™ codes for plotting Figures 3-4 to 3-8:

```matlab
clear R_0 L0_0 L3_0 k j i SS
L3_0 = linspace(0,10,500);
R_0 = [50 100 200 500 1000];
L0_0 = [50 200 500 1000];

for k = 1:4
    for j = 1:500
        for i = 1:5
            SS(i,j,k) = L3_0(j)-
1/(L3_0(j))^2+L0_0(k)/(2*R_0(i))/sqrt(L3_0(j));
        end
    end
end

figure('units','normalized','outerposition',[0 0 1 1])
subplot(2,2,1)
plot(L3_0,SS(:,:,1),'LineWidth',2)
hold on
xline(1,'--k','$$\bf Stretch-free$$ $$\bf state$$ $$\bf (\lambda_{3} =
1)$$',...
    'Interpreter','latex','LabelOrientation','horizontal',...
    'LabelVerticalAlignment','bottom','LineWidth',1);
yline(0,'--k','LineWidth',1);
ylim([-5 15]);
ax = gca; % current axes
ax.FontSize = 14;
ax.TickLabelInterpreter = 'latex'
xlabel('$$\bf Axial$$ $$\bf stretch$$ $$\bf
\lambda_{3}$$','FontSize',16,'Interpreter','latex')
ylabel('$$\bf Axial$$ $$\bf stress$$ $$\bf
\frac{\sigma}{\mu}$$','FontSize',16,'Interpreter','latex')
text(1.3,13.65,'$$\bf R_{0}$$ $$\bf =50,$$ $$\bf 100,$$ $$\bf 200,$$ $$\bf
500,$$ $$\bf and$$ $$\bf 1,000$$ $$\bf nm$$',...
    'FontSize',12,'Interpreter','latex')
text(1.3,12.15,'$$\bf l_{0}=50$$ $$\bf
nm$$','FontSize',12,'Interpreter','latex')
text(5,2.5,'$$\bf R_{0}$$ \bf
increases','FontSize',12,'Interpreter','latex')
annotation('arrow',[0.31 0.33],[0.80
0.735],'LineWidth',1.5,'HeadStyle','vback1',...
    'HeadLength',12,'HeadWidth',12)

subplot(2,2,2)
plot(L3_0,SS(:,:,2),'LineWidth',2)
hold on
xline(1,'--k','$$\bf Stretch-free$$ $$\bf state$$ $$\bf (\lambda_{3} =
1)$$',...
    'Interpreter','latex','LabelOrientation','horizontal',...
    'LabelVerticalAlignment','bottom','LineWidth',1);
yline(0,'--k','LineWidth',1);
ylim([-5 15]);
ax = gca; % current axes
ax.FontSize = 14;
ax.TickLabelInterpreter = 'latex'
```

```matlab
xlabel('$$\bf Axial$$ $$\bf stretch$$ $$\bf
\lambda_{3}$$','FontSize',16,'Interpreter','latex')
ylabel('$$\bf Axial$$ $$\bf stress$$ $$\bf
\frac{\sigma}{\mu}$$','FontSize',16,'Interpreter','latex')
text(1.3,13.65,'$$\bf R_{0}$$ $$\bf =50,$$ $$\bf 100,$$ $$\bf 200,$$ $$\bf
500,$$ $$\bf and$$ $$\bf 1,000$$ $$\bf nm$$',...
    'FontSize',12,'Interpreter','latex')
text(1.3,12.15,'$$\bf l_{0}=200$$ $$\bf
nm$$','FontSize',12,'Interpreter','latex')
text(5,2.5,'$$\bf R_{0}$$ \bf
increases','FontSize',12,'Interpreter','latex')
annotation('arrow',[0.745 0.77],[0.81
0.735],'LineWidth',1.5,'HeadStyle','vback1',...
    'HeadLength',12,'HeadWidth',12)


subplot(2,2,3)
plot(L3_0,SS(:,:,3),'LineWidth',2)
hold on
xline(1,'--k','$$\bf Stretch-free$$ $$\bf state$$ $$\bf (\lambda_{3} =
1)$$',...
    'Interpreter','latex','LabelOrientation','horizontal',...
    'LabelVerticalAlignment','bottom','LineWidth',1);
yline(0,'--k','LineWidth',1);
ylim([-5 15]);
ax = gca; % current axes
ax.FontSize = 14;
ax.TickLabelInterpreter = 'latex'
xlabel('$$\bf Axial$$ $$\bf stretch$$ $$\bf
\lambda_{3}$$','FontSize',16,'Interpreter','latex')
ylabel('$$\bf Axial$$ $$\bf stress$$ $$\bf
\frac{\sigma}{\mu}$$','FontSize',16,'Interpreter','latex')
text(1.3,13.65,'$$\bf R_{0}$$ $$\bf =50,$$ $$\bf 100,$$ $$\bf 200,$$ $$\bf
500,$$ $$\bf and$$ $$\bf 1,000$$ $$\bf nm$$',...
    'FontSize',12,'Interpreter','latex')
text(1.3,12.15,'$$\bf l_{0}=500$$ $$\bf
nm$$','FontSize',12,'Interpreter','latex')
text(5,2.5,'$$\bf R_{0}$$ \bf
increases','FontSize',12,'Interpreter','latex')
annotation('arrow',[0.30 0.33],[0.36
0.26],'LineWidth',1.5,'HeadStyle','vback1',...
    'HeadLength',12,'HeadWidth',12)


subplot(2,2,4)
plot(L3_0,SS(:,:,4),'LineWidth',2)
hold on
xline(1,'--k','$$\bf Stretch-free$$ $$\bf state$$ $$\bf (\lambda_{3} =
1)$$',...
    'Interpreter','latex','LabelOrientation','horizontal',...
    'LabelVerticalAlignment','bottom','LineWidth',1);
yline(0,'--k','LineWidth',1);
ylim([-5 15]);
ax = gca; % current axes
ax.FontSize = 14;
ax.TickLabelInterpreter = 'latex'
xlabel('$$\bf Axial$$ $$\bf stretch$$ $$\bf
\lambda_{3}$$','FontSize',16,'Interpreter','latex')
```

```
ylabel('$$\bf Axial$$ $$\bf stress$$ $$\bf
\frac{\sigma}{\mu}$$','FontSize',16,'Interpreter','latex')
text(1.3,13.65,'$$\bf R_{0}$$ $$\bf =50,$$ $$\bf 100,$$ $$\bf 200,$$ $$\bf
500,$$ $$\bf and$$ $$\bf 1,000$$ $$\bf nm$$',...
    'FontSize',12,'Interpreter','latex')
text(1.3,12.15,'$$\bf l_{0}=1,000$$ $$\bf
nm$$','FontSize',12,'Interpreter','latex')
text(5,2.5,'$$\bf R_{0}$$ \bf
increases','FontSize',12,'Interpreter','latex')
annotation('arrow',[0.73 0.77],[0.38
0.26],'LineWidth',1.5,'HeadStyle','vback1',...
    'HeadLength',12,'HeadWidth',12)
```

- MATLAB™ codes for plotting Figures 3-8:

```
clear R0 AAA BBB Lambda_3 L3_0
CC(2);
R0 = linspace(50,1000,100);
L0_0 = [50 200 500 1000];
for i = 1:4
    for j = 1:length(R0)
        BBB(i,j) = vpa(subs(CC(2),[L0 R],[L0_0(i) R0(j)]));
        AAA(i,j) = vpa(subs(CC(1),R,R0(j)));
        Lambda_3(i,j) = vpasolve(BBB(i,j)/AAA(i,j) == 2^2, L3, [0.2 Inf]);
    end
end
figure
plot(R0,Lambda_3,'LineWidth',2)
xlim([0 1000])
ylim([0 30])
yline(1,'--k','$$\bf Stretch-free$$ $$\bf state$$ $$\bf (\lambda_{3} =
1)$$',...
    'Interpreter','latex','LabelVerticalAlignment','middle','LineWidth',1);

ax = gca; % current axes
ax.FontSize = 14;
ax.TickLabelInterpreter = 'latex'
xlabel('$$\bf Fiber$$ $$\bf radius$$ $$\bf R_{0}$$ $$\bf
(nm)$$','FontSize',16,'Interpreter','latex')
ylabel('$$\bf Critical$$ $$\bf axial$$ $$\bf stretch$$ $$\bf
\lambda_{3}$$','FontSize',16,'Interpreter','latex')
text(30,28,'$$\bf l_{0}=50,$$ $$\bf 200,$$ $$\bf 500,$$ $$\bf and$$ $$\bf
1,000$$ $$\bf nm$$',...
    'FontSize',12,'Interpreter','latex')
text(200,18,'$$\bf l_{0}$$ \bf
decreases','FontSize',12,'Interpreter','latex')
annotation('arrow',[0.5 0.38],[0.15
0.57],'LineWidth',1.5,'HeadStyle','vback1',...
    'HeadLength',12,'HeadWidth',12)
```

- MATLAB™ codes for plotting Figures 3-9 to 3-12:

```
clear R_0 L0_0 L3_0 k1 i
L0_0 = [50 200 500 1000];              % [nm]
L3_0 = linspace(0,20,100);
```

```matlab
k1 = zeros(1,length(L3_0));
j = 0;
for R_0 = [50 100 200 500 1000];        % [nm]
    j = j+1;
for i = 1:length(L3_0)
    k1(j,i) = vpa(subs(kk,[R L3 L0],[R_0 L3_0(i) L0_0(1)]));
end
end

k2 = zeros(1,length(L3_0));
j = 0;
for R_0 = [50 100 200 500 1000];        % [nm]
    j = j+1;
for i = 1:length(L3_0)
    k2(j,i) = vpa(subs(kk,[R L3 L0],[R_0 L3_0(i) L0_0(2)]));
end
end

k3 = zeros(1,length(L3_0));
j = 0;
for R_0 = [50 100 200 500 1000];        % [nm]
    j = j+1;
for i = 1:length(L3_0)
    k3(j,i) = vpa(subs(kk,[R L3 L0],[R_0 L3_0(i) L0_0(3)]));
end
end

k4 = zeros(1,length(L3_0));
j = 0;
for R_0 = [50 100 200 500 1000];        % [nm]
    j = j+1;
for i = 1:length(L3_0)
    k4(j,i) = vpa(subs(kk,[R L3 L0],[R_0 L3_0(i) L0_0(4)]));
end
end

figure('units','normalized','outerposition',[0 0 1 1])

subplot(2,2,1)
plot(L3_0,k1,'LineWidth',2)
hold on
ylim([0 10])
yticks([0 2 4 6 8 10])
xline(1,'--k','$$\bf Stretch-free$$ $$\bf state$$ $$\bf (\lambda_{3} =
1)$$',...
    'Interpreter','latex','LabelHorizontalAlignment','center',...
    'LabelVerticalAlignment','middle','LineWidth',1);
yline(2,'--k','$$\bf Elliptic$$ $$\bf wrinkle$$ $$\bf (k = 2)$$',...

'Interpreter','latex','LabelHorizontalAlignment','center','LabelVerticalAlig
nment','middle','LineWidth',1);
ax = gca; % current axes
ax.FontSize = 14;
ax.TickLabelInterpreter = 'latex'
```

```matlab
xlabel('$$\bf Axial$$ $$\bf stretch$$ $$\bf
\lambda_{3}$$','FontSize',16,'Interpreter','latex')
ylabel('$$\bf Wavenumber$$ $$\bf k$$','FontSize',16,'Interpreter','latex')
text(1.5,9.3,'$$\bf R_{0}$$ $$\bf =50,$$ $$\bf 100,$$ $$\bf 200,$$ $$\bf
500,$$ $$\bf and$$ $$\bf 1,000$$ $$\bf nm$$',...
    'FontSize',12,'Interpreter','latex')
text(1.5,8.5,'$$\bf l_{0}=50$$ $$\bf
nm$$','FontSize',12,'Interpreter','latex')
text(4,6,'$$\bf R_{0}$$ \bf decreases','FontSize',12,'Interpreter','latex')
annotation('arrow',[0.45 0.25],[0.59
0.77],'LineWidth',1.5,'HeadStyle','vback1',...
    'HeadLength',12,'HeadWidth',12)


subplot(2,2,2)
plot(L3_0,k2,'LineWidth',2)
hold on
ylim([0 20])
yticks([0 5 10 15 20])
xline(1,'--k','$$\bf Stretch-free$$ $$\bf state$$ $$\bf (\lambda_{3} =
1)$$',...
    'Interpreter','latex','LabelHorizontalAlignment','center',...
    'LabelVerticalAlignment','middle','LineWidth',1);
yline(2,'--k','$$\bf Elliptic$$ $$\bf wrinkle$$ $$\bf (k = 2)$$',...
    'Interpreter','latex','LabelVerticalAlignment','middle','LineWidth',1);
ax = gca; % current axes
ax.FontSize = 14;
ax.TickLabelInterpreter = 'latex'
xlabel('$$\bf Axial$$ $$\bf stretch$$ $$\bf
\lambda_{3}$$','FontSize',16,'Interpreter','latex')
ylabel('$$\bf Wavenumber$$ $$\bf k$$','FontSize',16,'Interpreter','latex')
text(1.5,18.6,'$$\bf R_{0}$$ $$\bf =50,$$ $$\bf 100,$$ $$\bf 200,$$ $$\bf
500,$$ $$\bf and$$ $$\bf 1,000$$ $$\bf nm$$',...
    'FontSize',12,'Interpreter','latex')
text(1.5,17,'$$\bf l_{0}=200$$ $$\bf
nm$$','FontSize',12,'Interpreter','latex')
text(4,12,'$$\bf R_{0}$$ \bf decreases','FontSize',12,'Interpreter','latex')
annotation('arrow',[0.75 0.68],[0.6
0.77],'LineWidth',1.5,'HeadStyle','vback1',...
    'HeadLength',12,'HeadWidth',12)


subplot(2,2,3)
plot(L3_0,k3,'LineWidth',2)
hold on
ylim([0 30])
yticks([0 5 10 15 20 25 30])
xline(1,'--k','$$\bf Stretch-free$$ $$\bf state$$ $$\bf (\lambda_{3} =
1)$$',...
    'Interpreter','latex','LabelHorizontalAlignment','center',...
    'LabelVerticalAlignment','middle','LineWidth',1);
yline(2,'--k','$$\bf Elliptic$$ $$\bf wrinkle$$ $$\bf (k = 2)$$',...
    'Interpreter','latex','LabelVerticalAlignment','middle','LineWidth',1);
ax = gca; % current axes
ax.FontSize = 14;
ax.TickLabelInterpreter = 'latex'
xlabel('$$\bf Axial$$ $$\bf stretch$$ $$\bf
\lambda_{3}$$','FontSize',16,'Interpreter','latex')
```

```matlab
ylabel('$$\bf Wavenumber$$ $$\bf k$$','FontSize',16,'Interpreter','latex')
text(1.5,27.9,'$$\bf R_{0}$$ $$\bf =50,$$ $$\bf 100,$$ $$\bf 200,$$ $$\bf
500,$$ $$\bf and$$ $$\bf 1,000$$ $$\bf nm$$',...
    'FontSize',12,'Interpreter','latex')
text(1.5,25.5,'$$\bf l_{0}=500$$ $$\bf
nm$$','FontSize',12,'Interpreter','latex')
text(4,18,'$$\bf R_{0}$$ \bf decreases','FontSize',12,'Interpreter','latex')
annotation('arrow',[0.3 0.24],[0.13
0.297],'LineWidth',1.5,'HeadStyle','vback1',...
    'HeadLength',12,'HeadWidth',12)


subplot(2,2,4)
plot(L3_0,k4,'LineWidth',2)
hold on
ylim([0 50])
yticks([0 10 20 30 40 50])
xline(1,'--k','$$\bf Stretch-free$$ $$\bf state$$ $$\bf (\lambda_{3} =
1)$$',...
    'Interpreter','latex','LabelHorizontalAlignment','center',...
    'LabelVerticalAlignment','middle','LineWidth',1);
yline(2,'--k','$$\bf Elliptic$$ $$\bf wrinkle$$ $$\bf (k = 2)$$',...
    'Interpreter','latex','LabelVerticalAlignment','middle','LineWidth',1);
ax = gca; % current axes
ax.FontSize = 14;
ax.TickLabelInterpreter = 'latex'
xlabel('$$\bf Axial$$ $$\bf stretch$$ $$\bf
\lambda_{3}$$','FontSize',16,'Interpreter','latex')
ylabel('$$\bf Wavenumber$$ $$\bf k$$','FontSize',16,'Interpreter','latex')
text(1.5,46.5,'$$\bf R_{0}$$ $$\bf =50,$$ $$\bf 100,$$ $$\bf 200,$$ $$\bf
500,$$ $$\bf and$$ $$\bf 1,000$$ $$\bf nm$$',...
    'FontSize',12,'Interpreter','latex')
text(1.5,42.5,'$$\bf l_{0}=1,000$$ $$\bf
nm$$','FontSize',12,'Interpreter','latex')
text(4,30,'$$\bf R_{0}$$ \bf decreases','FontSize',12,'Interpreter','latex')
annotation('arrow',[0.75 0.68],[0.13
0.297],'LineWidth',1.5,'HeadStyle','vback1',...
    'HeadLength',12,'HeadWidth',12)
```

APPENDIX B. SUPPLEMENTAL MATERIALS OF CHAPTER 4

In Chapter 4, in addition to the three a/c aspect ratios of 0.25, 0.5, and 0.75, the case with a/c ratio of zero is also considered, i.e., the fiber is produced via regular electrospinning process without a hard core.
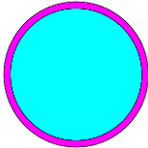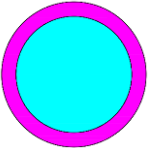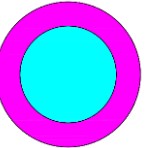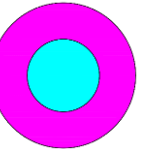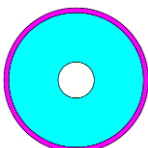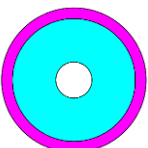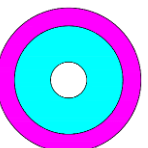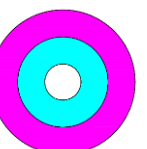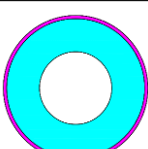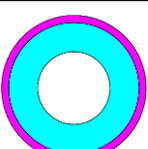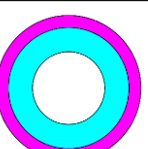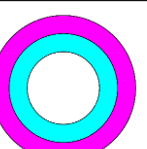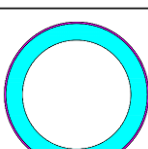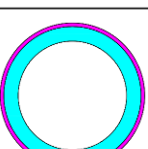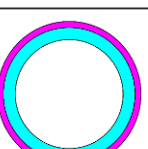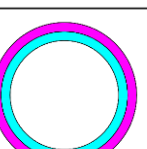
a/c	t_f/t_s			
	0.1	0.25	0.5	1
0				
0.25				
0.5				
0.75				

Figure B-1. Schematic cross-section geometries of the electrospun core-shell fibers of varying aspect ratios a/c and t_f/t_s used in computational wrinkling analysis.

As the additional information, for the cases with $a/c = 0$, below show the critical surface wrinkle mode charts and the variation of the critical wrinkling strain ε_c with respect to the wavenumber n of the surface wrinkle modes.
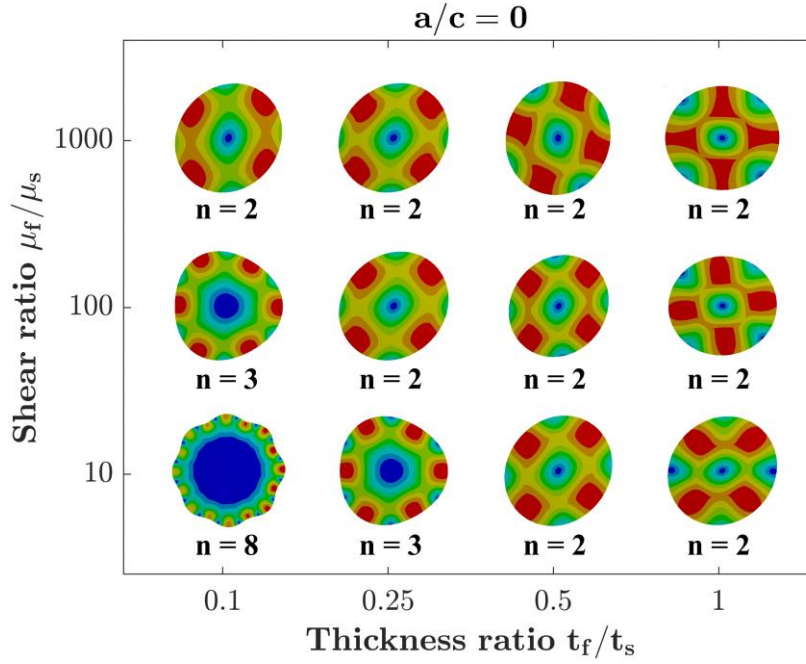
Figure B-2. Critical surface wrinkle mode charts in terms of the wavenumber n and surface topology against the aspect ratio t_f/t_s and stiffness ratio μ_f/μ_s for $a/c = 0$.
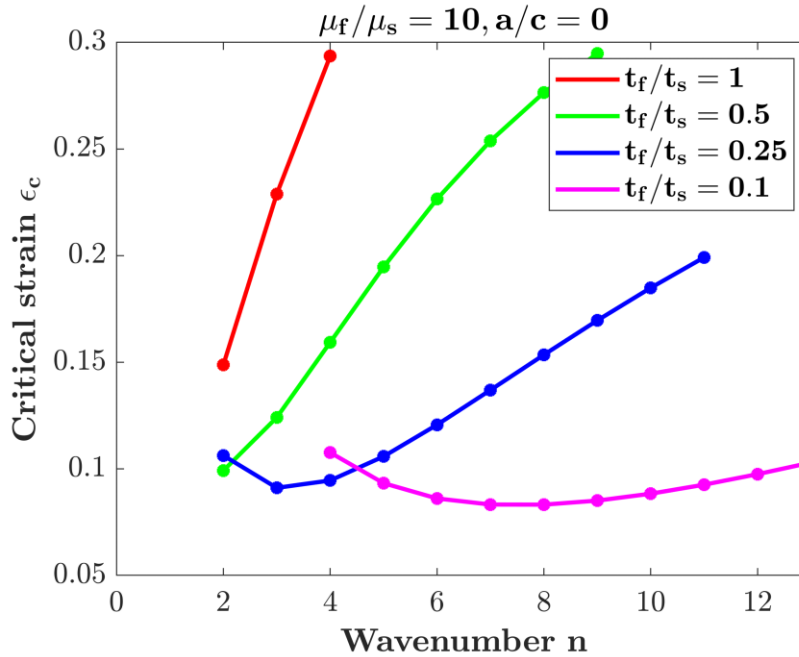
Figure B-3. Variation of the critical wrinkling strain ε_c with respect to the wavenumber n of the surface wrinkle modes at varying aspect ratios t_f/t_s for $a/c = 0$ and $\mu_f/\mu_s = 10$.
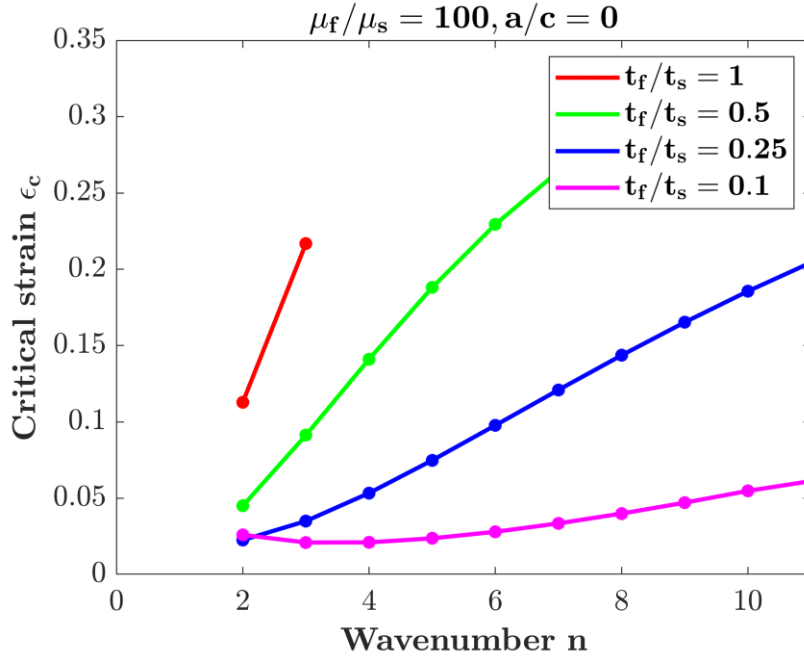
Figure B-4. Variation of the critical wrinkling strain ε_c with respect to the wavenumber n of the surface wrinkle modes at varying aspect ratios t_f/t_s for $a/c = 0$ and $\mu_f/\mu_s = 100$.
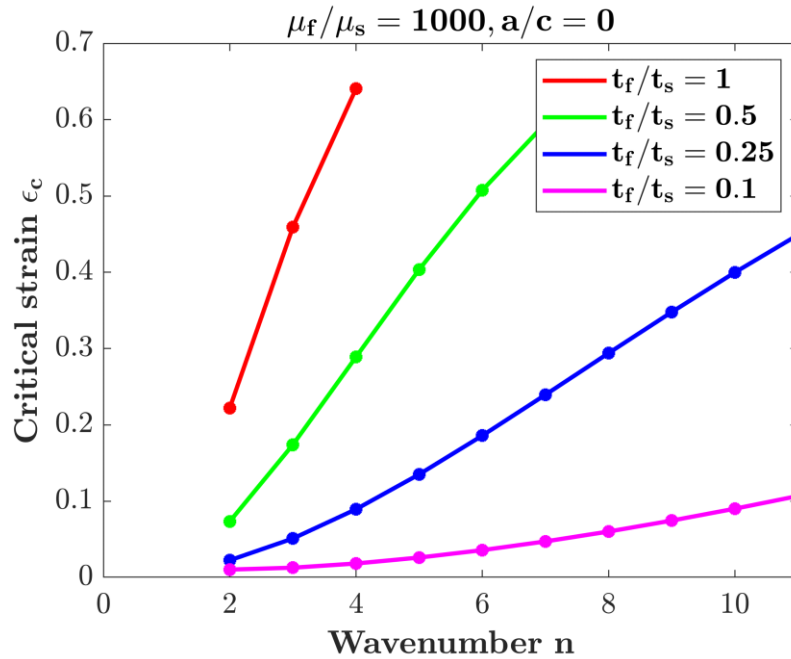
Figure B-5. Variation of the critical wrinkling strain ε_c with respect to the wavenumber n of the surface wrinkle modes at varying aspect ratios t_f/t_s for $a/c = 0$ and $\mu_f/\mu_s = 1,000$.

APPENDIX C. SUPPLEMENTAL MATERIALS OF CHAPTER 5

Eqs. (5.1) to (5.19) were derived by developing a MATLAB™ code as follow:

Radial and circumferential stretches of the hydrogels:

$$\lambda_r = \frac{dr}{dR},$$
(C.1)

$$\lambda_\theta = \frac{r}{R}.$$
(C.2)

- Deformation gradient matrix ($\mathbf{F}$), left Cauchy-Green tensor ($\mathbf{B}$) and three principal scalar invariants:

```
syms R T r(R) L_r L_t v C N kT X S_r S_t

F = [L_r 0 0;0 L_t 0;0 0 L_t]
B = simplify(F*transpose(F))
I1 = simplify(trace(B))
I2 = simplify(1/2*((trace(B))^2-trace(B^2)))
I3 = simplify(det(B))
```

$$\mathbf{F} = \begin{bmatrix} \dfrac{\partial r}{\partial R} & \dfrac{\partial r}{R\partial \Theta} & \dfrac{\partial r}{R\partial \Phi} \\ \dfrac{r\partial \theta}{\partial R} & \dfrac{r\partial \theta}{R\partial \Theta} & \dfrac{r\partial \theta}{R\partial \Phi} \\ \dfrac{r\partial \phi}{\partial R} & \dfrac{r\partial \phi}{R\partial \Theta} & \dfrac{r\partial \phi}{R\partial \Phi} \end{bmatrix} = \begin{bmatrix} \lambda_r & 0 & 0 \\ 0 & \lambda_\theta & 0 \\ 0 & 0 & \lambda_\theta \end{bmatrix},$$
(C.3)

$$\mathbf{B} = \mathbf{F}\mathbf{F}^T = \begin{bmatrix} \lambda_r^2 & 0 & 0 \\ 0 & \lambda_\theta^2 & 0 \\ 0 & 0 & \lambda_\theta^2 \end{bmatrix},$$
(C.4)

$$I_1 = \text{tr}(\mathbf{B}) = \lambda_r^2 + 2\lambda_\theta^2,$$
(C.5)

$$I_2 = \frac{1}{2}\left[\text{tr}(\mathbf{B})^2 - \text{tr}(\mathbf{B}^2)\right] = 2\lambda_r^2\lambda_\theta^2 + \lambda_\theta^4,$$
(C.6)

$$I_3 = \det(\text{B}) = \lambda_r^2\lambda_\theta^4.$$
(C.7)

- The molecular incompressibility condition:

```
eqn1 = simplify(det(F)) == 1+v*C
syms dF vC                    % new symbolic variables
eqn12 = subs(eqn1,[det(F) v*C],[dF vC]);        % replacing variables
h = simplify(solve(eqn12, vC))
vC = subs(h, dF, det(F))
```

$$\det(\mathbf{F}) = \lambda_\theta^2 \lambda_r = 1 + vC, \tag{C.8}$$

$$vC = \lambda_\theta^2 \lambda_r - 1. \tag{C.9}$$

- The Flory and Rehner (1943) free-energy density function for a swollen elastomer:

```
W_s = 0.5*N*kT*(I1-3-2*log(det(F)))
W_m = -(kT/v)*(v*C*log(1+1/(v*C))+X/(1+v*C))
% W = W_s+W_m
```

$$W_s(\mathbf{F}) = \frac{1}{2} NkT \left[I_1 - 3 - 2\log\left(\det(\mathbf{F})\right) \right], \tag{C.10}$$

$$W_m(C) = -\frac{kT}{v} \left[vC \log\left(1 + \frac{1}{vC}\right) + \frac{\chi}{1 + vC} \right], \tag{C.11}$$

$$W(\mathbf{F}, C) = W_s(\mathbf{F}) + W_m(C), \tag{C.12a}$$

$$W(\mathbf{F}, C) = \frac{1}{2} NkT \left[I_1 - 3 - 2\log\left(\det(\mathbf{F})\right) \right] - \frac{kT}{v} \left[vC \log\left(1 + \frac{1}{vC}\right) + \frac{\chi}{1 + vC} \right], \tag{C.12b}$$

- Nominal stresses and chemical potential:

$$s_r = \frac{\partial W(\mathbf{F}, C)}{\partial \lambda_r} - \Pi \frac{\partial \det(\mathbf{F})}{\partial \lambda_r}, \tag{C.13}$$

$$s_\theta = \frac{\partial W(\mathbf{F}, C)}{\partial \lambda_\theta} - \Pi \frac{\partial \det(\mathbf{F})}{\partial \lambda_\theta}, \tag{C.14}$$

$$\mu = \frac{\partial W(F, C)}{\partial C} + \Pi v, \tag{C.15}$$

- Equations of state for gel model:

```
S_r = simplify(diff(W_s,L_r)+(1/v)*diff(W_m,C)*diff(det(F),L_r))
S_t = simplify((diff(W_s,L_t)+(1/v)*diff(W_m,C)*diff(det(F),L_t))/2)
```

113

$$\frac{s_r}{NkT} = \lambda_r - \lambda_r^{-1} + \frac{\lambda_\theta^2}{vN}\left[\log\frac{vC}{1+vC} + \frac{1}{1+vC} + \frac{\chi}{(1+vC)^2}\right], \quad \text{(C.16)}$$

$$\frac{s_\theta}{NkT} = \lambda_\theta - \lambda_\theta^{-1} + \frac{\lambda_\theta\lambda_r}{vN}\left[\log\frac{vC}{1+vC} + \frac{1}{1+vC} + \frac{\chi}{(1+vC)^2}\right]. \quad \text{(C.17)}$$

- Nonlinear 2nd-order ODE governing equation:

```
S_r = simplify(subs(S_r,[v*C],[vC]))
S_t = simplify(subs(S_t,[v*C],[vC]))
SS_r = simplify(subs(S_r,[L_r L_t L_t],[diff(r(R),R) r/R r/R]))
SS_t = simplify(subs(S_t,[L_r L_t L_t],[diff(r(R),R) r/R r/R]))
%%
assume(v ~= 0 & kT ~= 0);
eqn21 = diff(SS_r,R)+2*(SS_r-SS_t)/R == 0
eqn22 = diff(SS_t,T)  == 0
```

$$\frac{d^2r}{dR^2} - \frac{d}{dR}\left(\frac{dR}{dr}\right) + \frac{1}{vN}\frac{d}{dR}\left(\frac{r^2}{R^2}\left[\log\left(1-\frac{R^2}{r^2}\frac{dR}{dr}\right) + \frac{R^2}{r^2}\frac{dR}{dr} + \chi\left(\frac{R^2}{r^2}\frac{dR}{dr}\right)^2\right]\right) +$$
$$\frac{2}{R}\left\{\frac{dr}{dR} - \frac{dR}{dr} - \frac{r}{R} + \frac{R}{r} + \frac{1}{vN}\left(\frac{r^2}{R^2} - \frac{r}{R}\frac{dr}{dR}\right)\left[\log\left(1-\frac{R^2}{r^2}\frac{dR}{dr}\right) + \frac{R^2}{r^2}\frac{dR}{dr} + \chi\left(\frac{R^2}{r^2}\frac{dR}{dr}\right)^2\right]\right\} = 0 \quad \text{.(C.18)}$$

Now solving (C.19) for $\dfrac{d^2r}{dR^2}$, determines $r'' = f(R, r, r')$ that will be used in the shooting

method to calculate r and r'. By having r and r', s_r and s_θ can be easily calculated.

```
syms r1 r2 dr2
SS_r12 = simplify(subs(SS_r, [r diff(r(R),R)], [r1 r2]))
SS_t12 = simplify(subs(SS_t, [r diff(r(R),R)], [r1 r2]))
eqn31 = simplify(subs(eqn21, [r diff(r(R),R) diff(r(R),R,R)], [r1 r2 dr2]))
%%
h = simplify(solve(eqn31, dr2))
dr2 = h
```

$$\frac{d^2r}{dR^2} = \frac{2r_2(r_1-Rr_2)(2R^5\chi + R^3r_1^2r_2 - 2R^3\chi r_1^2r_2 + Nr_1^5r_2^3v - NR^3r_1^2r_2v + NRr_1^4r_2^2v - NR^2r_1^3r_2^2v)}{R^4r_1^3r_2 + 2R^6\chi r_1 - 2R^4\chi r_1^3r_2 - NR^4r_1^3r_2v + NR^2r_1^5r_2^2v - NR^4r_1^3r_2^3v + NR^2r_1^5r_2^4v} . \quad \text{(C.19)}$$

- Shooting Method:

For $y'' = f(x, y, y')$ with $A \le x \le B$ and $y(A) = \lambda_0 A$, in order to calculate y and y', it is assumed that $y'(A) = Y$. Since the hydrogel swells freely on the outer edge, the radial nominal stress on the outer radius is

$$s_r[y(B, Y_k), y'(B, Y_k)] = 0, \tag{C.20}$$

where Y_k for $k \ge 1$ is calculated as

$$Y_k = Y_{k-1} - \frac{s_r[y(B, Y_{k-1}), y'(B, Y_{k-1})]}{\dfrac{\partial s_r(B, Y_{k-1})}{\partial y} \times z(B, Y_{k-1}) + \dfrac{\partial s_r(B, Y_{k-1})}{\partial y'} \times z'(B, Y_{k-1})}, \tag{C.21}$$

where $z = \dfrac{\partial y}{\partial Y}$ and $z' = \dfrac{\partial y'}{\partial Y}$. And Y_k for $k = 0$ is calculated as

$$Y_0 = y'(A) \approx \frac{y(B) - y(A)}{B - A} = Y. \tag{C.22}$$

For the initial values for z and z', consider the following conditions

$$z(A) = \frac{\partial y}{\partial Y}\bigg|_A = \frac{\partial(\lambda_0 A)}{\partial Y} = 0, \tag{C.23}$$

$$z'(A) = \frac{\partial y'}{\partial Y}\bigg|_A = \frac{\partial Y}{\partial Y} = 1. \tag{C.24}$$

With the initial conditions $y(A, Y) = \lambda_0 A$, $y'(A, Y) = Y_k$, $z(A, Y) = 0$, and $z'(A, Y) = 1$, the shooting method is capable of determining $y(B, Y)$, $y'(B, Y)$, $z(B, Y)$, and $z'(B, Y)$:

$$\begin{cases} u_1 = y \\ u_2 = y' \\ u_3 = z \\ u_4 = z' \end{cases} \rightarrow \begin{cases} u_1' = u_2 = y' \\ u_2' = y'' = f(x, y, y') \\ u_3' = u_4 = z' \\ u_4' = z'' = f_y z + f_{y'} z' \end{cases}. \tag{C.25}$$

where $f_y = \dfrac{\partial f(x, y, y')}{\partial y}$ and $f_{y'} = \dfrac{\partial f(x, y, y')}{\partial y'}$.

115

- MATLAB™ codes for plotting Figures 5-2 to 5-5:

```matlab
close all
clear all
clc

A = 1;
B = 2;
C = 3;
L_0 = 1.077;
vN10 = [1E-4 1E-3 1E-3];
vN20 = [1E-3 1E-3 1E-4];
X10 = [0.1 0.2 0.2];
X20 = [0.2 0.2 0.1];

str1 = [-4,-3,-3];
str2 = [-3,-3,-4];
str3 = ["Inner gel is softer than outer gel" "Inner and outer gels are same"
"Outer gel is softer than inner gel"];

Y0 = [10 10 10];
dy_0 = [0.1 0.1 0.1];
ddy_0 = [1E-2 1E-2 1E-2];

figure('units','normalized','outerposition',[0 0 1 1])

for k = 1:3
    vN1 = vN10(k);
    vN2 = vN20(k);
    X1 = X10(k);
    X2 = X20(k);

    Y(1) = Y0(k);

    S_r_C = inf;
    J = 0;
    j = 0;
    dy0 = dy_0(k);
    while abs(S_r_C) > 1E-6
        J = J+1;
        j = j+1;
        if abs(imag(S_r_C)) > 0 || j > 50 && abs(S_r_C) > 1E3 || j > 400 &&
abs(S_r_C) > 1E0
            dy0 = dy0+ddy_0(k);
            Y(1) = Y0(k);
            j = 1;
        end
        if J > 1E4
            break
        end
        % initial values
        y1(1) = L_0;
        dy1(1) = Y(j);
        z1(1) = 0;
```

116

```matlab
        dz1(1) = 1;
        u0 = [y1(1); dy1(1); z1(1); dz1(1)];
        [R1,u1] = ode45(@(R1,u1) odefun(R1,u1,vN1,X1),[A B],u0);
        y1 = u1(:,1);
        dy1 = u1(:,2);
        z1 = u1(:,3);
        dz1 = u1(:,4);
        n1 = length(R1);
        clear S_r1 S_t1
        for i = 1:n1
            S_r1(i,1) = fun_Sr(R1(i),y1(i),dy1(i),vN1,X1);
            S_t1(i,1) = fun_St(R1(i),y1(i),dy1(i),vN1,X1);
        end
        y2(1) = y1(n1);
        z2(1) = z1(n1);
        dz2(1) = dz1(n1);
        syms dy
        eqn = @(dy) S_r1(n1)-fun_Sr(B,y2(1),dy,vN2,X2);

        dy2(1) = fsolve(eqn,dy0);
        u0 = [y2(1); dy2(1); z2(1); dz2(1)];
        [R2,u2] = ode45(@(R2,u2) odefun(R2,u2,vN2,X2),[B C],double(u0));
        y2 = u2(:,1);
        dy2 = u2(:,2);
        z2 = u2(:,3);
        dz2 = u2(:,4);
        n2 = length(R2);
        clear S_r2 S_t2
        for i = 1:n2
            S_r2(i,1) = fun_Sr(R2(i),y2(i),dy2(i),vN2,X2);
            S_t2(i,1) = fun_St(R2(i),y2(i),dy2(i),vN2,X2);
        end
        S_r_C = S_r2(n2);
        [dSr_y2, dSr_dy2] = fun_dSr(R2(n2),y2(n2),dy2(n2),vN2,X2);
        Y(j+1) = real(Y(j)-S_r_C/(dSr_y2*z2(n2)+dSr_dy2*dz2(n2)));
        [dSr_y2B, dSr_dy2B] = fun_dSr(R2(1),y2(1),dy2(1),vN2,X2);
        ddy0 = (S_r1(n1)-S_r2(1))/(dSr_y2B*z2(1)+dSr_dy2B*dz2(1));
        [S_r_C dy0 j]
    end
%%
r1 = y1;
r2 = y2;
L_r1 = dy1;
L_r2 = dy2;
L_t1 = r1./R1;
L_t2 = r2./R2;
vC1 = ((L_t1.^2).*L_r1)-1;
vC2 = ((L_t2.^2).*L_r2)-1;
%%
syms L1 L2
eqn1 = @(L1) L1-1/L1+(L1^2/vN1)*(log((L1^3-1)/L1^3)+1/L1^3+X1/L1^6);
L1_free = double(bisection(eqn1,1,100));
vC1_free = L1_free^3-1;
eqn2 = @(L2) L2-1/L2+(L2^2/vN2)*(log((L2^3-1)/L2^3)+1/L2^3+X2/L2^6);
L2_free = double(bisection(eqn2,1,100));
vC2_free = L2_free^3-1;
```

117

```matlab
    %%
    color = [1 0 0;0 0.7 0;0 0 1];          % red green blue


    subplot(2,2,1); hold on; box on;
    P_r1(k) = plot([R1;R2], [r1;r2],'Color',color(k,:),'LineWidth',1.5);
    legendInfo{k} = str3(k);
    xline(B,':k','LineWidth',0.75);
    xlim([A,C]); ylim([0 15]); yticks(0:3:15);
    xlabel('R/A','FontSize',16,'Interpreter','latex');
ylabel('r(R)','FontSize',16,'Interpreter','latex');

legend([P_r1],legendInfo,'location','northwest','FontSize',14,'Interpreter',
'latex');
    ax = gca; % current axes
    ax.FontSize = 14;
    ax.TickLabelInterpreter = 'latex'

    subplot(2,2,2); hold on; box on;
    plot(R1, vC1,'Color',color(k,:),'LineWidth',1.5);
    xline(B,':k','LineWidth',0.75);
    plot(R2, vC2,'Color',color(k,:),'LineWidth',1.5);
    xlim([A,C]); ylim([0 150]); yticks(0:30:150);
    xlabel('R/A','FontSize',16,'Interpreter','latex');
ylabel('vC','FontSize',16,'Interpreter','latex');
    ax = gca; % current axes
    ax.FontSize = 14;
    ax.TickLabelInterpreter = 'latex'

    subplot(2,2,3); hold on; box on;
    plot(R1, L_r1,'Color',color(k,:),'LineWidth',1.5);
    plot(R1, L_t1,'Color',color(k,:),'LineStyle','--','LineWidth',1.5);
    xline(B,':k','LineWidth',0.75);
    plot(R2, L_r2,'Color',color(k,:),'LineWidth',1.5);
    plot(R2, L_t2,'Color',color(k,:),'LineStyle','--','LineWidth',1.5);
    xlim([A,C]); ylim([0 12]); yticks(0:2:12)
    xlabel('R/A','FontSize',16,'Interpreter','latex');
ylabel('$$\lambda$$','FontSize',16,'Interpreter','latex');
    P_Lr = plot(nan,nan,'k-','LineWidth',1.5);
    P_Lt = plot(nan,nan,'k--','LineWidth',1.5);
    legend([P_Lr P_Lt],'$$\bf \lambda_{r}$$','$$\bf
\lambda_{\theta}$$','FontSize',14,'Interpreter','latex')
    ax = gca; % current axes
    ax.FontSize = 14;
    ax.TickLabelInterpreter = 'latex'

    subplot(2,2,4); hold on; box on;
    plot(R1, S_r1,'Color',color(k,:),'LineWidth',1.5);
    plot(R1, S_t1,'Color',color(k,:),'LineStyle','--','LineWidth',1.5);
    xline(B,':k','LineWidth',0.75); yline(0,'-.k','LineWidth',0.75);
    plot(R2, S_r2,'Color',color(k,:),'LineWidth',1.5);
    plot(R2, S_t2,'Color',color(k,:),'LineStyle','--','LineWidth',1.5);
    xlim([A,C]); ylim([-20 10]); yticks([-20 -15 -10 -5 0 5 10])
    xlabel('R/A','FontSize',16,'Interpreter','latex');
ylabel('s/NkT','FontSize',16,'Interpreter','latex');
    P_Sr = plot(nan,nan,'k-','LineWidth',1.5);
```

```matlab
    P_St = plot(nan,nan,'k--','LineWidth',1.5);
    legend([P_Sr  P_St],'$$\bf s_{r}$$','$$\bf
s_{\theta}$$','Location','southeast','FontSize',14,'Interpreter','latex' )
    ax = gca; % current axes
    ax.FontSize = 14;
    ax.TickLabelInterpreter = 'latex'
end
%%
subplot(2,2,2);
txt = {{'$$\bf vN_{I} = 10^{-4}$$'; '$$\bf \chi_{I} = 0.1$$'},...
    {'$$\bf vN_{I} = 10^{-3}$$'; '$$\bf \chi_{I} = 0.2$$'},...
    {'$$\bf vN_{II} = 10^{-3}$$'; '$$\bf \chi_{II} = 0.2$$'},...
    {'$$\bf vN_{II} = 10^{-4}$$'; '$$\bf \chi_{II} = 0.1$$'}};
text([1.4 1.8 1.8 2.5 2.5], [100 70 30.5 35 125], [txt(1) txt(2) txt(2)
txt(3) txt(4)], 'HorizontalAlignment', 'center', 'BackgroundColor', 'w',
'EdgeColor', 'k', 'FontSize', 10, 'Interpreter','latex');
%%
function du = odefun(R,u,vN,X)
du = zeros(4,1);
du(1) = u(2);
du(2) = fun_d2y(R, u(1), u(2), vN, X);
du(3) = u(4);
du(4) = fun_d2z(R, u(1), u(2), u(3), u(4), vN, X);
end
function d2y = fun_d2y(R,y,dy,vN,X)
d2y = (2.0*dy*(y - R*dy)*(2.0*R^5*X + R^3*dy*y^2 + dy^3*vN*y^5 -
1.0*R^2*dy^2*vN*y^3 - 2.0*R^3*X*dy*y^2 - 1.0*R^3*dy*vN*y^2 +
R*dy^2*vN*y^4))/(R^4*dy*y^3 + 2.0*R^6*X*y + R^2*dy^2*vN*y^5 -
1.0*R^4*dy^3*vN*y^3 + R^2*dy^4*vN*y^5 - 2.0*R^4*X*dy*y^3 -
1.0*R^4*dy*vN*y^3);
end
function d2z = fun_d2z(R,y,dy,z,dz,vN,X)
F_y = (2.0*dy^2*(4.0*R^10*X^2 - 8.0*R^8*X^2*dy*y^2 - 6.0*R^8*X*dy^3*vN*y^2 -
4.0*R^8*X*dy*vN*y^2 + 4.0*R^8*X*dy*y^2 + 8.0*R^7*X*dy^2*vN*y^3 +
4.0*R^6*X^2*dy^2*y^4 + 12.0*R^6*X*dy^4*vN*y^4 + 8.0*R^6*X*dy^2*vN*y^4 -
4.0*R^6*X*dy^2*y^4 - 6.0*R^6*X*dy*vN*y^4 + R^6*dy^4*vN^2*y^4 -
1.0*R^6*dy^4*vN*y^4 + R^6*dy^2*vN^2*y^4 - 2.0*R^6*dy^2*vN*y^4 + R^6*dy^2*y^4
- 16.0*R^5*X*dy^3*vN*y^5 - 6.0*R^4*X*dy^5*vN*y^6 - 4.0*R^4*X*dy^3*vN*y^6 +
12.0*R^4*X*dy^2*vN*y^6 - 2.0*R^4*dy^5*vN^2*y^6 + 3.0*R^4*dy^5*vN*y^6 +
R^4*dy^4*vN^2*y^6 - 2.0*R^4*dy^3*vN^2*y^6 + 2.0*R^4*dy^3*vN*y^6 +
R^4*dy^2*vN^2*y^6 - 1.0*R^4*dy^2*vN*y^6 + 8.0*R^3*X*dy^4*vN*y^7 -
4.0*R^3*dy^4*vN*y^7 - 6.0*R^2*X*dy^3*vN*y^8 + R^2*dy^6*vN^2*y^8 -
2.0*R^2*dy^5*vN^2*y^8 + R^2*dy^4*vN^2*y^8 - 2.0*R^2*dy^3*vN^2*y^8 +
3.0*R^2*dy^3*vN*y^8 + dy^6*vN^2*y^10 + dy^4*vN^2*y^10))/(R^2*y^2*(2.0*R^4*X
+ R^2*dy*y^2 + dy^2*vN*y^4 + dy^4*vN*y^4 - 1.0*R^2*dy^3*vN*y^2 -
2.0*R^2*X*dy*y^2 - 1.0*R^2*dy*vN*y^2)^2);
F_dy = -(2.0*(8.0*R^10*X^2*dy - 4.0*R^9*X^2*y - 16.0*R^8*X^2*dy^2*y^2 +
2.0*R^8*X*dy^4*vN*y^2 - 8.0*R^8*X*dy^2*vN*y^2 + 8.0*R^8*X*dy^2*y^2 +
8.0*R^7*X^2*dy*y^3 - 12.0*R^7*X*dy^3*vN*y^3 + 4.0*R^7*X*dy*vN*y^3 -
4.0*R^7*X*dy*y^3 + 8.0*R^6*X^2*dy^3*y^4 - 4.0*R^6*X*dy^5*vN*y^4 +
16.0*R^6*X*dy^3*vN*y^4 - 8.0*R^6*X*dy^3*y^4 + 6.0*R^6*X*dy^2*vN*y^4 +
2.0*R^6*dy^3*vN^2*y^4 - 4.0*R^6*dy^3*vN*y^4 + 2.0*R^6*dy^3*y^4 -
4.0*R^5*X^2*dy^2*y^5 + 24.0*R^5*X*dy^4*vN*y^5 - 8.0*R^5*X*dy^2*vN*y^5 +
4.0*R^5*X*dy^2*y^5 + R^5*dy^6*vN^2*y^5 + 4.0*R^5*dy^4*vN^2*y^5 -
4.0*R^5*dy^4*vN*y^5 - 1.0*R^5*dy^2*vN^2*y^5 + 2.0*R^5*dy^2*vN*y^5 -
1.0*R^5*dy^2*y^5 + 2.0*R^4*X*dy^6*vN*y^6 - 8.0*R^4*X*dy^4*vN*y^6 -
```

```matlab
12.0*R^4*X*dy^3*vN*y^6 - 1.0*R^4*dy^6*vN*y^6 - 4.0*R^4*dy^4*vN^2*y^6 +
4.0*R^4*dy^4*vN*y^6 - 2.0*R^4*dy^3*vN^2*y^6 + 2.0*R^4*dy^3*vN*y^6 -
12.0*R^3*X*dy^5*vN*y^7 + 4.0*R^3*X*dy^3*vN*y^7 - 2.0*R^3*dy^7*vN^2*y^7 -
8.0*R^3*dy^5*vN^2*y^7 + 6.0*R^3*dy^5*vN*y^7 + 2.0*R^3*dy^3*vN^2*y^7 -
2.0*R^3*dy^3*vN*y^7 + 6.0*R^2*X*dy^4*vN*y^8 + 2.0*R^2*dy^5*vN^2*y^8 +
4.0*R^2*dy^4*vN^2*y^8 - 3.0*R^2*dy^4*vN*y^8 + R*dy^8*vN^2*y^9 +
4.0*R*dy^6*vN^2*y^9 - 1.0*R*dy^4*vN^2*y^9 -
2.0*dy^5*vN^2*y^10))/(R^2*y*(2.0*R^4*X + R^2*dy*y^2 + dy^2*vN*y^4 +
dy^4*vN*y^4 - 1.0*R^2*dy^3*vN*y^2 - 2.0*R^2*X*dy*y^2 -
1.0*R^2*dy*vN*y^2)^2);
d2z = F_y*z+F_dy*dz;
end
function S_r = fun_Sr(R,y,dy,vN,X)
S_r = (R^4*X + R^2*dy*y^2 + dy^2*y^4*log((- R^2 + dy*y^2)/(dy*y^2)) +
R^2*dy^3*vN*y^2 - 1.0*R^2*dy*vN*y^2)/(R^2*dy^2*vN*y^2);
end
function S_t = fun_St(R,y,dy,vN,X)
S_t = (R^4*X + dy*vN*y^4 + R^2*dy*y^2 + dy^2*y^4*log((- R^2 +
dy*y^2)/(dy*y^2)) - 1.0*R^2*dy*vN*y^2)/(R*dy*vN*y^3);
end
function [dSr_y, dSr_dy] = fun_dSr(R,y,dy,vN,X)
dSr_y = (1.0*(2*R^6*X - 2.0*dy^3*y^6*log((dy*y^2)/(- R^2 + dy*y^2)) +
2*R^2*dy^2*y^4 + 2.0*R^2*dy^2*y^4*log((dy*y^2)/(- R^2 + dy*y^2)) -
2.0*R^4*X*dy*y^2))/(R^2*dy^2*vN*y^3*(- R^2 + dy*y^2));
dSr_dy = (1.0*(2.0*R^4*X + R^2*dy*y^2 + dy^2*vN*y^4 + dy^4*vN*y^4 -
1.0*R^2*dy^3*vN*y^2 - 2.0*R^2*X*dy*y^2 - 1.0*R^2*dy*vN*y^2))/(dy^3*vN*y^2*(-
R^2 + dy*y^2));
end
%%
function p = bisection(f,a,b)
if f(a)*f(b)>0
    disp('Wrong choice bro')
else
    p = (a + b)/2;
    err = abs(f(p));
    while err > 1e-7
        if f(a)*f(p)<0
            b = p;
        else
            a = p;
        end
        p = (a + b)/2;
        err = abs(f(p));
    end
end
end
```

- MATLAB™ Codes for plotting Figures 5-6 to 5-9:

```matlab
A = 1;
B = 2;
C = 3;
L_0 = 1.077;
vN10 = [1E-2 1E-3 1E-3];
vN20 = [1E-3 1E-3 1E-2];
```

```matlab
X10 = [0.4 0.2 0.2];
X20 = [0.2 0.2 0.4];


str1 = [-2,-3,-3];
str2 = [-3,-3,-2];
str3 = ["Inner gel is stiffer than outer gel" "Inner and outer gels are
same" "Outer gel is stiffer than inner gel"];


Y0 = [10 10 10];
dy_0 = [0.1 0.1 0.1];
ddy_0 = [1E-2 1E-2 1E-2];


figure('units','normalized','outerposition',[0 0 1 1])


for k = 1:3
    vN1 = vN10(k);
    vN2 = vN20(k);
    X1 = X10(k);
    X2 = X20(k);

    Y(1) = Y0(k);

    S_r_C = inf;
    J = 0;
    j = 0;
    dy0 = dy_0(k);
    while abs(S_r_C) > 1E-6
        J = J+1;
        j = j+1;
        if abs(imag(S_r_C)) > 0 || j > 50 && abs(S_r_C) > 1E3 || j > 400 &&
abs(S_r_C) > 1E0
            dy0 = dy0+ddy_0(k);
            Y(1) = Y0(k);
            j = 1;
        end
        if J > 1E4
            break
        end
        % initial values
        y1(1) = L_0;
        dy1(1) = Y(j);
        z1(1) = 0;
        dz1(1) = 1;
        u0 = [y1(1); dy1(1); z1(1); dz1(1)];
        [R1,u1] = ode45(@(R1,u1) odefun(R1,u1,vN1,X1),[A B],u0);
        y1 = u1(:,1);
        dy1 = u1(:,2);
        z1 = u1(:,3);
        dz1 = u1(:,4);
        n1 = length(R1);
        clear S_r1 S_t1
        for i = 1:n1
            S_r1(i,1) = fun_Sr(R1(i),y1(i),dy1(i),vN1,X1);
            S_t1(i,1) = fun_St(R1(i),y1(i),dy1(i),vN1,X1);
        end
```

```matlab
        y2(1) = y1(n1);
        z2(1) = z1(n1);
        dz2(1) = dz1(n1);
        syms dy
        eqn = @(dy) S_r1(n1)-fun_Sr(B,y2(1),dy,vN2,X2);

        dy2(1) = fsolve(eqn,dy0);
        u0 = [y2(1); dy2(1); z2(1); dz2(1)];
        [R2,u2] = ode45(@(R2,u2) odefun(R2,u2,vN2,X2),[B C],double(u0));
        y2 = u2(:,1);
        dy2 = u2(:,2);
        z2 = u2(:,3);
        dz2 = u2(:,4);
        n2 = length(R2);
        clear S_r2 S_t2
        for i = 1:n2
            S_r2(i,1) = fun_Sr(R2(i),y2(i),dy2(i),vN2,X2);
            S_t2(i,1) = fun_St(R2(i),y2(i),dy2(i),vN2,X2);
        end
        S_r_C = S_r2(n2);
        [dSr_y2, dSr_dy2] = fun_dSr(R2(n2),y2(n2),dy2(n2),vN2,X2);
        Y(j+1) = real(Y(j)-S_r_C/(dSr_y2*z2(n2)+dSr_dy2*dz2(n2)));
        [dSr_y2B, dSr_dy2B] = fun_dSr(R2(1),y2(1),dy2(1),vN2,X2);
        ddy0 = (S_r1(n1)-S_r2(1))/(dSr_y2B*z2(1)+dSr_dy2B*dz2(1));
        [S_r_C dy0 j]
    end
    %%
    r1 = y1;
    r2 = y2;
    L_r1 = dy1;
    L_r2 = dy2;
    L_t1 = r1./R1;
    L_t2 = r2./R2;
    vC1 = ((L_t1.^2).*L_r1)-1;
    vC2 = ((L_t2.^2).*L_r2)-1;
    %%
    syms L1 L2
    eqn1 = @(L1) L1-1/L1+(L1^2/vN1)*(log((L1^3-1)/L1^3)+1/L1^3+X1/L1^6);
    L1_free = double(bisection(eqn1,1,100));
    vC1_free = L1_free^3-1;
    eqn2 = @(L2) L2-1/L2+(L2^2/vN2)*(log((L2^3-1)/L2^3)+1/L2^3+X2/L2^6);
    L2_free = double(bisection(eqn2,1,100));
    vC2_free = L2_free^3-1;
    %%
    color = [1 0 0;0 0.7 0;0 0 1];          % red green blue

    subplot(2,2,1); hold on; box on;
    P_r1(k) = plot([R1;R2], [r1;r2],'Color',color(k,:),'LineWidth',1.5);
    legendInfo{k} = str3(k);
    xline(B,':k','LineWidth',0.75);
    xlim([A,C]); ylim([0 10]); yticks(0:2:10);
    xlabel('R/A','FontSize',16,'Interpreter','latex');
ylabel('r(R)','FontSize',16,'Interpreter','latex');

legend([P_r1],legendInfo,'location','northwest','FontSize',14,'Interpreter',
```

```matlab
'latex');
    ax = gca; % current axes
    ax.FontSize = 14;
    ax.TickLabelInterpreter = 'latex'

    subplot(2,2,2); hold on; box on;
    plot(R1, vC1,'Color',color(k,:),'LineWidth',1.5);
    xline(B,':k','LineWidth',0.75);
    plot(R2, vC2,'Color',color(k,:),'LineWidth',1.5);
    xlim([A,C]); ylim([0 35]); yticks(0:5:35);
    xlabel('R/A','FontSize',16,'Interpreter','latex');
ylabel('vC','FontSize',16,'Interpreter','latex');
    ax = gca; % current axes
    ax.FontSize = 14;
    ax.TickLabelInterpreter = 'latex'

    subplot(2,2,3); hold on; box on;
    plot(R1, L_r1,'Color',color(k,:),'LineWidth',1.5);
    plot(R1, L_t1,'Color',color(k,:),'LineStyle','--','LineWidth',1.5);
    xline(B,':k','LineWidth',0.75);
    plot(R2, L_r2,'Color',color(k,:),'LineWidth',1.5);
    plot(R2, L_t2,'Color',color(k,:),'LineStyle','--','LineWidth',1.5);
    xlim([A,C]); ylim([0 10]); yticks(0:2:10)
    xlabel('R/A','FontSize',16,'Interpreter','latex');
ylabel('$$\lambda$$','FontSize',16,'Interpreter','latex');
    P_Lr = plot(nan,nan,'k-','LineWidth',1.5);
    P_Lt = plot(nan,nan,'k--','LineWidth',1.5);
    legend([P_Lr P_Lt],'$$\bf \lambda_{r}$$','$$\bf
\lambda_{\theta}$$','FontSize',14,'Interpreter','latex')
    ax = gca; % current axes
    ax.FontSize = 14;
    ax.TickLabelInterpreter = 'latex'

    subplot(2,2,4); hold on; box on;
    plot(R1, S_r1,'Color',color(k,:),'LineWidth',1.5);
    plot(R1, S_t1,'Color',color(k,:),'LineStyle','--','LineWidth',1.5);
    xline(B,':k','LineWidth',0.75); yline(0,'-.k','LineWidth',0.75);
    plot(R2, S_r2,'Color',color(k,:),'LineWidth',1.5);
    plot(R2, S_t2,'Color',color(k,:),'LineStyle','--','LineWidth',1.5);
    xlim([A,C]); ylim([-15 10]); yticks([-15 -10 -5 0 5 10])
    xlabel('R/A','FontSize',16,'Interpreter','latex');
ylabel('s/NkT','FontSize',16,'Interpreter','latex');
    P_Sr = plot(nan,nan,'k-','LineWidth',1.5);
    P_St = plot(nan,nan,'k--','LineWidth',1.5);
    legend([P_Sr  P_St],'$$\bf s_{r}$$','$$\bf
s_{\theta}$$','Location','southeast','FontSize',14,'Interpreter','latex' )
    ax = gca; % current axes
    ax.FontSize = 14;
    ax.TickLabelInterpreter = 'latex'
end
%%
subplot(2,2,2);
txt = {{'$$\bf vN_{I} = 10^{-2}$$'; '$$\bf \chi_{I} = 0.4$$'},...
    {'$$\bf vN_{I} = 10^{-3}$$'; '$$\bf \chi_{I} = 0.2$$'},...
    {'$$\bf vN_{II} = 10^{-3}$$'; '$$\bf \chi_{II} = 0.2$$'},...
```

```matlab
    {'$$\bf vN_{II} = 10^{-2}$$'; '$$\bf \chi_{II} = 0.4$$'}};
text([1.4 1.8 1.8 2.5 2.5], [14 21.5 30.5 29 7.5], [txt(1) txt(2) txt(2)
txt(3) txt(4)], 'HorizontalAlignment', 'center', 'BackgroundColor', 'w',
'EdgeColor', 'k', 'FontSize', 10, 'Interpreter','latex');
%%
function du = odefun(R,u,vN,X)
du = zeros(4,1);
du(1) = u(2);
du(2) = fun_d2y(R, u(1), u(2), vN, X);
du(3) = u(4);
du(4) = fun_d2z(R, u(1), u(2), u(3), u(4), vN, X);
end
function d2y = fun_d2y(R,y,dy,vN,X)
d2y = (2.0*dy*(y - R*dy)*(2.0*R^5*X + R^3*dy*y^2 + dy^3*vN*y^5 -
1.0*R^2*dy^2*vN*y^3 - 2.0*R^3*X*dy*y^2 - 1.0*R^3*dy*vN*y^2 +
R*dy^2*vN*y^4))/(R^4*dy*y^3 + 2.0*R^6*X*y + R^2*dy^2*vN*y^5 -
1.0*R^4*dy^3*vN*y^3 + R^2*dy^4*vN*y^5 - 2.0*R^4*X*dy*y^3 -
1.0*R^4*dy*vN*y^3);
end
function d2z = fun_d2z(R,y,dy,z,dz,vN,X)
F_y = (2.0*dy^2*(4.0*R^10*X^2 - 8.0*R^8*X^2*dy*y^2 - 6.0*R^8*X*dy^3*vN*y^2 -
4.0*R^8*X*dy*vN*y^2 + 4.0*R^8*X*dy*y^2 + 8.0*R^7*X*dy^2*vN*y^3 +
4.0*R^6*X^2*dy^2*y^4 + 12.0*R^6*X*dy^4*vN*y^4 + 8.0*R^6*X*dy^2*vN*y^4 -
4.0*R^6*X*dy^2*y^4 - 6.0*R^6*X*dy*vN*y^4 + R^6*dy^4*vN^2*y^4 -
1.0*R^6*dy^4*vN*y^4 + R^6*dy^2*vN^2*y^4 - 2.0*R^6*dy^2*vN*y^4 + R^6*dy^2*y^4
- 16.0*R^5*X*dy^3*vN*y^5 - 6.0*R^4*X*dy^5*vN*y^6 - 4.0*R^4*X*dy^3*vN*y^6 +
12.0*R^4*X*dy^2*vN*y^6 - 2.0*R^4*dy^5*vN^2*y^6 + 3.0*R^4*dy^5*vN*y^6 +
R^4*dy^4*vN^2*y^6 - 2.0*R^4*dy^3*vN^2*y^6 + 2.0*R^4*dy^3*vN*y^6 +
R^4*dy^2*vN^2*y^6 - 1.0*R^4*dy^2*vN*y^6 + 8.0*R^3*X*dy^4*vN*y^7 -
4.0*R^3*dy^4*vN*y^7 - 6.0*R^2*X*dy^3*vN*y^8 + R^2*dy^6*vN^2*y^8 -
2.0*R^2*dy^5*vN^2*y^8 + R^2*dy^4*vN^2*y^8 - 2.0*R^2*dy^3*vN^2*y^8 +
3.0*R^2*dy^3*vN*y^8 + dy^6*vN^2*y^10 + dy^4*vN^2*y^10))/(R^2*y^2*(2.0*R^4*X
+ R^2*dy*y^2 + dy^2*vN*y^4 + dy^4*vN*y^4 - 1.0*R^2*dy^3*vN*y^2 -
2.0*R^2*X*dy*y^2 - 1.0*R^2*dy*vN*y^2)^2);
F_dy = -(2.0*(8.0*R^10*X^2*dy - 4.0*R^9*X^2*y - 16.0*R^8*X^2*dy^2*y^2 +
2.0*R^8*X*dy^4*vN*y^2 - 8.0*R^8*X*dy^2*vN*y^2 + 8.0*R^8*X*dy^2*y^2 +
8.0*R^7*X^2*dy*y^3 - 12.0*R^7*X*dy^3*vN*y^3 + 4.0*R^7*X*dy*vN*y^3 -
4.0*R^7*X*dy*y^3 + 8.0*R^6*X^2*dy^3*y^4 - 4.0*R^6*X*dy^5*vN*y^4 +
16.0*R^6*X*dy^3*vN*y^4 - 8.0*R^6*X*dy^3*y^4 + 6.0*R^6*X*dy^2*vN*y^4 +
2.0*R^6*dy^3*vN^2*y^4 - 4.0*R^6*dy^3*vN*y^4 + 2.0*R^6*dy^3*y^4 -
4.0*R^5*X^2*dy^2*y^5 + 24.0*R^5*X*dy^4*vN*y^5 - 8.0*R^5*X*dy^2*vN*y^5 +
4.0*R^5*X*dy^2*y^5 + R^5*dy^6*vN^2*y^5 + 4.0*R^5*dy^4*vN^2*y^5 -
4.0*R^5*dy^4*vN*y^5 - 1.0*R^5*dy^2*vN^2*y^5 + 2.0*R^5*dy^2*vN*y^5 -
1.0*R^5*dy^2*y^5 + 2.0*R^4*X*dy^6*vN*y^6 - 8.0*R^4*X*dy^4*vN*y^6 -
12.0*R^4*X*dy^3*vN*y^6 - 1.0*R^4*dy^6*vN*y^6 - 4.0*R^4*dy^4*vN^2*y^6 +
4.0*R^4*dy^4*vN*y^6 - 2.0*R^4*dy^3*vN^2*y^6 + 2.0*R^4*dy^3*vN*y^6 -
12.0*R^3*X*dy^5*vN*y^7 + 4.0*R^3*X*dy^3*vN*y^7 - 2.0*R^3*dy^7*vN^2*y^7 -
8.0*R^3*dy^5*vN^2*y^7 + 6.0*R^3*dy^5*vN*y^7 + 2.0*R^3*dy^3*vN^2*y^7 -
2.0*R^3*dy^3*vN*y^7 + 6.0*R^2*X*dy^4*vN*y^8 + 2.0*R^2*dy^5*vN^2*y^8 +
4.0*R^2*dy^4*vN^2*y^8 - 3.0*R^2*dy^4*vN*y^8 + R*dy^8*vN^2*y^9 +
4.0*R*dy^6*vN^2*y^9 - 1.0*R*dy^4*vN^2*y^9 -
2.0*dy^5*vN^2*y^10))/(R^2*y*(2.0*R^4*X + R^2*dy*y^2 + dy^2*vN*y^4 +
dy^4*vN*y^4 - 1.0*R^2*dy^3*vN*y^2 - 2.0*R^2*X*dy*y^2 -
1.0*R^2*dy*vN*y^2)^2);
d2z = F_y*z+F_dy*dz;
end
```

```matlab
function S_r = fun_Sr(R,y,dy,vN,X)
S_r = (R^4*X + R^2*dy*y^2 + dy^2*y^4*log((- R^2 + dy*y^2)/(dy*y^2)) +
R^2*dy^3*vN*y^2 - 1.0*R^2*dy*vN*y^2)/(R^2*dy^2*vN*y^2);
end
function S_t = fun_St(R,y,dy,vN,X)
S_t = (R^4*X + dy*vN*y^4 + R^2*dy*y^2 + dy^2*y^4*log((- R^2 +
dy*y^2)/(dy*y^2)) - 1.0*R^2*dy*vN*y^2)/(R*dy*vN*y^3);
end
function [dSr_y, dSr_dy] = fun_dSr(R,y,dy,vN,X)
dSr_y = (1.0*(2*R^6*X - 2.0*dy^3*y^6*log((dy*y^2)/(- R^2 + dy*y^2)) +
2*R^2*dy^2*y^4 + 2.0*R^2*dy^2*y^4*log((dy*y^2)/(- R^2 + dy*y^2)) -
2.0*R^4*X*dy*y^2))/(R^2*dy^2*vN*y^3*(- R^2 + dy*y^2));
dSr_dy = (1.0*(2.0*R^4*X + R^2*dy*y^2 + dy^2*vN*y^4 + dy^4*vN*y^4 -
1.0*R^2*dy^3*vN*y^2 - 2.0*R^2*X*dy*y^2 - 1.0*R^2*dy*vN*y^2))/(dy^3*vN*y^2*(-
R^2 + dy*y^2));
end
%%
function p = bisection(f,a,b)
if f(a)*f(b)>0
    disp('Wrong choice bro')
else
    p = (a + b)/2;
    err = abs(f(p));
    while err > 1e-7
        if f(a)*f(p)<0
            b = p;
        else
            a = p;
        end
        p = (a + b)/2;
        err = abs(f(p));
    end
end
end
```

- MATLAB™ codes for plotting Figures 5-10 to 5-13:

```matlab
A = 1;
B = 2;
C = 3;
L_0 = 1.077;
vN10 = [1E-4 1E-4];
vN20 = [1E-1 1E-4];
X10 = [0.1 0.1];
X20 = [1.2 0.1];

str1 = [-4,-4];
str2 = [-1,-4];

Y0 = [20 10];
dy_0 = [0.01 0.1];
ddy_0 = [1E-4 1E-2];

figure('units','normalized','outerposition',[0 0 1 1])
```

125

```matlab
for k = 1:2
    vN1 = vN10(k);
    vN2 = vN20(k);
    X1 = X10(k);
    X2 = X20(k);


    Y(1) = Y0(k);


    S_r_C = inf;
    J = 0;
    j = 0;
    dy0 = dy_0(k);
    while abs(S_r_C) > 1E-6
        J = J+1;
        j = j+1;
        if abs(imag(S_r_C)) > 0 || j > 50 && abs(S_r_C) > 1E3 || j > 400 &&
abs(S_r_C) > 1E0
            dy0 = dy0+ddy_0(k);
            Y(1) = Y0(k);
            j = 1;
        end
        if J > 1E4
            break
        end
        % initial values
        y1(1) = L_0;
        dy1(1) = Y(j);
        z1(1) = 0;
        dz1(1) = 1;
        u0 = [y1(1); dy1(1); z1(1); dz1(1)];
        [R1,u1] = ode45(@(R1,u1) odefun(R1,u1,vN1,X1),[A B],u0);
        y1 = u1(:,1);
        dy1 = u1(:,2);
        z1 = u1(:,3);
        dz1 = u1(:,4);
        n1 = length(R1);
        clear S_r1 S_t1
        for i = 1:n1
            S_r1(i,1) = fun_Sr(R1(i),y1(i),dy1(i),vN1,X1);
            S_t1(i,1) = fun_St(R1(i),y1(i),dy1(i),vN1,X1);
        end
        y2(1) = y1(n1);
        z2(1) = z1(n1);
        dz2(1) = dz1(n1);
        syms dy
        eqn = @(dy) S_r1(n1)-fun_Sr(B,y2(1),dy,vN2,X2);

        dy2(1) = fsolve(eqn,dy0);
        u0 = [y2(1); dy2(1); z2(1); dz2(1)];
        [R2,u2] = ode45(@(R2,u2) odefun(R2,u2,vN2,X2),[B C],double(u0));
        y2 = u2(:,1);
        dy2 = u2(:,2);
        z2 = u2(:,3);
        dz2 = u2(:,4);
```

```matlab
        n2 = length(R2);
        clear S_r2 S_t2
        for i = 1:n2
            S_r2(i,1) = fun_Sr(R2(i),y2(i),dy2(i),vN2,X2);
            S_t2(i,1) = fun_St(R2(i),y2(i),dy2(i),vN2,X2);
        end
        S_r_C = S_r2(n2);
        [dSr_y2, dSr_dy2] = fun_dSr(R2(n2),y2(n2),dy2(n2),vN2,X2);
        Y(j+1) = real(Y(j)-S_r_C/(dSr_y2*z2(n2)+dSr_dy2*dz2(n2)));
        [dSr_y2B, dSr_dy2B] = fun_dSr(R2(1),y2(1),dy2(1),vN2,X2);
        ddy0 = (S_r1(n1)-S_r2(1))/(dSr_y2B*z2(1)+dSr_dy2B*dz2(1));
        [S_r_C dy0 j]
    end
    %%
    r1 = y1;
    r2 = y2;
    L_r1 = dy1;
    L_r2 = dy2;
    L_t1 = r1./R1;
    L_t2 = r2./R2;
    vC1 = ((L_t1.^2).*L_r1)-1;
    vC2 = ((L_t2.^2).*L_r2)-1;
    %%
    syms L1 L2
    eqn1 = @(L1) L1-1/L1+(L1^2/vN1)*(log((L1^3-1)/L1^3)+1/L1^3+X1/L1^6);
    L1_free = double(bisection(eqn1,1,100));
    vC1_free = L1_free^3-1;
    eqn2 = @(L2) L2-1/L2+(L2^2/vN2)*(log((L2^3-1)/L2^3)+1/L2^3+X2/L2^6);
    L2_free = double(bisection(eqn2,1,100));
    vC2_free = L2_free^3-1;
    %%
    color = [1 0 0;0 0 1];

    subplot(2,2,1); hold on; box on;
    plot([R1;R2], [r1;r2],'Color',color(k,:),'LineWidth',1.5);
    xline(B,':k','LineWidth',0.75);
    xlim([A,C]); ylim([0 15]); yticks(0:3:15);
    xlabel('R/A','FontSize',16,'Interpreter','latex');
ylabel('r(R)','FontSize',16,'Interpreter','latex');
    ax = gca; % current axes
    ax.FontSize = 14;
    ax.TickLabelInterpreter = 'latex';

    subplot(2,2,2); hold on; box on;
    plot(R1, vC1,'Color',color(k,:),'LineWidth',1.5);
    xline(B,':k','LineWidth',0.75);
    plot(R2, vC2,'Color',color(k,:),'LineWidth',1.5);
    xlim([A,C]); ylim([0 150]); yticks(0:30:150);
    xlabel('R/A','FontSize',16,'Interpreter','latex');
ylabel('vC','FontSize',16,'Interpreter','latex');
    ax = gca; % current axes
    ax.FontSize = 14;
    ax.TickLabelInterpreter = 'latex';

    subplot(2,2,3); hold on; box on;
```

127

```matlab
    plot(R1, L_r1,'Color',color(k,:),'LineWidth',1.5);
    plot(R1, L_t1,'Color',color(k,:),'LineStyle','--','LineWidth',1.5);
    xline(B,':k','LineWidth',0.75);
    plot(R2, L_r2,'Color',color(k,:),'LineWidth',1.5); plot(R2,
L2_free*ones(n2,1),'-.k','LineWidth',0.75);
    plot(R2, L_t2,'Color',color(k,:),'LineStyle','--','LineWidth',1.5);
    xlim([A,C]); ylim([0 15]); yticks(0:3:15)
    xlabel('R/A','FontSize',16,'Interpreter','latex');
ylabel('$$\lambda$$','FontSize',16,'Interpreter','latex');
    P_Lr = plot(nan,nan,'k-','LineWidth',1.5);
    P_Lt = plot(nan,nan,'k--','LineWidth',1.5);
    P_Lf = plot(nan,nan,'k-.','LineWidth',0.75);
    legend([P_Lr P_Lt P_Lf],'$$\bf \lambda_{r}$$','$$\bf
\lambda_{\theta}$$','$$\bf
\lambda_{free}$$','FontSize',14,'Interpreter','latex')
    ax = gca; % current axes
    ax.FontSize = 14;
    ax.TickLabelInterpreter = 'latex';

    subplot(2,2,4); hold on; box on;
    plot(R1, S_r1,'Color',color(k,:),'LineWidth',1.5);
    plot(R1, S_t1,'Color',color(k,:),'LineStyle','--','LineWidth',1.5);
    xline(B,':k','LineWidth',0.75); yline(0,'-.k','LineWidth',0.75);
    plot(R2, S_r2,'Color',color(k,:),'LineWidth',1.5);
    plot(R2, S_t2,'Color',color(k,:),'LineStyle','--','LineWidth',1.5);
    xlim([A,C]); ylim([-30 10]); yticks([-30 -20 -10 0 10])
    xlabel('R/A','FontSize',16,'Interpreter','latex');
ylabel('s/NkT','FontSize',16,'Interpreter','latex');
    P_Sr = plot(nan,nan,'k-','LineWidth',1.5);
    P_St = plot(nan,nan,'k--','LineWidth',1.5);
    legend([P_Sr  P_St],'$$\bf s_{r}$$','$$\bf
s_{\theta}$$','Location','southeast','FontSize',14,'Interpreter','latex' )
    ax = gca; % current axes
    ax.FontSize = 14;
    ax.TickLabelInterpreter = 'latex';
end
%%
subplot(2,2,1);
txt = {{'$$\bf vN_{I} = 10^{-4}$$'; '$$\bf \chi_{I} = 0.1$$'},...
    {'$$\bf vN_{II} = 10^{-4}$$'; '$$\bf \chi_{II} = 0.1$$'},...
    {'$$\bf vN_{II} = 10^{-1}$$'; '$$\bf \chi_{II} = 1.2$$'}};
text([1.5 2.5 2.5], [6 13 8.5], [txt(1) txt(2) txt(3)],
'HorizontalAlignment', 'center', 'BackgroundColor', 'w', 'EdgeColor', 'k',
'FontSize', 10, 'Interpreter','latex');
%%
function du = odefun(R,u,vN,X)
du = zeros(4,1);
du(1) = u(2);
du(2) = fun_d2y(R, u(1), u(2), vN, X);
du(3) = u(4);
du(4) = fun_d2z(R, u(1), u(2), u(3), u(4), vN, X);
end
function d2y = fun_d2y(R,y,dy,vN,X)
d2y = (2.0*dy*(y - R*dy)*(2.0*R^5*X + R^3*dy*y^2 + dy^3*vN*y^5 -
1.0*R^2*dy^2*vN*y^3 - 2.0*R^3*X*dy*y^2 - 1.0*R^3*dy*vN*y^2 +
R*dy^2*vN*y^4))/(R^4*dy*y^3 + 2.0*R^6*X*y + R^2*dy^2*vN*y^5 -
```

```
1.0*R^4*dy^3*vN*y^3 + R^2*dy^4*vN*y^5 - 2.0*R^4*X*dy*y^3 -
1.0*R^4*dy*vN*y^3);
end
function d2z = fun_d2z(R,y,dy,z,dz,vN,X)
F_y = (2.0*dy^2*(4.0*R^10*X^2 - 8.0*R^8*X^2*dy*y^2 - 6.0*R^8*X*dy^3*vN*y^2 -
4.0*R^8*X*dy*vN*y^2 + 4.0*R^8*X*dy*y^2 + 8.0*R^7*X*dy^2*vN*y^3 +
4.0*R^6*X^2*dy^2*y^4 + 12.0*R^6*X*dy^4*vN*y^4 + 8.0*R^6*X*dy^2*vN*y^4 -
4.0*R^6*X*dy^2*y^4 - 6.0*R^6*X*dy*vN*y^4 + R^6*dy^4*vN^2*y^4 -
1.0*R^6*dy^4*vN*y^4 + R^6*dy^2*vN^2*y^4 - 2.0*R^6*dy^2*vN*y^4 + R^6*dy^2*y^4
- 16.0*R^5*X*dy^3*vN*y^5 - 6.0*R^4*X*dy^5*vN*y^6 - 4.0*R^4*X*dy^3*vN*y^6 +
12.0*R^4*X*dy^2*vN*y^6 - 2.0*R^4*dy^5*vN^2*y^6 + 3.0*R^4*dy^5*vN*y^6 +
R^4*dy^4*vN^2*y^6 - 2.0*R^4*dy^3*vN^2*y^6 + 2.0*R^4*dy^3*vN*y^6 +
R^4*dy^2*vN^2*y^6 - 1.0*R^4*dy^2*vN*y^6 + 8.0*R^3*X*dy^4*vN*y^7 -
4.0*R^3*dy^4*vN*y^7 - 6.0*R^2*X*dy^3*vN*y^8 + R^2*dy^6*vN^2*y^8 -
2.0*R^2*dy^5*vN^2*y^8 + R^2*dy^4*vN^2*y^8 - 2.0*R^2*dy^3*vN^2*y^8 +
3.0*R^2*dy^3*vN*y^8 + dy^6*vN^2*y^10 + dy^4*vN^2*y^10))/(R^2*y^2*(2.0*R^4*X
+ R^2*dy*y^2 + dy^2*vN*y^4 + dy^4*vN*y^4 - 1.0*R^2*dy^3*vN*y^2 -
2.0*R^2*X*dy*y^2 - 1.0*R^2*dy*vN*y^2)^2);
F_dy = -(2.0*(8.0*R^10*X^2*dy - 4.0*R^9*X^2*y - 16.0*R^8*X^2*dy^2*y^2 +
2.0*R^8*X*dy^4*vN*y^2 - 8.0*R^8*X*dy^2*vN*y^2 + 8.0*R^8*X*dy^2*y^2 +
8.0*R^7*X^2*dy*y^3 - 12.0*R^7*X*dy^3*vN*y^3 + 4.0*R^7*X*dy*vN*y^3 -
4.0*R^7*X*dy*y^3 + 8.0*R^6*X^2*dy^3*y^4 - 4.0*R^6*X*dy^5*vN*y^4 +
16.0*R^6*X*dy^3*vN*y^4 - 8.0*R^6*X*dy^3*y^4 + 6.0*R^6*X*dy^2*vN*y^4 +
2.0*R^6*dy^3*vN^2*y^4 - 4.0*R^6*dy^3*vN*y^4 + 2.0*R^6*dy^3*y^4 -
4.0*R^5*X^2*dy^2*y^5 + 24.0*R^5*X*dy^4*vN*y^5 - 8.0*R^5*X*dy^2*vN*y^5 +
4.0*R^5*X*dy^2*y^5 + R^5*dy^6*vN^2*y^5 + 4.0*R^5*dy^4*vN^2*y^5 -
4.0*R^5*dy^4*vN*y^5 - 1.0*R^5*dy^2*vN^2*y^5 + 2.0*R^5*dy^2*vN*y^5 -
1.0*R^5*dy^2*y^5 + 2.0*R^4*X*dy^6*vN*y^6 - 8.0*R^4*X*dy^4*vN*y^6 -
12.0*R^4*X*dy^3*vN*y^6 - 1.0*R^4*dy^6*vN*y^6 - 4.0*R^4*dy^4*vN^2*y^6 +
4.0*R^4*dy^4*vN*y^6 - 2.0*R^4*dy^3*vN^2*y^6 + 2.0*R^4*dy^3*vN*y^6 -
12.0*R^3*X*dy^5*vN*y^7 + 4.0*R^3*X*dy^3*vN*y^7 - 2.0*R^3*dy^7*vN^2*y^7 -
8.0*R^3*dy^5*vN^2*y^7 + 6.0*R^3*dy^5*vN*y^7 + 2.0*R^3*dy^3*vN^2*y^7 -
2.0*R^3*dy^3*vN*y^7 + 6.0*R^2*X*dy^4*vN*y^8 + 2.0*R^2*dy^5*vN^2*y^8 +
4.0*R^2*dy^4*vN^2*y^8 - 3.0*R^2*dy^4*vN*y^8 + R*dy^8*vN^2*y^9 +
4.0*R*dy^6*vN^2*y^9 - 1.0*R*dy^4*vN^2*y^9 -
2.0*dy^5*vN^2*y^10))/(R^2*y*(2.0*R^4*X + R^2*dy*y^2 + dy^2*vN*y^4 +
dy^4*vN*y^4 - 1.0*R^2*dy^3*vN*y^2 - 2.0*R^2*X*dy*y^2 -
1.0*R^2*dy*vN*y^2)^2);
d2z = F_y*z+F_dy*dz;
end
function S_r = fun_Sr(R,y,dy,vN,X)
S_r = (R^4*X + R^2*dy*y^2 + dy^2*y^4*log((- R^2 + dy*y^2)/(dy*y^2)) +
R^2*dy^3*vN*y^2 - 1.0*R^2*dy*vN*y^2)/(R^2*dy^2*vN*y^2);
end
function S_t = fun_St(R,y,dy,vN,X)
S_t = (R^4*X + dy*vN*y^4 + R^2*dy*y^2 + dy^2*y^4*log((- R^2 +
dy*y^2)/(dy*y^2)) - 1.0*R^2*dy*vN*y^2)/(R*dy*vN*y^3);
end
function [dSr_y, dSr_dy] = fun_dSr(R,y,dy,vN,X)
dSr_y = (1.0*(2*R^6*X - 2.0*dy^3*y^6*log((dy*y^2)/(- R^2 + dy*y^2)) +
2*R^2*dy^2*y^4 + 2.0*R^2*dy^2*y^4*log((dy*y^2)/(- R^2 + dy*y^2)) -
2.0*R^4*X*dy*y^2))/(R^2*dy^2*vN*y^3*(- R^2 + dy*y^2));
dSr_dy = (1.0*(2.0*R^4*X + R^2*dy*y^2 + dy^2*vN*y^4 + dy^4*vN*y^4 -
1.0*R^2*dy^3*vN*y^2 - 2.0*R^2*X*dy*y^2 - 1.0*R^2*dy*vN*y^2))/(dy^3*vN*y^2*(-
R^2 + dy*y^2));
end
```

```matlab
%%
function p = bisection(f,a,b)
if f(a)*f(b)>0
    disp('Wrong choice')
else
    p = (a + b)/2;
    err = abs(f(p));
    while err > 1e-7
        if f(a)*f(p)<0
            b = p;
        else
            a = p;
        end
        p = (a + b)/2;
        err = abs(f(p));
    end
end
end
```